MOLECULAR LEVEL MECHANICAL PROPERTIES OF ULTRA HIGH TEMPERATURE CERAMICS AND THEIR NANOCOMPOSITES

A Dissertation
Submitted to the Faculty of
University of Texas at Arlington
by Md Riaz Kayser

In Partial Fulfillment of the Requirements for the

Degree of Doctor of Philosophy

Department of Mechanical Engineering

in the Graduate School

University of Texas at Arlington

August 2020

Acknowledgements

I wish to express my sincere appreciation to my supervisor, Dr. Ashfaq Adnan, who convincingly guided and encouraged me to be professional and do the right thing even when the road got tough. Without his persistent help, the goal of this project would not have been realized. I am indebted for his plentiful enlightening discussions and inspiring critiques, which makes me become a better researcher. Financial support from National Science Foundation (CMMI -1540346) is highly appreciated. Without their support and funding, this project could not have reached its goal. I would like to extend my sincere thanks to Dr. Ferdous and Dr. Yuan-Ting Wu who gave me unconditional support when I need help.

I would like to thank Dr. Reifsnider, Dr. Agonafer and Dr. Luo for becoming a committee member of my dissertation defense. Each of them has provided me with the insights that have allowed me to progress in my research. I gratefully acknowledge Dr. Raihan and Dr. Liao for their assistance with different tools to accomplish my research.

To all my lab-mates, thanks for the fun and support. The number of people that have helped me with this research is large, and I will not list the names for fear of omitting someone. I greatly look forward to having all of you as colleagues in the years ahead.

Finally, I wish to acknowledge the support and great love my parents and my wife, Jui. They kept me going on and this work would not have been possible without their input.

Thanks for all your encouragement!

I dedicate this dissertation to my parents and my wife for their constant support and unconditional love. I love you all dearly.

Abstract

Ultra High-Temperature Ceramics (UHTC) have been of great interest in the spacecraft, aerospace, and aeronautic industry due to their high melting point and their potential application as a protective material for the stagnation areas of leading edges. In this work, the effect of nanoparticle reinforcement for achieving tailored mechanical properties of UHTC's has been studied. Two different material systems have been considered, namely the ZrB_2-based and the HfO_2-based nanocomposites. In the first study, the grain boundary driven mechanical behavior of polycrystalline ZrB_2 and ZrC-ZrB_2 nanocomposites using large-scale molecular dynamics simulations have been performed. The atomistic models of polycrystalline ZrB_2 and ZrC-ZrB_2 nanocomposite were subjected to tensile loading to determine their elastic constants and strengths. It has been found that the presence of nanoparticles imparts an insignificant effect on the mechanical properties of ZrB_2. It has also been observed that failure mechanisms of both ZrB_2 and ZrC-ZrB_2 nanocomposite are driven by grain boundary deformation. In the second study, an atomistic computational study of electric field and thermal effects on the mechanical behavior of memristor material HfO_2 have been performed. Since the material has non-symmetric crystal structure, it is observed that tensile properties along the x, y and z directions are different. In addition, the effects of electrical field on mechanical behavior are studied by varying the electrical field intensity from 0 to 0.3 v/Å gradually. For each case, atomistic snapshots are taken to identify the changes occur in the structure due to the electric field. A significant structural damage on the crystal structure of HfO_2 is observed after applying 0.3 v/Å electric field, whereas the structural change is insignificant when the magnitude of the electric field is 0.2 v/Å or less. To understand more about the damage of this material, shear loads are applied in different directions and their responses are studied in this work.

Table of Contents

List of Figures

List of Tables

Chapter 1

Introduction

1.1 Nanotechnology: Scopes and Challenges

The design of more efficient devices relies on a robust understanding of the science at atomic scales. How materials coalesce, how chemical bonds form and break—these are the key questions one needs to answer to design better materials and better devices. By tailoring the structures of materials at extremely small scales many desired properties can be achieved. Using nanotechnology, materials can essentially be made stronger, lighter, more durable, more reactive, better electrical conductors and many other traits can also be achieved. Nanotechnology is helping to substantially improve, even revolutionize, many technology and industrial sectors, like medicine[1][2], information technology[3][4], transportation[5], energy and food safety[6][7], [8], and many others. For example, nanoparticles have been developed as effective target specific strategies for drug delivery, acting as nanocarriers and active agents [9]–[11]. Over the last decades, different types of nanoparticles have been developed based on various components, including carbon, metal oxides, silica oxides, nanocrystals, lipids, dendrimers, polymers, and quantum dots, together with wide variety of recently developed materials[9], [12]–[15].These nanomaterials are capable to provide a high degree of biocompatibility before and after conjugation to biomolecules for specific function so as to translate into nanomedicines and clinical practice. In addition, nanoscale additives to or surface treatments of fabrics can provide lightweight ballistic energy deflection in personal body armor [16]–[18]. Flexible, foldable, bendable, and stretchable electronics are reaching into various sectors and are being integrated with aerospace applications, wearables, and the Internet of Things. Semiconductor nanomembranes and other nanomaterials like graphene and cellulosic nanomaterials are being used to make flexible electronics to enable wearable and “tattoo” type sensors[19], electronic papers[20] that can be rolled up and photovoltaics[21] that can be sewn onto clothing. Making flexible, flat, lightweight, non-brittle, highly efficient electronics opens the new horizon to countless smart products. Nanostructured ceramic coatings exhibit much greater toughness than conventional wear-resistant coatings

for thermal protection system applications on space shuttle. Also, carbon nanotube sheets are now being produced for use in next-generation air vehicles.

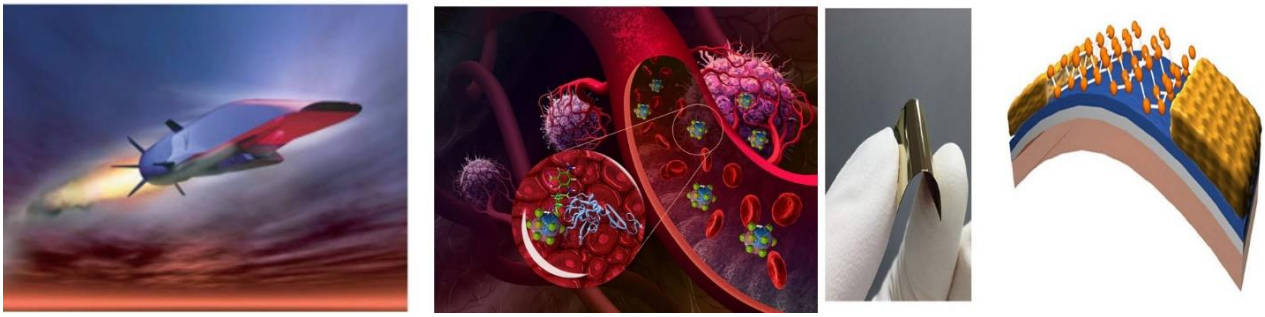

(a) (b) (c)

Figure 1-1 Different applications of nanotechnology (a) For next generation space vehicles[22] (reprinted from "Ultra-high temperature ceramics: Materials for extreme environments", 2017 with the permission from Elsevier(b) drug delivery[23] (c) flexible nanoelectronics[24].

Therefore, to develop a new functional material, it is imperative to understand the forces that shape them at nano scales. Studies should bridge the continuum scale from subatomic, to atomic, to molecular, to nanoscale, and beyond. Those studies will create foundational knowledge that will help us to achieve real-time adaptive control over materials fabrication. Fabricating these structures at the micro- or even nanoscale is a huge challenge. Chemical reactions have to be controlled so as to add or remove material where it is needed, sometimes as precisely as one atomic layer at a time. To accomplish this goal, one needs to work at the intersection between Materials Science and Mechanical Engineering—where the study of materials structure-property relationships drives the design and fabrication of components with optimized performance using the most advanced manufacturing technologies. Often times computational techniques paves the way of developing new materials by optimizing many parameters with time-saving solutions.

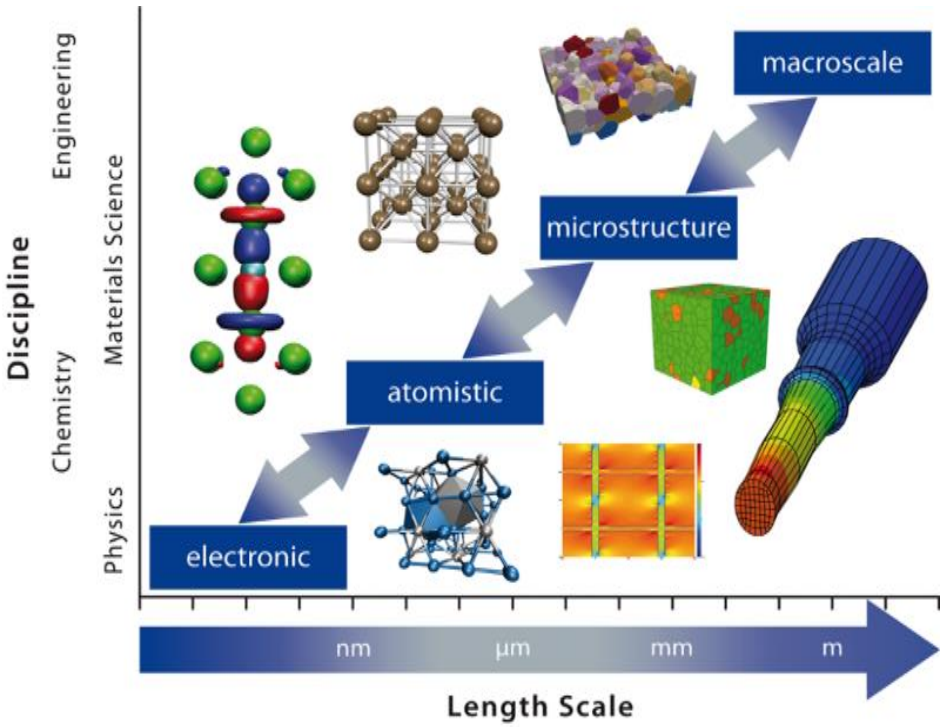

Figure 1-2 Developing novel material requires overcoming the borders between different disciplines for a seamless integration of the models on different length scales into one coherent modelling framework[25].

1.2 Background and Significance

Next generation materials for the use on space vehicle needs significant improvements in material properties leading to enhanced reliability and safety to survive extreme environments. Due to high melting point, ultra-high hardness, low density, excellent wear resistance, high refractoriness, high electrical and thermal conductivity, Ultra-high temperature ceramics (UHTC), primarily composed of metal diborides, are considered as potential materials for hypersonic re-entry vehicles to survive this extreme environment. The main goals of developing new UHTC's are that the space exploration should have to be reusable and reliable. With the development of new UHTC's it will survive multiple reentries from orbital speeds to our worldly atmosphere and that will enormously accelerate the space exploration due to the fact of reducing the use of resources needed to keep exploring.

Ceramics are utilized in different industries from pottery to electronics, from cutting tools to medical device industries[26], it has enormous field of applications. Recently it has been considered for creating thermal

protection system applications due to their high melting point and withstanding capability in high temperature and pressures[27]. It is extremely desirable in many of engineering applications that a material should have the properties of high stiffness and high toughness but in practical low toughness and fracture toughness of ceramics restricts their applications to many different industries.

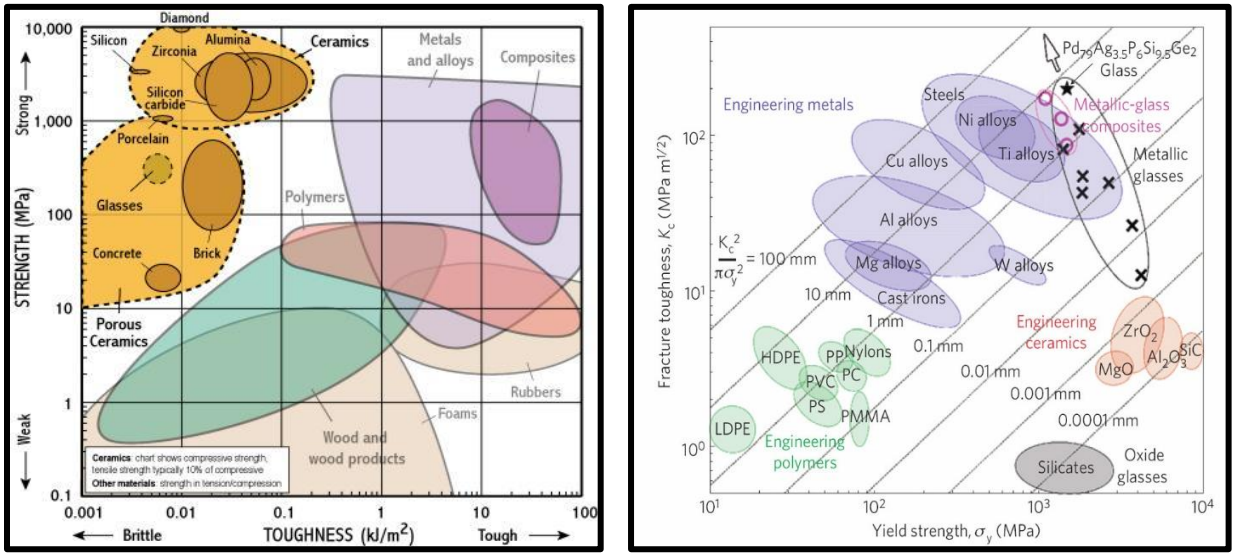

Figure 1-3 Comparison of mechanical properties of metal, ceramic and polymer materials[28](reprinted from "The conflicts between strength and toughness", 2011 with the permission from Nature Materials)

Fracture toughness is the ability of a material containing crack to resist fracture and it quantifies how a material responds to resist ultimate failure of a system. Cracks are developed in engineering parts when it experiences different types of loading, mainly in fatigue. Later those cracks are accumulated and leads to catastrophic failure in brittle material such as in ceramics. Strength and toughness are the two critical properties that are desired in wide range of engineering applications. The attainment of these two properties is a vital requirement for many structural materials: unfortunately, strength and toughness are mutually exclusive. A material with higher strength can carry higher loads before failure, and materials with high toughness can go through larger deformation without breaking. The fracture toughness of different materials can be seen from figure 1-3. The desired properties will be having the higher toughness of material

without sacrificing the strength significantly. The poor fracture toughness of the ceramics limits its application on extreme environments.

This lower fracture toughness and the brittleness of the ceramics originate from their bonding character. Both covalent and ionic bonding can be found in the ceramic material. The degree of covalent character increases with the decrease of difference in electro-negativity of atoms. Because of the directional characteristics of covalent bond, the dislocation motion of the atoms is not allowed. This restriction in the dislocation movement greatly degrades the toughness properties of ceramics because the dislocation motions are responsible for controlling the toughness properties of a material.

Ceramics have high strength and stiffness compared to metal because they are bonded with covalent or ionic bonds, however metals have much higher toughness than ceramics. Metal has valence electrons at outermost shell that plays a vital role to explain the high toughness and ductility of a material. As shown in figure 1-4, in metallic materials valence electrons are loosely bonded with positive charge and these electrons are responsible for allowing large deformation of the whole material. In addition, metals having face centered cubic (FCC) crystal structure in particular, allow dislocations along the maximum planar atomic density planes. Dislocations are directly related to plastic deformation, which in turn, can enhance the toughness of materials. Ceramic materials having predominantly covalent bonds, dislocation movements are quite difficult due to rigid bond network and directional properties.

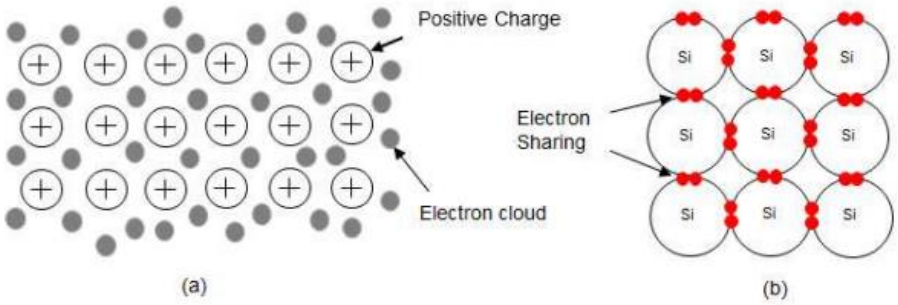

Figure 1-4 Schematic diagram to represent bonding in (a) metal and (b) ceramic (covalent)[27]

Therefore, the dislocation movement needs the bonds to be broken and reformed as well as the bond angles to be distorted[29]. So, tailoring of mechanical properties especially toughness is not trivial although the experts are exploring every possible way to come up with a novel material which will have higher stiffness as well as demanded toughness. Research have been carried out extensively to improve fracture toughness (with crack) and the toughness (when no crack is present) property of ceramic materials without compromising other mechanical properties of ceramics. With different types of loading crack nucleation happens in every material and the crack propagation leads to ultimate failure for entire structure. So, higher fracture toughness is a desired factor for every material system. Zhang et al. reported [1] several experimental methods to increase the fracture toughness property of materials including crack bridging, crack blunting, or relaxation of the strain field around the crack tip. Ferdous et al. created multiphase ceramics with lattice mismatched interfaces and computationally investigated their mechanical properties. The tensile properties of the new phase enhanced with C enrichment of SiC structure. As it creates lattice mismatch structure compared to single phase SiC, the tensile and shear properties are enhanced. For 10% and 40% C enrichment the tensile strength increased by 23 and 86 GPa respectively. 10% ‘‘C” enriched appears to be best performing in terms of tensile strength and toughness compared to pure SiC [92]. A similar approach is followed to create a multiphase ceramic of ZrB_2 and ZrC.

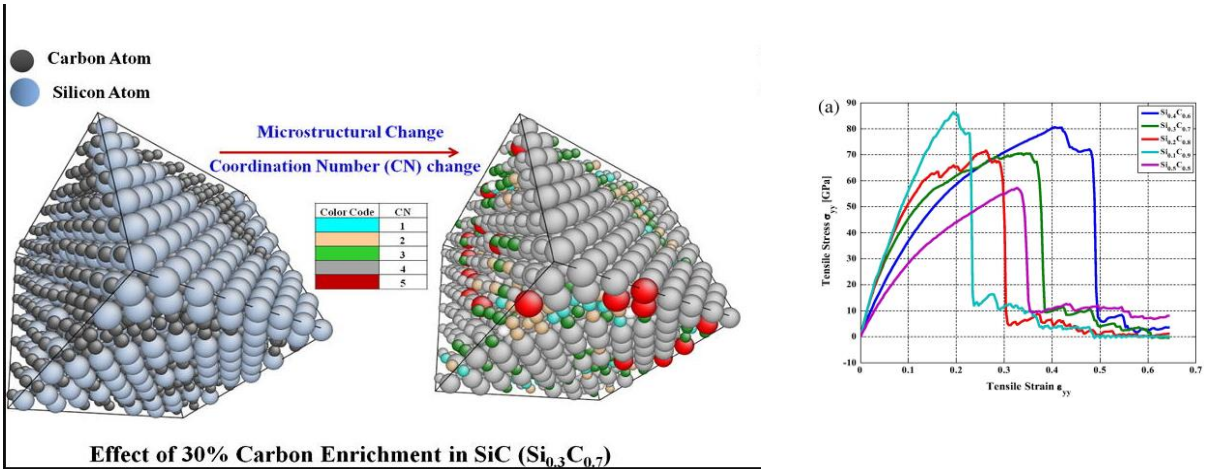

Figure 1-5 Effect of Carbon enrichment on the mechanical properties of SiC[27].

1.3 Research Objectives and Outline of the Thesis

The objective of my research is to investigate the effect of nanoparticle reinforcement for achieving tailored mechanical properties of UHTC's. In this work we investigated the formation of novel Zirconium (Zr) based "strong and tough" multiphase ceramics by selectively choosing phases with "thermodynamically compatible" crystal structure but different lattice constants to form "energy dissipate-able" microstructures. By creating the innovative energy dissipate-able microstructure, we hypothesized that during deformation some microstructural change will take place across the ceramic-ceramic lattice mismatched interface, which eventually will contribute to energy dissipation. Therefore, overall toughness of the material will increase. If we attempt to trace back to identify the parameters that controls the performance of a material, we can see that properties of materials are mostly influenced by the atomic structure, composition, microstructure, interfaces and the defects. Therefore, it is critical to quantitatively study the mechanics and physics of nanostructured materials and their interfaces, so that by modeling the physical laws that are relevant at the nanoscale can generate the desired macroscopic properties.

In this work, two different material systems have been studied, namely the ZrB_2-based and the HfO_2-based nanocomposites. Molecular dynamics (MD) simulation has been used to identify the effects of reinforcing materials, defects, interfaces, and microstructure on the overall mechanical properties of UHTC's. We also discuss about the validation of our computational work by the experiments done by our collaborator. The outline of the thesis and specific goals are as follows:

(i) In Chapter 2, the structural and mechanical properties with different fabrication methods of UHTCs are described and in Chapter 3, the principles of the computational tool that's been used to study the materials properties in atomistic scale are discussed.

(ii) In Chapter 4, we report the grain boundary driven mechanical behavior of two polycrystalline ultra-high-temperature ceramics (UHTC's), zirconium diboride (ZrB_2) and zirconium carbide (ZrC) with zirconium diboride (ZrC-ZrB_2) nanocomposites. First, we discussed the procedure of creating atomistic

models of the polycrystalline ZrB_2 and ZrC-ZrB_2 nanocomposites. Then the tensile properties of ZrB_2 and its nanocomposites are mentioned. Also, the effect of position and particle size of reinforcing ZrC in the host ceramics ZrB_2 are discussed elaborately. At different loading states, the deformation snapshots of the nanocomposite are captured, the local stress of the microstructure are determined and the reasons for the failure are identified from those study.

(iii) In Chapter 5, we discuss new sets of simulations to find the tensile and shear properties of grain boundary material. A detailed modeling approach for developing a model with grain boundary and twin crystal are mentioned here. The results were compared with the adjacent single crystal and overall polycrystalline material properties, where we found that the shear strength and stiffness of the grain boundary materials are significantly lower than the single crystal or polycrystal ZrB_2. At the end of the chapter, an analytical approach was employed with the grain boundary and twin crystal sub model to determine the tensile and shear modulus of grain boundary.

(iv) In Chapter 6, we present an atomistic computational study of electric field and thermal effects on the mechanical behavior of memristor material HfO_2. In our study, first, the atomistic model of HfO_2 is built on a monoclinic lattice structure. Then, tensile tests have been carried out to study its mechanical behavior. Since the material has non-symmetric crystal structure. In addition, the effects of electrical field on mechanical behavior are studied by varying the electrical field intensity from 0 to 0.3 v/Å gradually. For each case, atomistic snapshots are taken to identify the changes occur in the structure due to the electric field. To understand more about the damage of this material, shear loads are applied in different directions and their responses are studied elaborately in this chapter.

(v) Finally, we summarize our findings and some future research directions are outlined at the end of the dissertation.

Chapter 2

Zirconium Diboride Based Ceramics

2.1 Introduction

Because of the high melting point(3245°C), high thermal conductivity, low density (6.09 g/cm^3) compared to refractory metals and high strength, Zirconium diboride is considered as a potential candidate for using as ultra-high temperature ceramics(UHTC)[30]. In general, at room temperature the borides exhibit lower electrical resistivity and higher thermal conductivities than carbide ceramics. In addition, the Borides exhibit better resistance to chemical attack. These characteristics have yielded borides candidates for applications including molten metal crucibles, refractory linings, cutting tools, furnace electrodes, and particularly for the use on potential hypersonic aerospace vehicles. In this section, a general overview of zirconium diboride based ceramics and their recent research progress is presented. At the beginning, the crystal structure, chemical and physical properties are presented briefly. Later, the different manufacturing processes along with sintering techniques of ceramics are reviewed. Moreover, several methods for depositing ceramics nanofilm presented in the later part. The effects of processing, composition, and microstructure on the overall mechanical properties of the material are discussed thoroughly.

2.2 Crystal Structure and Properties

Zirconium diboride (ZrB_2) has alternating layers of zirconium and boron atoms, which represents the AlB_2-type P6/mmm crystal structure (Figure 2-1). Boron atoms create 2D graphene-type sheets alternating with close packed zirconium layers. In the middle of two adjoining boron layers, Zirconium atoms remain in the center of each boron hexagon. Each boron atom is surrounded by 3 equidistant boron atoms, and 6 equidistant zirconium atoms. On the other hand, each zirconium atom contains 6 equidistant zirconium neighbors and 12 equidistant boron neighbors. This crystal structure indicates a combination of covalent,

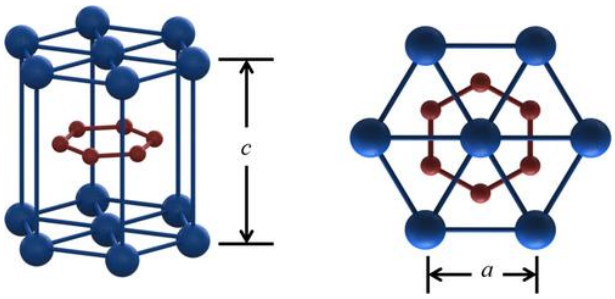

Figure 2-1 Crystal structure of ZrB_2

ionic, and metallic bonding: B-B bonds are covalent; Zr-B bonds show both ionic and covalent characteristics; Zr-Zr bonds exhibit metallic and covalent bonding. The anisotropic form of the ZrB_2 crystal structure leads in many of its mechanical and physical characteristics being anisotropic. For example, hardness of the material varies in different planes in ZrB_2 structure. Xuan et al. measured the Vickers hardness of ZrB_2 single crystalline structure in the temperature range from 25°C to 1000°C[30]. The hardness decreased from ~20.9 GPa for all planes to ~7.9 GPa for the (0001) plane and ~4.9 GPa for the (1010) and (1120) planes with the increase of the temperature from 25°C to 1000°C. The hardness of the (1120) and (1010) planes was much lower(~35%) than that of the (0001) plane for the same temperature range. Okamoto et al. reported the elastic constants of single crystal ZrB_2 in different temperature range, where he found C_{12} is below 100 GPa, C_{33} is above 400 GPa, and C_{11} is greater than 500 GPa. These elastic constants vary with changes in temperature. It is reported that C_{12} and C_{13} appear to be insensitive to variations in temperature up to 1400°C while C_{11}, C_{33}, and C_{44} decrease with increasing temperature. The coefficient of thermal expansions (CTE) of ZrB_2 are 6.7 X 10-6 /K, and 6.9 X 10-6 /K along the a-axis and c-axis respectively. As the values along the a and c axes are very near it signify slight anisotropy in CTE along different crystallographic directions. Since polycrystalline ZrB_2 contains random orientation of grains in the microstructure, it usually does not show anisotropic properties on the macroscopic level.

2.3 Several Processing Methods of common Ceramic Materials

The processing method of ceramics is crucial to ensure the desired shape, size, properties, and ability to refine the materials. Various processing steps will be discussed in this section to obtain compact ceramics employing the standard powder metallurgical processes, which includes advanced and conventional

sintering processes[29].The schematic of conventional processing method of ceramics is illustrated in figure 2-2. To confirm the faster densification, it is crucial to use agglomerate-free and finer sized high-purity ceramic powders. Often times desired amount of sinter-aid or binder is used to enhance sintering which entails efficient milling. Milling is used for two reasons: (1) to decrease the particle size with the

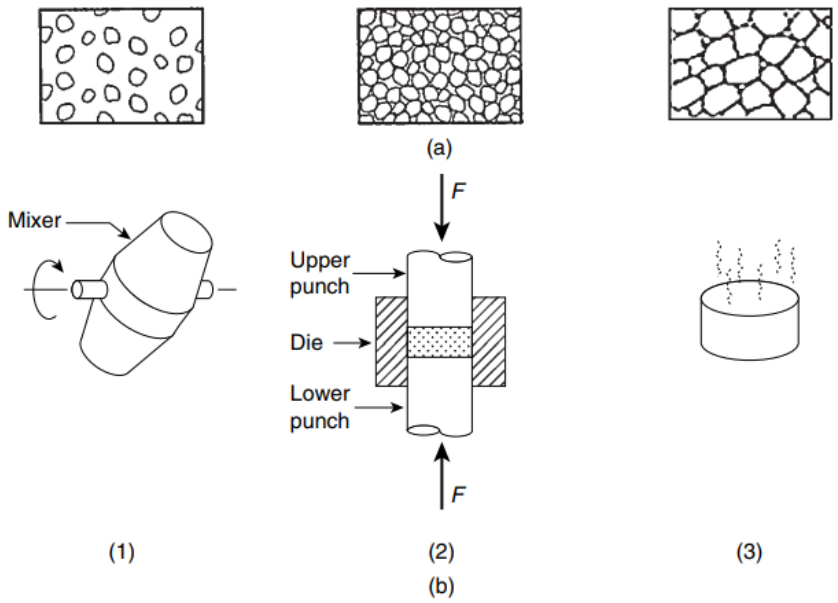

Figure 2-2 Stages involved in the conventional sintering route: (a) blending, (b) compaction, and (c) sintering[29].

starting powder feedstock and (2) to create a homogenized mixture of different phases of material with the matrix phase.

2.3.1 Ball Milling

Ball milling utilizes mixing of elemental and pre alloyed powders along with the grinding balls to cause the milling of powders, as demonstrated schematically in Figure 2-3. The grinding balls can be made of ceramics (Al_2O_3, ZrO_2), stainless steel, WC or other materials to ensure the better mixing and homogenization of ceramic powders. As the grinding balls moves at high speed, and repeatedly crushes the powder particles it leads to reduction of the particle size of ceramics powder. The physical mechanisms involve extensive deformation and subsequent fracturing of powders. During the first stage, the particles fracture due to the impact of balls and the friction between the grinding balls and particles. In the second

stage, the cold-welding takes place which causes the particles to adhere to other particle's surfaces. Therefore, the particles turn out to be spherical and their size decreases. With the continuous process of ball millin, the powders repetitively flatten, fracture, cold weld, and reweld. The flattening of particles mostly happens for ductile metals, which subsequently work harden and become brittle. In that way, continuous impacts fragment the particles. Likewise, in the case of brittle material like ceramic powder, the particles endure repeated fracture. It should be noted that the effective ball milling entails a critical speed, which is inversely proportional to the inner diameter of the mill cylinder. If the speed of a ball mill is lower than the critical speed, which leads to ball impact and causes milling, is minimal, any speed greater than the critical speed

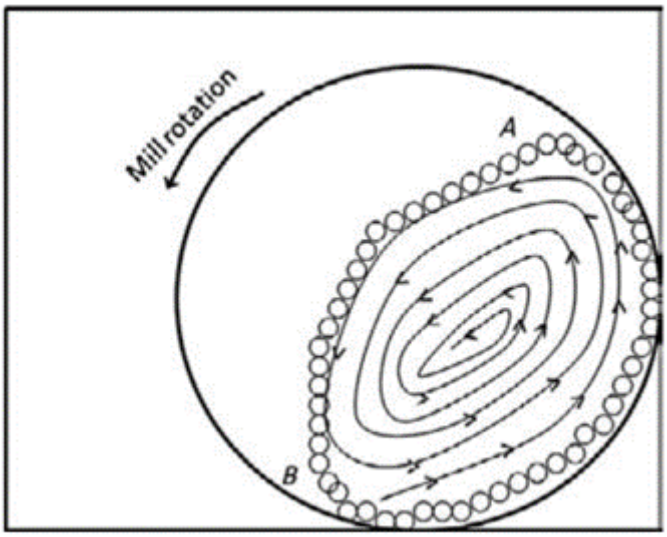

Figure 2-3 Schematic diagram of illustrating the movement of balls and powders in a typical ball mill[29].

causes the ball to revolve with the container due to centrifugal force. Therefore, only the critical speed creates cascading (frictional milling) and impacting (impact milling) of the powder media. A typical movement of the balls and powder are demonstrated in Figure 2-3. In addition, the ball-to-powder ratio (BPR) is important to achieve the desired results. In ideal case, the ratio of BPR is 4:1 for efficient milling. Increasing the density of balls and ball diameter can also lead to increase in the BPR. The BPR determines the ball milling time, which should be optimized to save cost and power.

2.3.2 Sintering

Sintering refers to the process of compacting and forming a solid mass of material by pressure or heat without melting it to the point of liquefaction. It's a process of diffusional mass transport leads to the formation of a dense body. It is a method based on powder metallurgy and produces high-density materials from ceramics or metal powders by applying mechanical pressure and/or heat. Typically, sintering process involves preparation of a powder blend which includes powder, binder or sinter additive followed by compaction and consolidation at elevated temperature (schematics shown in Fig. 2-4). Sintering involves a process of transformation from a porous state to a state of dense material and it must involve the neck formation and growth process. As illustrated in Figure 2-4, the sintering process essentially involves with the continuous and dynamic change in pore size and shape. The elimination of porosity can occur by mass transport from powder particles to porous regions either through lattice diffusion or grain boundary diffusion. It is now widely established that sintering is the only processing technique for the refractory ceramics and metals. This is due to the following factors: (1) The typical melting–solidification route, as is commonly used for metals, cannot be employed in the case of ceramics. This is due to the fact that the melting points of most of these materials lie in the range of 2000–3500°C, which requires the use of furnaces capable of operating at such extreme conditions. This is not an efficient engineering solution. (2) Because of the brittle nature of ceramics, the conventional metal-forming processes, like forging and rolling, cannot be implemented to manufacture products with preferred shapes in the case of refractory.

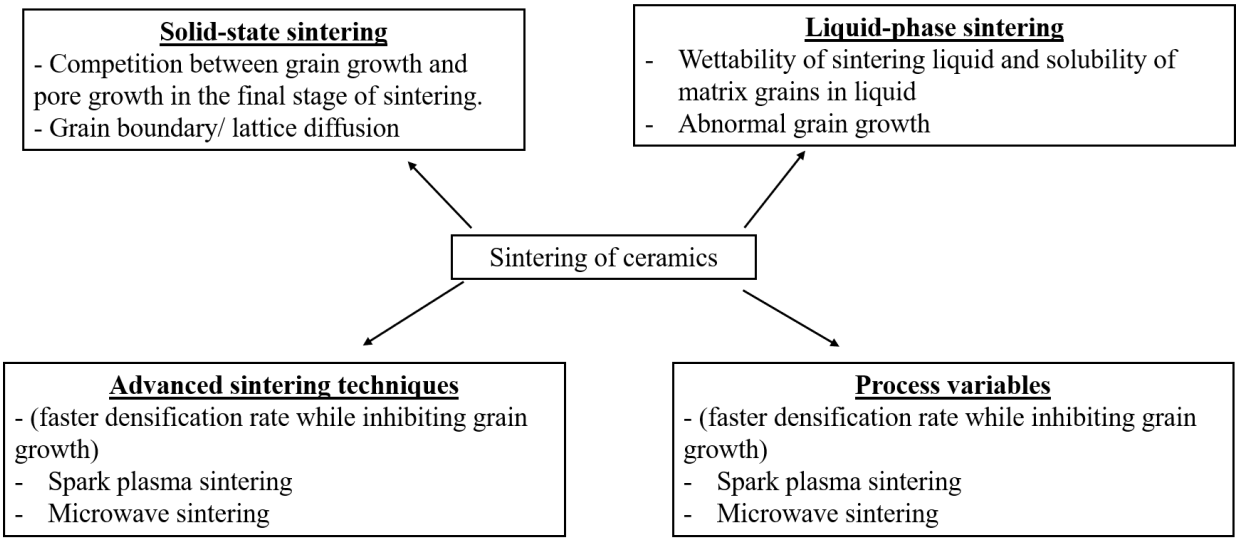

Figure 2-4 Summary of various factors controlling the sintering of ceramics as well as issues related to solid- state and liquid-phase sintering. Also, some advanced sintering techniques are mentioned[29].

Different Thermomechanical Sintering Methods: Thermomechanical treatment involves a blend of thermal and mechanical treatments to achieve superior properties of a material. Often times there is limited plastic deformation in ceramics; therefore, high-temperature treatments can cause some softening during ceramic processing. Moreover, high temperature with mechanical refinement can stimulate phase transformation, which can induce certain crystal defects in the material. As such, two degrees of freedom, such as pressure and temperature, can be played with to make the high-density components. Different techniques fall under the category of thermomechanical processing, such as hot pressing, hot isostatic pressing (HIP or HIPing), Spark plasma sintering, hot sintering etc. Those will be outlined one by one in the forthcoming sections.

2.3.3 Hot Pressing

Hot pressing is a standard compaction process which uses simultaneous application of pressure and heat to increase the overall material temperature above the recrystallization temperature. A schematic of the procedure is shown in Fig. 2-5. Hot pressing is different from the powder metallurgy technique in the way that the pressure and heat are applied simultaneously as contrast to power metallurgy methods where heat

applications are independent of the pressure applying cycle. The hot-pressing procedure can be described

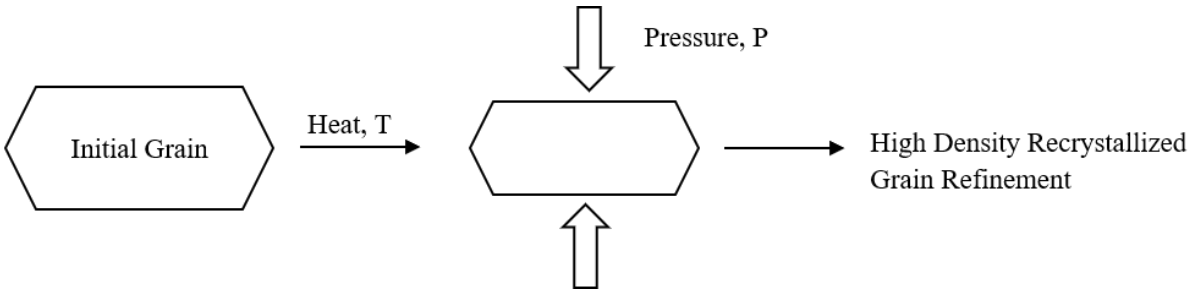

Figure 2-5 Schematic of heat and pressure involvement in the thermomechanical treatment to achieve refined grains and dense structure[29].

as follows. Ceramic powders are put into a die and are hard-pressed to ~10–50 MPa at temperatures in the range of 1000–2200°C for a certain period to attain a desired density of ceramic. 100% theoretical densities can be achieved by this technique, and often, the sintered material density is more than ~95% of the theoretical density.

2.3.4 Hot Isostatic Pressing (HIP)

Hot isostatic pressing (HIP) is a form of heat treatment that uses high pressure to improve material properties. That pressure is applied by an inert gas, usually argon. Time at elevated temperature and pressure allows plastic deformation, creep and diffusion to occur. Castings for critical applications are HIPed to eliminate internal micro porosity thereby improving mechanical properties by removing defects. Hot isostatic pressing also enables the bonding, or cladding, of two or more materials together, either in the solid or powder form. Hot isostatic pressing plays an important role in powder metallurgy and 3D printing as well. Bodycote has decades of experience creating both simple to complex components from powdered metal. These solutions dramatically reduce the manufacturing time and production cost of a part compared to producing the same part using 3D printing alone. This brings a drawback that top and bottom surfaces get compressed more when compared to the core and sides of the ceramic specimen. Therefore, the term “HIP or HIPing” evolves from the “similar” static pressure arising from a fluid (gas/liquid) around a ceramic to apply pressure from all around the sample surface The ceramic body is submerged in the chamber at high temperatures, and a high-pressure inert gas compresses the ceramic to uniformly sinter the ceramic.

Consequently, a consolidated high-density ceramic specimen can be simply attained having a homogeneous microstructure. Increased hardness and strength, reduction in porosity, and uniform microstructure are common in HIP.

2.3.5 Spark Plasma Sintering

Spark plasma sintering also known as pulsed electric current sintering is a sintering technique employing simultaneous uniaxial force and pulsed direct electrical current (DC) with low atmospheric pressure to carry out faster solidification of the powder. In this way, the heating and cooling rate is high which enhances the densification over grain growth promoting diffusion mechanisms and allows to maintain the intrinsic properties of the powders in the fully consolidated products. The process considered as a rapid sintering technique in which the heating not only dispersed over the volume of the powder compact evenly in a macroscopic scale, but also the heating power can be controlled to dissipate at the exact locations in the microscopic scale, where energy would be essential for the sintering process, specifically at the contact surfaces of the powder particles (see Fig. 2). This procedure results in a desired sintering characteristic with fewer grain growth and suppressed powder decomposition. SPS systems extend many improvements over the conventional sintering approaches by hot isostatic pressing (HIP), hot press (HP) sintering, or atmospheric furnaces, in respect of operational ease and controlling the sintering energy precisely. Also, the SPS technique enhances the high reproducibility, high sintering speed, safety and reliability.

2.3.6 Some other Processing Methods

2.3.6.1 Chemical Vapor Deposition

Chemical vapor deposition (CVD) is a combination of processes in which a solid material is deposited from a vapor by a chemical reaction occurring on or in the vicinity of a heated substrate surface. The resulting material could be in the form of a thin film, single crystal or powder. By differing experimental conditions, like substrate material, temperature, composition of the reaction gas mixture, total pressure gas flows, etc., specimens with a wide range of chemical, physical, and tribological properties can be attributed. An important aspect of the CVD method is its excellent throwing power, facilitating the fabrication of coatings

of uniform thickness and properties with minimal porosity even on substrates with complex shape. Another significant characteristic is the capability of localized, or selective deposition, on patterned substrates. CVD and other related methods are utilized in many thin film applications, including epitaxial layers for microelectronics, heat or corrosion-resistant coatings, conductors, dielectrics, oxidation barriers, passivation layers, conductive oxides, tribological coatings. Other CVD applications are the fabrication of high-temperature materials like ceramics, tungsten, etc. and the production of high-temperature fiber composites, solar cells, and particles of well-defined sizes. In this technique, oxygen activity in the vapor can be controlled precisely during the deposition, therefore, no annealing in oxygen is required to attain superconductivity.

2.3.6.2 Atomic Layer Deposition

Atomic layer deposition (ALD) is a vapor phase technique used to deposit thin films onto a substrate based on sequential, self-saturating chemical reactions. The procedure of ALD entails the surface of a substrate being subjected to alternating precursors, which do not overlap but instead are introduced in sequence. The process of ALD requires the surface of a substrate being exposed to alternating precursors, which do not overlap but instead are introduced sequentially. Two or more precursors, each comprising distinct elements of the materials being deposited, are introduced to the substrate surface separately, one at a time. Each precursor saturates the surface developing a monolayer of the specific material. Most of the commercial Atomic Layer Deposition systems are based on using inert carrier gas, e.g. nitrogen, at about 1 mbar. Short precursor chemical pulses are injected into the flowing carrier gas, followed by short purge or evacuation periods. A specific amount of material, typically a monolayer of about 1 Å, of the thin film material is grown during each ALD cycle. A conventional ALD cycle times varies from one second to several seconds. The range of the process temperature differs from room temperature to over 500 °C. Most ALD procedures run between 200 °C and 400 °C. ALD processes have been used for oxides, carbides, nitrides, certain metals,

fluorides, II–VI and III–V compounds, and recently been used for organic materials.

2.4 Processing of Zirconium Diboride Based Ceramics

Reactive hot-pressing (RHP), hot pressing, spark plasma sintering could be used to produce high purity ZrB_2 ceramics at different temperatures. Researchers have used appropriate precursor material, ball milling and sintering procedures to get their desired phase of ceramics. In this section a typical ZrB_2 fabrication procedure is described. In general, commercially available Zirconium hydride powder and amorphous boron was used to synthesize ZrB_2 ceramics. Powders were dispersed in methyl ethyl ketone by ball-milling with a dispersant and plasticizer using ZrB_2 media. A soluble phenolic resin was then added as a carbon precursor. Binder was included to compositions not containing phenolic resin to facilitate granulation. Powders were batched following appropriate design with factors being the C:O ratio with levels = 0.0, 0.5, and 1.0, and the B:Zr ratio with levels = 2.00, 2.05, and 2.10. Batch amounts were adjusted based on the reported and calculated fugitive impurities (O, 4.9 wt%, and Mg, 0.99 wt%, in B, and O, 1.5 wt%, in ZrH_2). After ball milling for several hours, slurries were dried at a temperature of 80°C, with mild vacuum condition and at a rotation speed of 120 rpm. Grinding media were weighed before and after milling to estimate contamination. Prior to hot pressing the dried powders were lightly ground and passed through a 50mesh screen prior to hot pressing. Specimen designations are RHPxy, where x values 1, 2, or 3 correspond to Zr:B molar ratios of 2.00, 2.05, and 2.10 and y values of 1, 2, or 3 correspond to C:O molar ratios of 0.0, 0.5, and 1.0. Milled powders were hot-pressed in 25.4 mm circular graphite dies lined with BN coated graphite foil. Powders were compacted at ~10 MPa and then heat is applied with a designed heating cycle.

2.5 Processing of HfO_2 Based Nanofilms

Chemical vapor deposition[31] or Atomic layer deposition[32] method can be used to fabricate the HfO_2 based nanofilms. A procedure of depositing HfO_2 layer with ALD is discussed briefly in this section [33]. HfO_2 was deposited on p-type Si wafer in which surface saturating chemical reactions between hafnium tetrachloride and water (H_2O) precursors were performed at about 300 °C. A SiO_2 thin layer formed

between HfO_2 and Si wafer because no cleaning procedure was employed before the deposition was started to the bare Si wafer. This SiO_2 interface was not considerably influenced by the ALD method. In order to carry out the proper annealing process the deposited HfO_2 thin film was then cut into 20 mm × 20 mm samples. Because of a major structural change from amorphous to crystalline phases at ~450–550 °C and current source/drain dopant activation requirements at ~900–1050 °C [33], the annealing processes were performed at 500 °C for 1 min and 900 °C for 2 min by rapid temperature annealing method with a heating rate of 50 °C/s under an argon environment. This deposited film could be used for structural characterization.

Another widely used method of fabricating HfO_2, is using chemical vapor deposition (CVD) technique. Hafnium oxide films can be deposited on silicon substrates by chemical vapor deposition using appropriate precursor, hafnium 3-methyl-3-pentoxide {$Hf[OC(CH_3)(C_2H_5)_2]_4$, Hf(mp)4}, with no additional oxygen source[34]. Hf(mp)4 is a liquid at room temperature and has a moderate vapor pressure comparable to that of hafnium tertbutoxide, Hf(OtBu)4, and a lower residual weight (<10%) in thermogravimetric analysis. The rate of the deposition was about 27 Å/min at 400 °C, and the activation energy was 68.1 kJ/mol, which is higher than those of regular hafnium alkoxide and hafnium amide precursors.

Chapter 3

Methodology

3.1 Introduction

We use an atomistic simulation approach as this method provides structure-property relations of materials at the atomic detail that is still intractable via experimental or first principle-based methods[35] . As the materials are formed from atoms and molecules – more precisely from electrons, protons, and some subatomic species, hence, the right way to determine the mechanical and physical behavior of material, either computationally or experimentally, should involve the performance assessments from the smallest scale. By using quantum-mechanical laws and explicitly including the electrons in the model, the first principle method can accurately capture thermo-mechanical, electrical, or magnetic properties of materials. However, the computational cost of this method limits its simulation capacity to hundreds of atoms. On the other hand, the scope of the experimental resolution is currently limited to capture the discrete lattice phenomena either spatially or temporally. The first issue of the experimentation methods deals with the imaging conditions. For example, different phenomenon's like elasto-plastic transition, dislocation transmission, grain boundary sliding, defect formation, dislocation incorporation to boundaries and dislocation multiplication at the matrix-grain boundary interfaces could be particularly challenging to capture given the fact that they occur over several atomic layers. As a result, molecular level modeling and simulation becomes vital to identify the mechanics of those dynamics in nanodevices. In this chapter, an overview of atomistic modeling will be presented followed by a brief discussion of the simulation procedures.

3.2 Molecular Dynamics Simulation

3.2.1 Essential Concepts

Molecular dynamics (MD) is a computer simulation technique that permits to predict the time evolution of interacting particles like atoms, molecules, granules, etc. Atoms are considered as the basic particles

disregarding nuclei or electrons in MD simulation[36]. Atom is represented as a sphere with a point mass in the center. Therefore, the role of the electron is ignored, and the electronic wave function is approximated with the current configurations of the atoms. In this way the computation becomes overly simplified as the electrons are not considered as a separate entity in Molecular Dynamics simulation. However, we need to generate the empirical interatomic potential to consider the effect of the electrons and to define the interaction between atoms. There are several steps to follow for carrying out the molecular dynamic's simulation.

First, for setting up the simulation, one needs to define:

- Initial positions and velocities of all the particles in a particular system.
- Potential that defines the forces among all the intearcting particles.

Second, by solving equations of motion in classical mechanics, the time evolution of the system can be updated for all particles in the system. The equations of motion that govern the motion of classical particles are the ones that correspond to Newton's second law of motion.

$$m\frac{d^2 r_i}{dt^2} = F_i(r_1, r_2, r_3 \ldots . r_N), \qquad i = 1,2, \ldots, N \tag{3.1}$$

Here, r_i represents the position vectors and F_i depicts the forces acting upon the N particles in the system. The forces acting on the ith atom can be derived from potential functions, $\mathrm{U}((r_1, r_2, r_3 \ldots . r_N))$, which usually portrays the potential energy for a specific system of interacting particles:

$$F_i(r_1, r_2, r_3 \ldots . r_N) = \nabla r_i \times \mathrm{U}((r_1, r_2, r_3 \ldots . r_N)), \qquad i = 1,2, \ldots, N \tag{3.2}$$

The equation signifies the total energy conservation of the system, $\mathrm{E} = \mathrm{E_{Kin}} + \mathrm{U}$, where $\mathrm{E_{Kin}}$ is the instantaneous kinetic energy. In case of the absence of externally applied forces, the potential energy can be formulated as a sum of pairwise interactions:

$$U = \sum_{i=1}^{N} \sum_{j>1}^{N} u(r_{ij}) \tag{3.3}$$

Here, $r_i = r_i - r_j$, $r_{ij} \equiv |r_{ij}|$, and the condition j > i inhibits the twice counting of interaction between particle pairs. Also, the forces are calculated with the basis of individual interactions with rest of the atoms:

$$F_i = \sum_{j \neq i}^{N} f_{ij}, \qquad f_{ij} = \frac{du(r_{ij})}{dr_{ij}} \frac{r_{ij}}{r_{ij}} \tag{3.4}$$

Newton's third law, $f_{ij} = -f_{ji}$ is used to reduce the computation in half. A cutoff radius is imposed in the simulation to further reduce the computational cost beyond which the potential becomes insignificant. Now, for a substantially larger system, it's almost impossible to attain a direct solution for the Equation of Motion (EOM), and therefore, those equations are solved by finite difference methods. One of the most used methods is known as *Verlet Leapfrog (LF)* integration scheme[36]. This method needs the numerical values of position (***r***) and force (***f***) of each atom at time *t* while the velocities (***v***) remain half a timestep behind. For a particular time, the velocities are advanced to $t + (1/2)\,\Delta t$ by the integration of force:

$$\vec{v}\left(t + \frac{1}{2}\,\Delta t\right) = \vec{v}\left(t - \frac{1}{2}\,\Delta t\right) + \Delta t\,\frac{\vec{F}(t)}{m} \tag{3.5}$$

where *m* represents the mass of an atom and Δt represents the timestep. The positions are then updated using the latest velocities:

$$\vec{r}\left(t + \frac{1}{2}\,\Delta t\right) = \vec{r}\,(t)\left(t - \frac{1}{2}\,\Delta t\right) + \Delta t\,\frac{\vec{F}(t)}{m} \tag{3.6}$$

As the MD simulation usually requires position and velocity simultaneously, therefore, the velocity at time t is approximated with the average of velocities half a timestep either side of time t:

$$\vec{v}(t) = \frac{1}{2}\left[\vec{v}\,(t)\left(t + \frac{1}{2}\,\Delta t\right) + \vec{v}\,(t)\left(t - \frac{1}{2}\,\Delta t\right)\right] \qquad 3.7$$

3.2.2 Simulation Procedure

In general, MD simulation runs through initialization, integration, and data production. To start the MD run and get meaning results from the simulation, several steps needs to follow. The schematic diagram in Fig. 3-1 illustrates a standard MD simulation outline. First step is the initialization, at the initialization the model needs the information about the initial positions and velocities of every particles. Then it calculates the interaction(forces) based on force-energy empirical relation between the particles based on spatial coordinates. Then it goes to next part where it involves integrating the Equation of Motion to get updated positions and velocities of the system. The force calculation part required most of the time of MD simulations. The following sections describe the procedures of implementing that information in MD simulation.

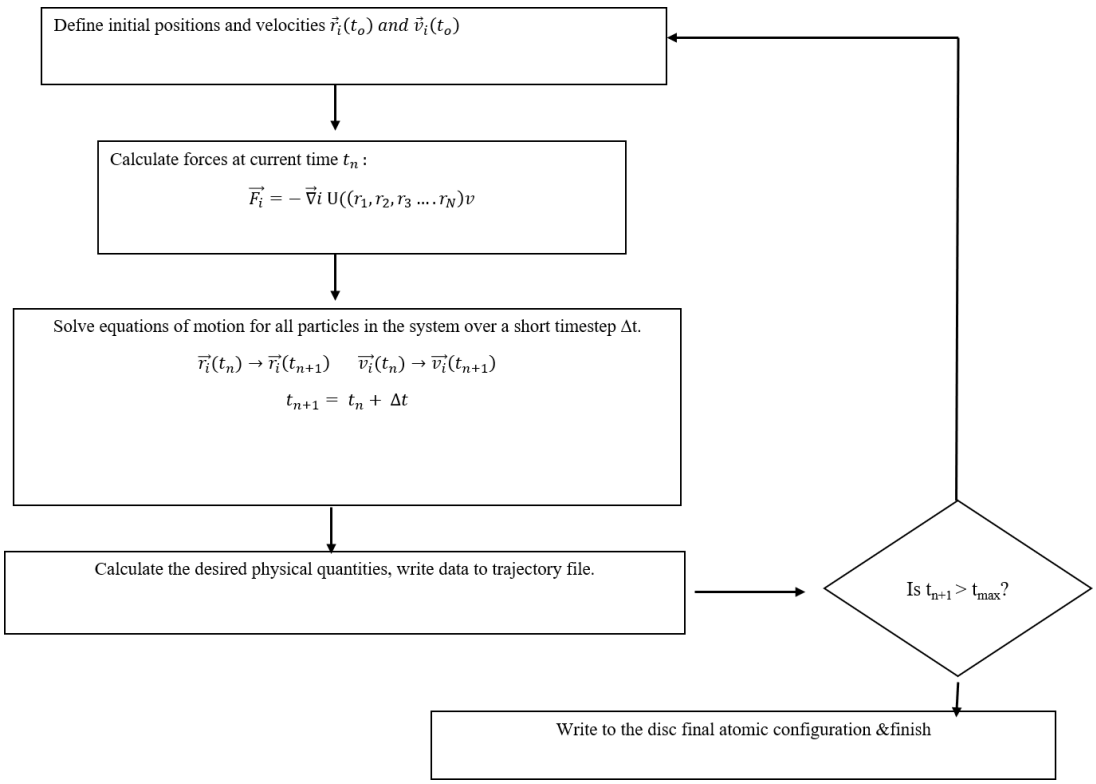

Figure 3-1 Schematic diagram of Basic MD Simulation

3.2.2.1 Defining Initial Positions and Velocities of Particles

To get started with MD simulation, the initial positions and velocities must be specified for all atoms in a system. The instantaneous positions and velocities are required to solve the Newton's law of motion. The initial position can be identified from the known lattice positions for a crystallographic system. The initial velocities of particles could be determined from a Maxwell–Boltzmann or Gaussian distribution at a specific temperature value. For instance, the probability that an atom has a velocity ***v*** at an absolute temperature *T* is

$$P(v) = \left(\frac{m}{2\pi K_B T}\right)^{\frac{1}{2}} \exp\left(-\frac{mv^2}{2K_B T}\right) \quad 3.8$$

where K_B represents the Boltzmann constant. In addition, the directions of velocities are selected randomly to create the zero value of total momentum.

3.2.3 Force Field

A force field is a mathematical expression that describes the relation between the energy of a system and the positions of its particles. It comprises of an analytical form of the interatomic potential energy, U (r1, r2, ... , rN), and a set of variables entering into this equations. The parameters are usually taken either from fitting to experimental data such as X-ray or electron diffraction, Infrared, Raman spectroscopy, NMR etc or from the ab initio or quantum mechanical calculations. Molecules are basically defined as a set of particles that is kept together by simple elastic forces and the Force Field substitutes the true potential with a simplified model that is acceptable in the system being simulated. Ideally it should be a simple model to be evaluated quickly, but adequately detailed to replicate the properties of interest of the system analyzed. In the literature, many potentials are available with different degrees of complexity and focused on treating different kinds of systems. However, a conventional form of a potential may look like this:

$$U = \sum_{bonds} \frac{1}{2} K_b (r - r_o)^2 + \sum_{angles} \frac{1}{2} K_a (\theta - \theta_o)^2 + \sum_{torsions} \frac{V_n}{2} [1 + \cos(n\emptyset - \delta)] + \sum_{improper} V_{imp} + \sum_{LJ} 4\varepsilon_{ij} \left(\frac{{\sigma_{ij}}^{12}}{{r_{ij}}^{12}} - \frac{{\sigma_{ij}}^{6}}{{r_{ij}}^{6}} \right) + \sum_{elec} \frac{q_i q_j}{r_{ij}}$$

where the first four terms denote the intramolecular contributions to the total energy, like bond stretching, angle bending, dihedral and improper torsions, and the last two terms represents the Van der Waals interactions (here, it is a 12-6 Lennard-Jones potential) and the Coulombic interactions.

3.2.3.1 Pair Potential

Among all forcefields, the pair potential is the simplest choice where the potential energy can be calculated from the sum of energy contributions between the pair of atoms. In a system where the number of atoms is N, an atom i interacts with other atoms and the interaction can be expressed as

$$U = \sum_{i<j}^{N} U_2 (r_i , r_j) + \sum_{i<j<k}^{N} U_3 (r_i , r_j , r_k) + \cdots \quad 3.9$$

where the terms are potentials for two atoms, three atoms, and so forth, respectively. Here, the summation notations indicate sums over all distinct pairs, triplets, and so forth without double counting any of the atoms. Now, considering the interaction between two-atom pair interactions, where (N – 1) interactions per atom, and thus the number of pairs N_{pair} , is on the order of N^2

$$N_{pair} = \frac{(N-1)N}{2} \propto O(N^2) \quad 3.10$$

Figure 3-2 shows the 10 pair interactions in a system of five atoms. Pair potentials are considered as a simplest form of a potential that reflects only two-atom interactions and disregards the other interactions. A classic example

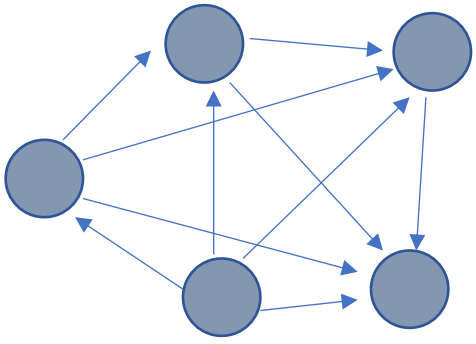

Figure 3-2 Pair interactions represented by the arrows in a five-atom system.

is the Lennard-Jones potential[36], $U_{LJ}(r)$, stated in terms of interatomic distance, r, with the following two parameters:

$$U_{LJ}(r) = 4\varepsilon\left[\left(\frac{\sigma}{r}\right)^{12} - \left(\frac{\sigma}{r}\right)^{6}\right] \quad 3.11$$

where:

parameter ε portrays the lowest energy of the potential curve that is equivalent to the well depth in the plot of Lennard- jones potential , parameter σ is the interatomic distance where the potential is zero as shown in Figure ... From here, the force form can be obtained as:

$$F_{LJ} = \frac{24\varepsilon}{\sigma}\left[2\left(\frac{\sigma}{r}\right)^{13} - \left(\frac{\sigma}{r}\right)^{7}\right] \quad 3.12$$

Several aspects can be highlighted here when two Lennard-Jones particles for example, inert element Ar, move towards each other from a long distance: At $r = \infty$, U_{LJ} and $\boldsymbol{F}$ are zero. When they get close enough, the dipole–dipole attraction takes place, and this term best describes the van der Waals interaction. When the atoms are very close to each other, due to overlapping electron clouds, a strong repulsion takes place. and the arbitrary r-12 term expresses this sharp increase in the repulsion.

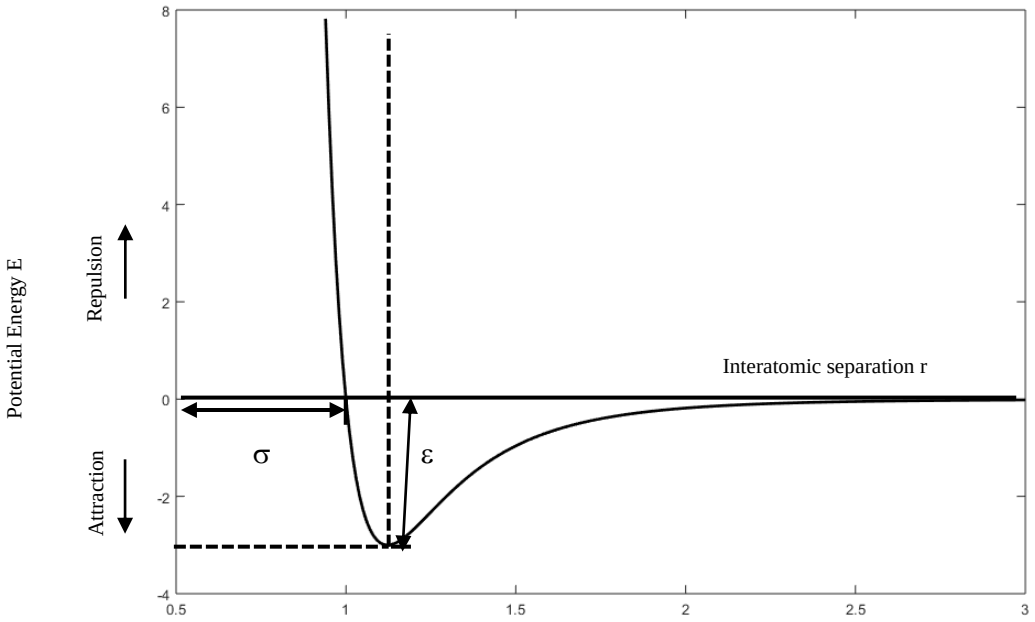

Figure 3-3 Schematic representation of Lennard-Jones potential

3.2.3.2 Tersoff potential

The Tersoff potential is a many body potential functional which explicitly incorporates an angular contribution of the force. At present, the potential is extensively used in numerous applications for silicon, germanium, carbon etc. Diamond or zincblende structures belong to the group of covalent solids and have the bond angle of ~109.47° and bonds of the sp^3 hybridization of orbitals. Therefore, bond angle and bond order are the primary characteristics of these types of material. The strength of a bond between two particles relies on the local environment such as coordination number and bond angle. Tersoff[37] identified this geometrical fact and developed a potential as the following expression:

$$U_{Tersoff} = \frac{1}{2}\sum_{i \neq j} U_R(r_{ij}) + \frac{1}{2}\sum_{i \neq j} B_{ij}\, U_A(r_{ij}) \qquad 3.13$$

where: U_R and U_A are repulsive and attractive potentials, B_{ij} represents the bond order for the bond between particle i and j, which is typically a diminishing function of the coordination number, N_{coor}, as

$$B_{ij} \propto \frac{1}{\sqrt{N_{coor}}} \quad 3.14$$

In other words, the bonding B_{ij} of atom i with atom j is decreased by the existence of another bond B_{ik}. The degree of diminishing depends on other bonds position and angle. Even though both terms depend only on position, this type of potential typically has more than six variables to be fitted. This potential has performed quite well with a good parameterization and has been used to simulate various covalently bonded solids such as diamond, graphite, amorphous carbon, Si, SiC, ZrB_2, HfB_2 and hydrocarbons etc.

3.2.3.3 Charged Optimized Many Body Potential (COMB)

The COMB potential is a variable charge potential[38] and an extended form of Tersoff potential for semiconductors. By using the electronegativity equalization method, the equilibrium charge for each atom is determined. Different types of bonding like metallic, ionic, and covalent are present in many devices that combine the functionality of different material system. In metallic bonding the electrons are shared with all the atoms quite uniformly. By contrast, the ionic bonds are created by transferring the electrons from one atom to another while covalent bonds are created by sharing of electrons between two atoms [39]. Density Functional Theory (DFT) methods illustrate these differences clearly. While classical empirical potentials used in MD simulations do not explicitly describe the electrons, they do incorporate surrogate quantities that account for the influences of electrons on material bonding. Traditional potentials have been developed to take into account for one type of bonding only, whereas the COMB potential permits the seamless simulation of devices composed of dissimilar materials. This is possible because COMB incorporates a charge equilibration technique that allows each atom to autonomously and dynamically calculate its charge, and a sophisticated description of bond order, by which the strength of an individual pair bond is modified by the presence and strength of other neighboring bonds. Compared to electronic-structure, simulations using COMB potentials are orders of magnitude faster, can simulate much larger systems and can easily consider dynamic behavior[39]. The total energy expression illustrating the COMB potential, E^{comb}, can be written as

$$E^{comb} = E^{self} + E^{Coul} + E^{polar} + E^{vDW} + E^{bond} + E^{other} \quad 3.15$$

Here, E^{self} represents the energy corresponding to the ionization of an atom, E^{Coul} is the Coulombic interaction between ions, E^{polar} is the dipole and higher order electrostatic interactions, E^{vDW} is the Van der Waals interactions, E^{bond} is the bond-order energy and E^{other} is used to illustrate very specific bond angle configurations. The key term involved in the self-consistent charge equilibration is the self-energy, that can be written as:

$$E^{self} = \sum_{i=1}^{N} \chi_i q_i + \frac{1}{2} J_i {q_i}^2 \quad 3.16$$

Here J_i is the chemical hardness and χ_i represents the electronegativity of species i. The self-energy term imposes a relative difference in energy cost for different charge states of a element.

3.2.4 Controller

After setting up the force fields, one needs to setup the virtual test environment to carry out the MD simulation which is done by "controllers". Molecular dynamics simulation uses the theories of statistical mechanics which explains how the macroscopic observables such as pressure, heat capacities, energy, etc. controls the microscopic behavior of a system. From statistical mechanics point of view, the major elements of "controllers" are a set of thermodynamic variables that are collectively known as ensembles. Also, an ensemble can be described as a compilation of all possible systems with different microscopic states but have an identical macroscopic or thermodynamic state. There are three main ensembles that are broadly used in MD – namely, NPT, NVT, and NVE ensembles. Figure. 3-4 illustrates how those ensembles are employed in MD.

The NVT ensemble known as microcanonical ensemble has a fixed number of atoms (N), box volume (V), and total energy (E) and is an isolated system which does not exchange any matter or energy with its surrounding environment. This ensemble is often used in MD because it represents the real systems at its

best. The equation of motion for the particles is the usual Newtonian equation for this NVE ensemble. As demonstrated in Figure 3-4, all other ensembles are artificially surrounded by large external systems to control the fixed parameters. The canonical ensemble has a constant number of atoms(N), box volume(V), and temperature (T) and is also used in the Monte Carlo simulation methods. The isothermal–isobaric ensemble fixes the number of atoms(N), pressure (P), and temperature(T), and nearly traction free boundary condition can be obtained from NPT ensemble[40]. whereas the grand canonical ensemble fixes chemical potential (μ), volume, and temperature, and the number of atoms is allowed to change.

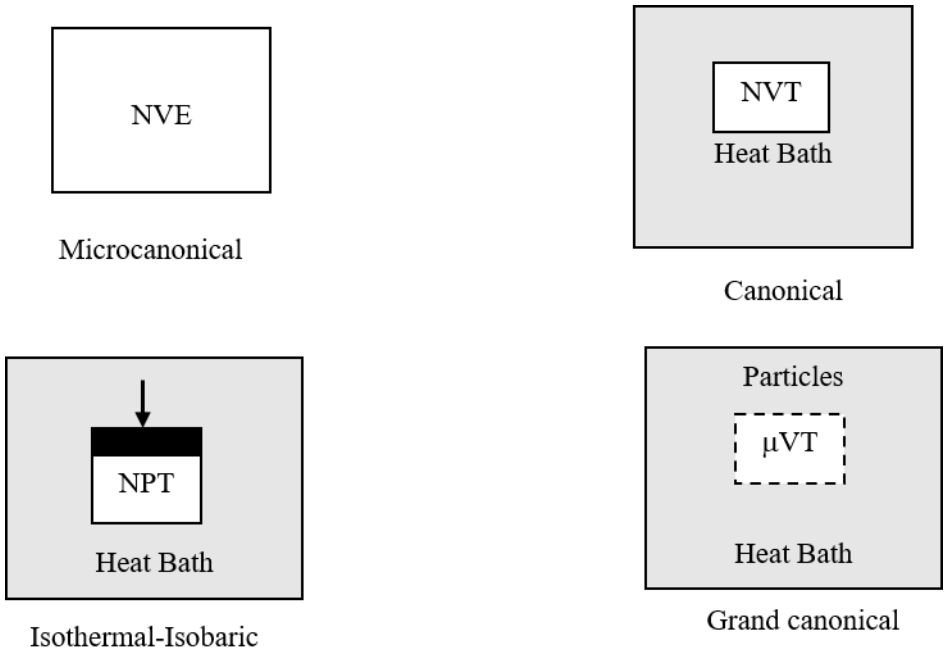

Figure 3-4 Schematics of four ensembles adopted in MD[36]

A successful MD simulation creates a trajectory of positions, velocities and forces on each particle involved, that can be converted to various thermodynamic parameters such as temperature, pressure, energy etc. with the implication of statistical mechanics. The major constraint of using MD for many situations, is the limitations of using this method in different time and length scales. Even these days by using high-speed supercomputing facilities with the modern MD codes which can perform massively parallel computations, the largest system that can be simulated is comprising few billions of atoms. The largest time scale is also

restricted to ~Ns range indicating that MD is unable to capture any long-term actions. The reason behind the restrictions in total simulation time is related with the size of timestep, which in turn is restricted mostly by three reasons [33], (1) numerical stability, (2) van der Waals collision (3) local resonance[40]. Among them, the numerical instability is believed as the major factor that evolves when a specific selection of timestep creates a diverging error pattern during the simulation. By considering a simple one-dimensional harmonic oscillator case, it is observed that the biggest timestep 'T must be smaller than the reciprocal natural frequency of the oscillator.

3.2.4.1 Strain

In Molecular Dynamics, stress-strain curve for any system of interest can be obtained via equivalent "displacement-controlled" mode. In order to displace a 3-dimensional periodic model, uniform strain field is attained by incrementally scaling the subsequent unit cell and the atomic positions of all the particles towards the preferred direction. Here, all strain fields represent the engineering strains unless specified otherwise. In addition, at every time step the incremental strain field is not applied. Entire model is equilibrated for 3000 times steps prior to applying the following strain field. The process continues until a representative stress-strain behavior is attained. Mostly NVT ensemble is used to carry out the equilibration process. When a 2-dimensional periodic system is considered, like studying the thin films, where the loading planes are the two non-periodic faces, then in-plane surface atoms are only displaced in agreement with desired deformation and the other atoms are changed their subsequent position dynamically.

3.2.4.2 Stress

Local atomistic stresses can be calculated in several ways in MD simulation by using methods developed by researchers like virial stress[41], hardy stress[42], Irving and Kirkwood method[43] etc. The virial stress is the atomistic representation of stress that is equivalent to the Cauchy stress in continuum scale[41]. The virial stress is the mechanical stress if the correct spatial and temporal averages are considered in an Eulerian reference frame. Both potential and velocity terms are required to correctly quantify the value of

virial stress. The following expression explains the stress tensor for atom I, where a and b take on values x, y, z to create the components of the tensor:

$$S_{ab} = -mv_a v_b - W_{ab} \tag{3.17}$$

The negative sign represents the tensile stress as a positive quantity (In general, in MD, compression is considered as positive). The first term states the kinetic energy contribution for particle I whereas, the second term is the virial contribution for intra and intermolecular interactions. The details of the computational expression are stated below.

$$\begin{aligned} W_{ab} = \frac{1}{2}\sum_{n=1}^{N_p}(r_{1a}F_{1b} + r_{2a}F_{2b}) + \frac{1}{2}\sum_{n=1}^{N_b}(r_{1a}F_{1b} + r_{2a}F_{2b}) \\ + \frac{1}{3}\sum_{n=1}^{N_a}(r_{1a}F_{1b} + r_{2a}F_{2b} + r_{3a}F_{3b}) \\ + \frac{1}{4}\sum_{n=1}^{N_d}(r_{1a}F_{1b} + r_{2a}F_{2b} + r_{3a}F_{3b} + r_{4a}F_{4b}) \\ + \frac{1}{4}\sum_{n=1}^{N_i}(r_{1a}F_{1b} + r_{2a}F_{2b} + r_{3a}F_{3b} + r_{4a}F_{4b}) + K_{space}(r_{ia,}\, F_{ib}) \\ + \sum_{n=1}^{N_f}(r_{ia}F_{ib}) \end{aligned} \tag{3.18}$$

The first term states a pairwise energy contribution where n loops over the N_p neighbors of atom I, r1 and r2 are the positions of the 2 atoms in the pairwise interaction, and F_1 and F_2 are the forces on the 2 atoms resulting from the pairwise interaction. The second term is a bond contribution of similar form for the N_b bonds which atom I is part of. There are similar terms for the N_d dihedral, N_a angle and N_i improper interactions atom I is part of. There is also a term for the K_{space} contribution from long-range Coulombic interactions, if defined. Finally, there is a term for the N_f fixes that apply internal constraint forces to atom I. The local atomistic stress, global stress (the whole volume-averaged virial stress) and continuum stress, are supposed to be identical for a perfect crystal subjected to uniform loading.

Chapter 4

Nano Composites of ZrB_2 and ZrC

4.1 Potential application

Because of their structural stability at temperatures exceeding 2000 ^oC, many transition metal ceramics such as hafnium diboride (HfB_2), zirconium diboride (ZrB_2), zirconium carbide (ZrC), titanium carbide (TiC) and their composites have been regarded as ultra-high-temperature structural ceramics (UHTCs) [1-20]In addition to their structural stabilities at high temperatures, UHTCs exhibit many excellent physical and mechanical properties such as ultra-high hardness, high melting point, low density, excellent wear resistance, high refractoriness, high electrical and thermal conductivity, chemical inertness against molten metals, etc. Of these, ZrB_2 and its composites have been studied more extensively [11–20]. because of their potential application in hypersonic aerospace vehicles [1–5].To improve oxidation resistance, thermal stability and mechanical properties, other ceramic phases such as ZrC and silicon carbide (SiC) are often added to ZrB_2[11–20]. Reactive hot pressing and pressureless sintering methods [7–20,21,22] are primarily used to process these materials.

As outlined in [30] and referenced therein, the flexural stiffness and flexural strength of ZrB_2 and its composites largely depend on the porosity and presence of sintering additives. For example, the highest measured flexural modulus of 99.8% dense ZrB_2 is found to be 489 GPa [57]. Using single crystal ZrB_2 modulus measurement data, Okamoto et al. [65] calculated the elastic (tensile) modulus of polycrystalline ZrB_2 as 525 GPa, which is very consistent with the first principle calculations (~520 GPa)[66] . The effect of adding second phases to ZrB_2 appears to give a surprisingly inconsistent effect on modulus properties [26–29] For instance, while small additions of boron carbide (B_4C) and/or carbon (C) increase the elastic modulus of ZrB_2 [26,27] additions of AlN and Si_3N_4 lower the elastic modulus [69][70]. The evolution mechanisms of the additives within the microstructure of ZrB_2 act as the driving force for modulus enhancement or degradation of ZrB_2. For instance, additives such as C and B_4C can eliminate low modulus impurities (e.g., surface oxides) [26,27], which, in turn, can lead to a modulus increase. On the other hand, additives such as aluminum nitride (AlN) and silicon nitride (Si_3N_4) promote formation of low modulus

grain boundary phases [29-28], which eventually lead to modulus reduction. The strength (tensile or flexural) of ZrB_2 are greatly affected by the presence of flaws, grain size and additive concentrations [7, 10, 30–36]. In principle, tensile strength and flexural strength of homogenous and isotropic material should be the same [37,39]. The location and distribution of flaws within a material can lead the material to fail at different strengths when tested in tension and bending. This is because when a material is tested in bending, only the surface layers of the material experience the highest normal stresses (tensile in one side or compressive on the other side. As such, flexural strength of a material is primarily controlled by the strength of the outside layers, However, when material is tested in tension, then, all the layers in the material experience same level of stress. As such, failure in that material initiates when the weakest layer within the material reaches its limiting tensile strength. Therefore, materials with higher level of "interior" defects typically have higher flexural strengths than tensile strengths. On the other hand, materials containing predominantly "surface" defects generally have higher tensile strengths than flexural strengths.

The highest tensile strength of ZrB_2, also regarded as the ideal/theoretical tensile strength, is observed in defect-free single crystal ZrB_2 [21, 39 - 40]. Depending on crystallographic orientations, the tensile strength of single crystal ZrB_2 appears to vary between ~40 and ~55 GPa[63]. The strength values are estimated from the critical failure energy density principle-based and the critical strain principle-based computational models [63]. Zhang et al [80] and Samvedi and Tomar [82] independently computed the tensile strength of ZrB_2 using first-principle calculations and ab-initio molecular dynamics, respectively, and obtained consistent values. The flexural strength of polycrystalline ZrB_2, depending on the grain size and additives, typically range from 250 to 630 MPa [7, 12, 30–36]. Although the general trend suggests that strength of ZrB_2 is inversely proportional to its grain size, the complex microstructure-mechanical property relations of ZrB_2, processing parameters, presence of impurities, and subtleties in the measurement methods often limit quantitative determination of actual deformation mechanisms and structure-property relations. Because the size of the particulate reinforcing phase controls the strength, a uniform dispersion of additive particles is essential to maximize strength, which is often very difficult to achieve. The presence of impurities such as oxides or amorphous carbon particles also affect strength. It is generally argued [42–46]

that grain crazing near grain boundaries, grain boundary strengthening, and impeding grain boundary shear are critical factors in retaining overall strength in ZrB_2 and its composites. It is, however, extremely difficult to capture such dynamic events using currently available experimental tools.

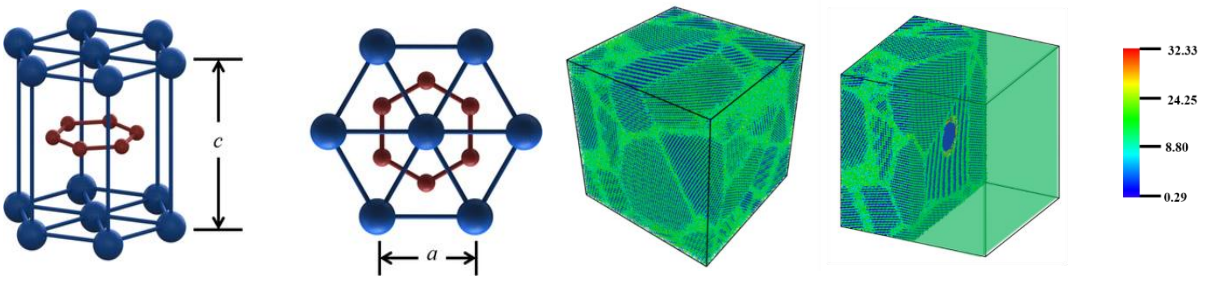

Figure 4-1 The crystal structure of ZrB2 is built on a primitive hexagonal and the simulation model of a) polycrystalline ZrB2 and b) ZrC-ZrB2 nanocomposite

In this study, we report the grain boundary driven mechanical behavior of polycrystalline ZrB_2 and ZrC-ZrB_2 nanocomposites. We use an atomistic simulation approach as this method provides structure-property relations of materials at the atomic detail that is still intractable via experimental or first principle-based methods [47]. Here, atomistic models of ZrB_2 and ZrC-ZrB_2 nanocomposite have been subjected to tensile loading to determine their elastic constants and strengths. Tensile and shear simulations are also conducted solely on a comparison of the crystal grain boundary material with crystalline properties to determine their role in the overall mechanical behavior of ZrB_2 and its nanocomposite.

4.2 Molecular models and simulation procedure

The crystal structure of ZrB_2 is built on a primitive hexagonal (AlB_2-type, *P*6/*mmm* space group) lattice with nominal lattice constants a = 3.17 Å and c = 3.53 Å. Figure 4-1 shows the crystal structure of ZrB_2. Two different atomistic models with a simulation box size of 21.9 × 21.9 × 21.2 nm were developed in this study. The first type represents the polycrystalline ZrB_2 with 12 grains (made with a total of 1,027,538 atoms) where grain sizes and orientations were randomly determined using the three-dimensional Voronoi construction method [47, 48]. A Voronoi tessellation or diagram is a cell structure constructed from randomly positioned points, also referred to as Poisson points. For polycrystalline material, we can think of these points as grain nucleation sites where the solidification starts and then uniform outward grain

growth occurs in all directions. The solidification front continues to expand until it interacts with other adjacent fronts to create a grain boundary. In geometrical terms, the grain boundary is obtained by introducing lines perpendicular to lines connecting neighboring Poisson points. The result is a set of convex polygons/polyhedra. In sample type two, one spherical ZrC nanoparticle (NP) with a nominal diameter of 6 nm is inserted within ZrB_2 as a rigid inclusion. To capture the effect of NP location within a ZrB_2 microstructure, three separate models are built. In Model I, the ZrC NP is placed at the center of one ZrB_2 grain. In Models II and III, the NP is placed at the quadruple junction of ZrB_2 grains and on the grain boundary, respectively.

The simulation box size for this type is 21.9 × 21.9 × 21.2 nm with 1,024,328 atoms. The interactions between Zr and B have been described by the Tersoff-type potential [89] . Since the ZrC nanoparticle (NP) is regarded as rigid, no interatomic potentials are needed for Zr–C, C–C and Zr–Zr interactions. To capture the interfacial interactions between ZrB_2 and ZrC, interaction parameters between Zr_{ZrB2}-Zr_{ZrC}, B_{ZrB2}-Zr_{ZrC}, Zr_{ZrB2} -C_{ZrC} and B_{ZrB2}-C_{ZrC} atoms are required (subscripts in each atom define the ceramic phase). The parameters for Zr_{ZrB2} – Zr_{ZrC} and B_{ZrB2}–Zr_{ZrC} interactions are taken from Tersoff potential used in pure ZrB_2 simulation [87]. The B_{ZrB2}–C_{ZrC} interaction has been described by the Tersoff type potential proposed by Kınacı et al. [90]. The parameters for Zr_{ZrB2}-C_{ZrC} and B_{ZrB2}-C_{ZrC} interactions are not readily available. As such, parameters for these interactions are estimated from the available interactions between Zr and B as well as B and B, respectively. Table 4-1 shows the parameters used in our simulation. The environmental temperature is maintained at 300 K by using the Nosé-Hoover thermostat. To develop tensile and shear stress–strain curves, atomistic models were equilibrated first to attain a stress-free state; then, models were subjected to incremental tensile and shear loading. During equilibration, each simulation was run up to 30,000 time-steps in a constant temperature/constant pressure (NPT) ensemble. After attaining the stress-free state, uniaxial tensile loading was applied along the *z* direction at a strain rate of 10^{10} s^{-1} with a time step of 1 fs. The time constants for the thermostats [heat bath] and the barostats [pressure bath] were set to 1 ps. All simulations were carried out in LAMMPS [91], and the atomistic structures were visualized based

on centrosymmetric parameters using OVITO (a scientific visualization and analysis software for atomistic and particle simulation data)[64].

Table 4-1 Parameters describing the potentials for Zr, B and Zr-B

Parameter	Zr	B	B-C	Zr–B
A (eV)	3.58787×10^3	1.0619848×10^3	1.38678×10^3	1.7659542×10^3
B (eV)	3.71035×10^1	3.6767392×10^1	339.068910	4.0023041×10^1
λ (Å^{-1})	2.91078	3.955278	3.5279	3.360803944
μ (Å^{-1})	0.659036	1.190167		0.9220569
□	1	0.541	1.25724e-7	□$_{MMM}$ =1.0
n	1	21.885575	0.72751	□$_{MMB}$ = 0.2930705
c	0	0	25000	□$_{MBM}$ = 9.0588265
d	1	1	4.3484	□$_{MBB}$ = 3.5295546
h	0	0	-	□$_{BMM}$ = 0.94069107
				□$_{BMB}$ = 0.82400007
				□$_{BBM}$ = 0.17523123
				□$_{BBB}$ = 1.0
R (Å)	4.6	2.2	1.95	3.18
S (Å)	5.0	2.5	-	3.54
m	1	1	3.0	
λ_3 (Å^{-1})	1.32308	0	0	

4.3 Results and discussion

4.3.1 Mechanical properties of Polycrystalline ZrB_2 and ZrB_2-ZrC nanocomposites

Tensile tests were carried on polycrystalline ZrB_2 and ZrB_2-ZrC nanocomposites (Model III) at 300 K, as shown in Fig. 4-2. It appears from the stress-strain curve that both polycrystalline ZrB_2 and its nanocomposites deformed almost linearly up to ~ 0.02 strain (note the inset chart in Fig. 4-2). They then

deformed in a somewhat nonlinear fashion up to a strain state of 0.08 and rapidly failed in a brittle manner. The computed tensile strengths of both ZrB_2 and ZrB_2-ZrC nanocomposite are about 22 GPa. In essence, the estimated strength values are roughly half of the ideal tensile strength of ZrB_2 [21, 39–41] but at least two orders of magnitude higher than the experimentally obtained strengths of ZrB_2 (250 to 630 MPa) [27, 30, 32–35, 52, 53]. As outlined in Fahrenholtz et. al [90], the as-fabricated of ZrB_2 and ZrB_2-10 vol% ZrC composites contain flaws of different types and sizes, which most likely contribute to low mechanical strengths. Their results support the long-known observation that the failure strengths of brittle materials are typically three or four orders of magnitude below their theoretical cohesive strength [94]. Since our models do not contain any such defects, it is expected that the predicted strength would be higher than experimentally observed values.

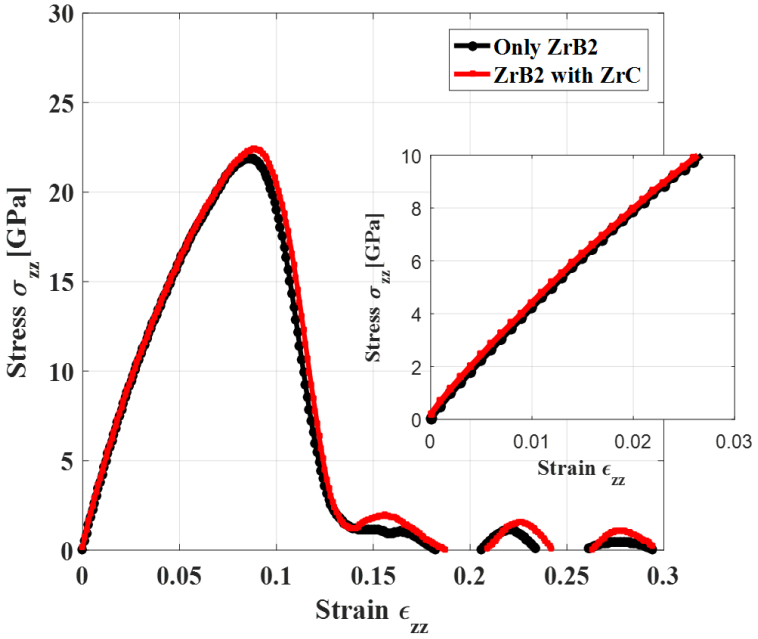

Figure 4-2 Stress-strain curves of polycrystalline ZrB_2 and ZrC-ZrB_2 nanocomposite. Inset plot shows initial part of stress-strain relation.

The estimated elastic properties of ZrB_2 and ZrB_2-ZrC nanocomposite are shown in Table 2 where Young's moduli are 322 GPa for both polycrystalline ZrB_2 and ZrB_2-ZrC nanocomposites. The predicted values are consistent with the experimentally reported values ranging between 350 and 530 GPa [37,55]. It should be noted that the grain sizes of ZrB_2 in pure ZrB_2 and in ZrB_2-ZrC nanocomposites were 1.8 µm and 1.5 µm[78]

respectively; whereas the grain size of the ZrB_2 in this work is below 10 nm. Yet, the predicted elastic properties are not significantly different from experimentally obtained values suggesting grain size has a relatively insignificant effect on the elastic response of ZrB_2. Since we conducted tensile simulation only for the polycrystalline ZrB_2 and nanocomposite model, the shear modulus properties reported in Table 2 cannot be extracted from the simulation data. However, it is reasonable to assume that polycrystalline ZrB2 and the nanocomposite system deforms like an isotropic material. Under this assumption, shear modulus can be estimated from the E and v value of ZrB_2 using the isotropic relation: G = E/2(1+v). Using the value of E and v given in Table 4-2, we computed the value of G.

Table 4-2 Mechanical properties of ZrB_2 and ZrC-ZrB_2 nanocomposite

	Elastic Constant, C11 (GPa)	Elastic Constant, C13 (GPa)	Young's modulus E (GPa)	Poisson's Ratio v	Shear Modulus* G (GPa)	Tensile strength (GPa)
Only ZrB_2	418.62	178.94	322.77	0.3	123.84	21.87
ZrB_2 with ZrC	418.62	178.94	322.77	0.3	123.84	22.56

* Estimated based on isotropic assumption, G = E/(1+v)

4.3.2 The effect of ZrC position and size on mechanical properties of ZrB_2-ZrC nanocomposite

Figures 4-3 and 4-4 show the effect of the NP location and grain size on the mechanical properties of the ZrB_2 nanocomposites. One of the reasons behind placing NP at the grain boundary junctions (Model I) or on the grain boundary (Model II) or in the grain interior (Model III) is to determine if ZrC NP location has any role on the overall deformation process. Moreover, the size of the ZrC NP has been varied from 5 to 7 nm and included at the center of the model. Finally, a cavity has been introduced replacing the 5 nm ZrC to simulate the presence of a void on the overall deformation process.

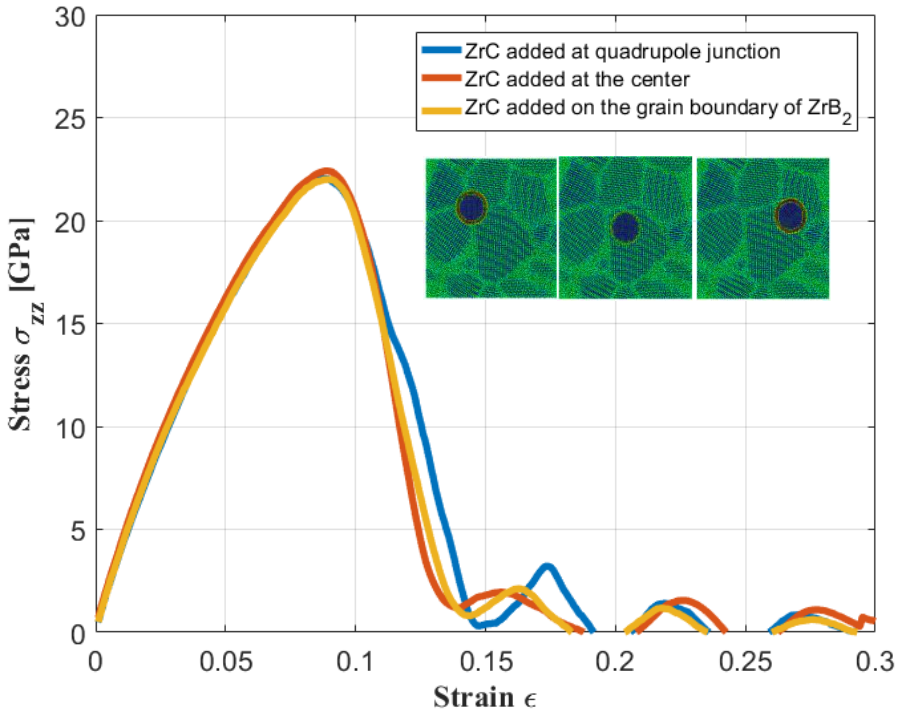

Figure 4-3 Stress-strain curves of ZrC-ZrB2 nanocomposite with different positions of ZrC

It appears from Figures 4–4 that ZrC nanoparticles have an insignificant effect on the mechanical behavior of ZrB_2 polycrystalline. To understand the underlying deformation mechanism, we referred to the atomistic snapshots taken at different strain states.

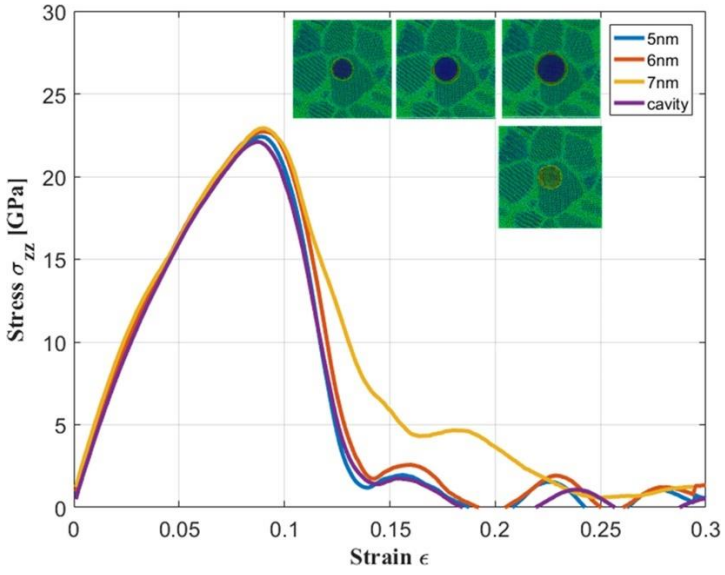

Figure 4-4 Stress-strain curves of ZrC-ZrB2 nanocomposite with different sizes of ZrC

The local stresses in each atom were calculated and are presented in Figure 4-6. The atoms are colored according to the magnitude of stress state σ_{zz}. It appears from Figure 4-6 that the magnitude of local stresses can be as high as 140 GPa, which is about 7 times higher than the strength of the material, as reported in Figure 4-2. As such, it can be argued that the failure of the material mostly initiates from areas A, B, and C where local stresses are exceedingly high compared to other locations in the structure.

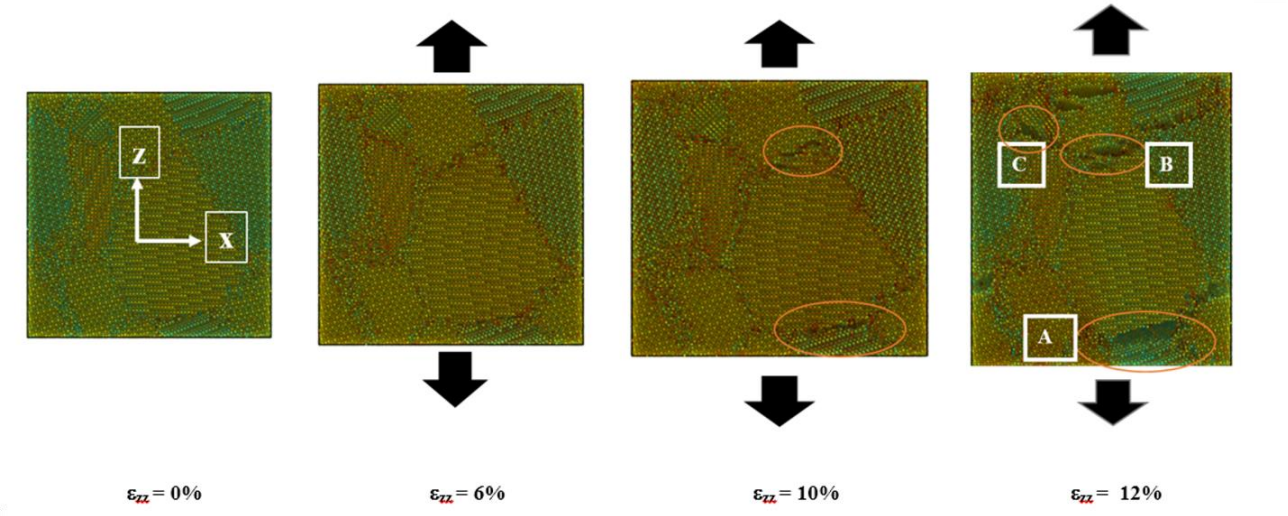

Figure 4-5 Deformed snapshots of polycrystalline ZrB_2 taken at different tensile strain states. Failure is governed by the relative atomic motion in the grain boundary regions which leads to the formation of large voids and atomic sliding events (location A,B,C)

It can also be observed that all "high-stress" zones are located near grain boundaries implying that failure is driven by the grain-boundary microstructure. The mechanical behavior of ZrC-reinforced polycrystalline ZrB_2 is shown in Figure 4-7. As previously discussed, the ZrC NP was inserted at the center of ZrB_2 as a rigid particle. Nevertheless, as illustrated in Figure 4-7, the deformation and failure mechanisms of the NP-ZrB2 system is very similar to the pure ZrB_2 system, in that both systems failed due to void formation in the grain boundary region. For 5 and 6 nm ZrC NP sizes, the failure occurs from the grain boundaries. However, for 7 nm particle size, a crack appears to initiate from the interface between NP-ZrB_2 as shown in Figure 4-7. Yet, overall mechanical properties of the material, as shown in Figure 4-4, do not alter. Hypothetically, overall failure of nanocomposites could be driven by bulk crystal failure, grain boundary failure, intra-granular fracture, inter-granular fracture or ZrC NP-ZrB_2 interfacial failure, either as

distinctive or as combined failure mechanisms. The current simulation results suggest that even though the interface between ZrC and ZrB_2 separates from each other (Figure 4-7), implying the interfacial interaction is weaker than the cohesive strength of ZrB_2, the overall deformation is dominated by grain boundary sliding. Even the presence of a cavity (equivalent to "zero" interaction between ZrC and ZrB_2) does not alter the deformation process and final strength. If the interaction between ZrC and ZrB_2 had been significantly stronger, then the failure process would surely be driven by grain boundary sliding. Such a

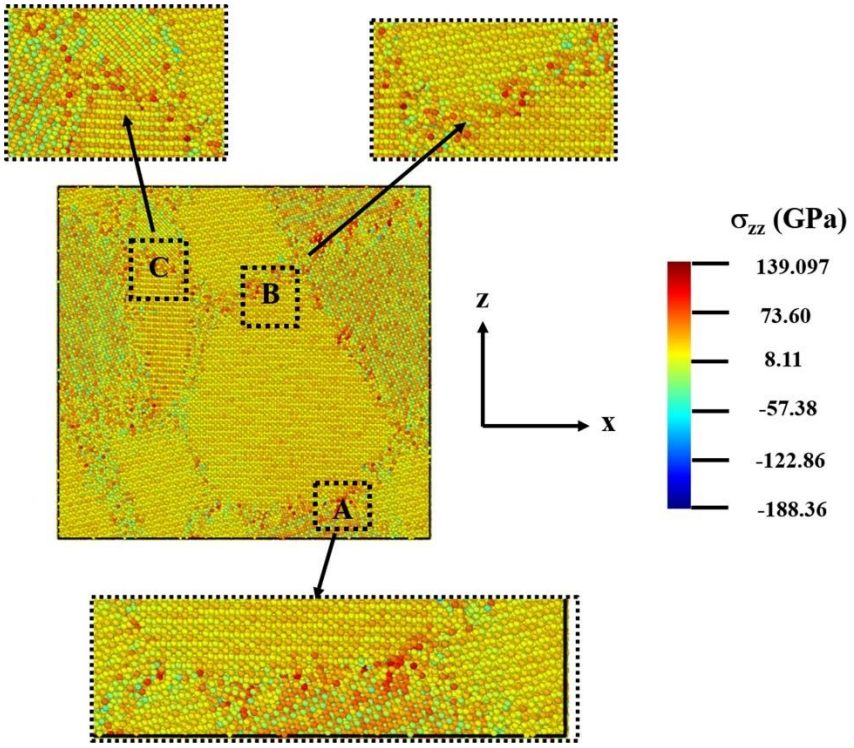

Figure 4-6 Local atomic stress plot of polycrystalline ZrB_2 loaded in tension. The corresponding strain state ε_{zz} = 6%. Failure mostly initiated from areas A, B, and C are observed in Figure 4. Highlighted areas A, B, and C in this figure reveal that local stresses in these locations are much higher than in other areas of the structure. The atoms are colored according to the atomic stress tensor (σ_{zz})

trend in results is somewhat nonintuitive as existing literature indicates that the addition of nanoparticles may degrade or enhance stiffness properties but usually enhances ceramic material strength.28

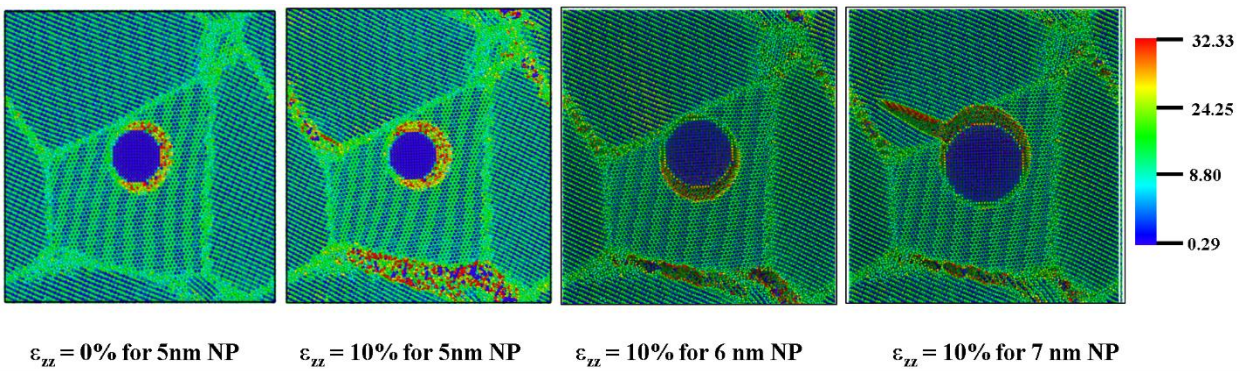

Figure 4-7: Deformed snapshots of various sized ZrC reinforced polycrystalline ZrB2 taken at different tensile strain states. Failure is dominant as noted by the void formation in the grain boundary region. All atoms are colored based on their centrosymmetric parameter

4.4 Fabrication of ZrB_2 based nanocomposites

In order to study the effect of ZrC reinforcement on mechanical behavior of ZrB_2, Neuman [81] fabricated the ZrB_2 with 10 vol% ZrC using ball milling and hot pressed sintering. For the experiment he used commercially available ZrB_2 powder (Grade B, H. C. Starck, Karlsruhe, Germany), ZrC powder (Grade A, H. C. Starck), and ZrH_2 (Grade S, Chemetall, Jackson, MI). To get the desired phase of ZrB_2-ZrC_x-C, a phenolic resin was used as a carbon precursor to help removing the surface oxides and increase the carbon's amount in the microstructure. Therefore, ZrH_2 was added to react with residual carbon and form ZrC during hot-pressing, attempting to keep the system in the ZrB_2-ZrC_x binary phase field. Then powders are measured at appropriate weights to meet the composition of ZrB_2-10 vol% ZrC, these powders were ball milled using methyl ethyl ketone environments for 8 hours to disperse the powder with ZrB_2 environments. After adding the necessary precursor and ball milling again for16 hours those mixtures were dried using rotary evaporator. Then the dried powders were lightly grounded to pass through a 50-mesh screen. Then the powders are consolidated by using a cold pressed technique by using a uniaxial press about 2 MPa. Then by using 63.5 mm square graphite dies lined with BN coated graphite the samples were hot pressed. The process involved informing applying of heat, isothermal holding and applying uniaxial pressure and cooling down to a uniform rate. The whole process was carried out in Argon environment or in vacuum. A complete description of the process was described here[30].

4.5 Experimental Characterization and Mechanical Testing of ZrB_2

Scanning electron microscopy (SEM) equipped with energy dispersive spectroscopy (EDS) was used to identify the morphology of the microstructure and correct chemical phase of the specimen. In this experiment the surfaces were polished and analyzed both as-tested and polished while the fracture surfaces were analyzed as-tested only. To eliminate furnace deposits, the as-tested specimens were cleaned by using ultrasonic technique. The SEM image of the specimen was captured after polishing the specimens were upto ~100 μm from the tensile surface by plane grounding, then polished again to achieve a 0.05 μm surface finish using diamond abrasives. A chemical etching with molten KOH was used at 200°C for ~2 s. After this the specimen SEM images were captured, and the grain sizes of ZrB_2 were measured by computerized image analysis. The grain size distribution of the ZrB_2 phase, and the cluster size distribution of the ZrC phase, were estimated by fitting ellipses to at least 1000 grains, or clusters, respectively.

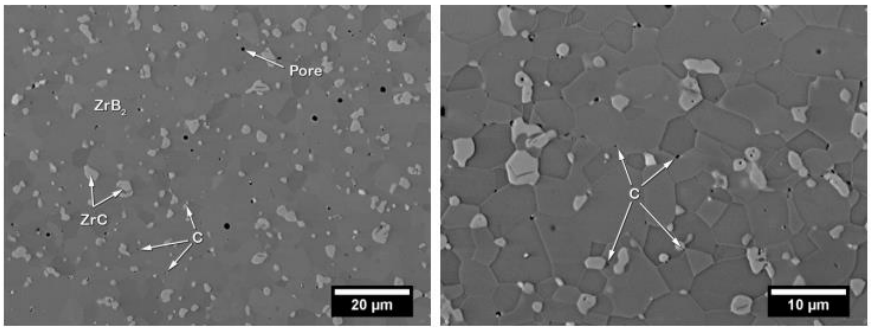

a b

Figure 4-8 SEM image of (a) polished and (b)chemically etched cross-sections of ZrB_2-10 vol% ZrC ceramic[30].

After getting the desired phase of the specimen from the fabrication process, the flexural strength, fracture toughness and elastic modulus were measured [30]. Flexure strength was measured by following ASTM C1161-02c with four-point bending using type-B bars (45 mm x 4 mm x 3 mm). ASTM C1211- 08 testing procedures were followed to measure the flexure strength at elevated temperatures. According to ASTM standard E411-04, elastic constants were calculated using the static bend test method while the elastic modulus was computed from the slope of the load displacement curves, with the beam displacement assessed from the crosshead displacement. An average value from a minimum of five readings were taken

to determine the reported numbers. According to ASTM Standard C1421-10 fracture toughness was evaluated by the chevron notch beam technique in four-point bending employing a fully articulated test fixture with chevron notch type-A bars. A heating rate of 50°C/min was used, followed by an isothermal hold of 5 min at the desired temperature for testing at elevated temperatures. A digital microscope was used to measure the notch dimensions. Five samples were used to test the fracture toughness at room temperature, whereas, for elevated temperatures three specimens were tested for each sample points.

4.6 Results

Elastic modulus was computed from the crosshead displacement throughout testing and should be considered an estimate. At room temperature the modulus of the composites was measured as 505 GPa, that is smaller than the calculated modulus of 518 GPa with the rule of mixtures employing 524 GPa for ZrB_2 and 465 GPa for ZrC. Nevertheless, A wide range of values are reported in the literature for the modulus of ZrB_2 and ZrC. For ZrB_2 the modulus is varied from 490-530 GPa and for ZrC the value is from 350-465 GPa, considering the wide range of reported values the measured value is consistent. The softening of oxide phases at grain boundaries and triple junctions could lead to the reduction of the elastic modulus. Because the ZrC lattice can accommodate a large amount of oxygen compared to monolithic ZrB_2, even it can form ZrOC phases, this may account for the less severe decrease in modulus.

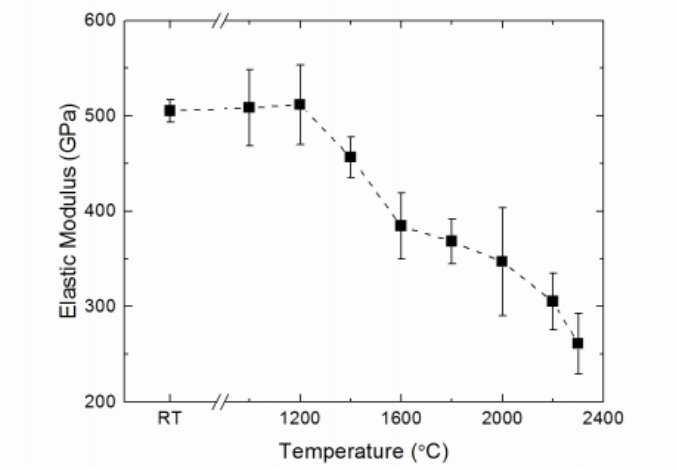

Figure 4-9 Elastic modulus of ZZC10 tested in argon atmosphere as a function of temperature[30].

In addition, from the analysis of SEM and EDS, significant amounts of oxygen are found on some of the ZrC grains, which suggests that the ZrC is acting as a sink for oxygen, that reduces the amount of oxide phase present in the microstructure. The diffusional creep and grain boundary sliding are two contemplating factors which leads to the rapid decrease in modulus at elevated temperature. ZrB_2 and ZrB_2-10 vol% ZrC exhibit the following properties, where E is the Young's modulus, K_{IC} is the stress intensity factor, HV is hardness and σ is flexure strength.

Table 4-3 Mechanical properties of ZrB_2

	E (GPa)	HV (GPa)	K_{IC} (MPa•m1/2)	σ (MPa)
ZrB_2 []	542 ± 8	14.6 ± 0.7	3.82 ± 0.43	508 ± 59
ZrB_2-10 vol% ZrC []	505 ± 12	-	4.8 ± 0.5	696 ± 82

Since the results from the experiments and simulations suggest the failure deformation of ZrB_2–ZrC nanocomposites are derived by grain boundary sliding, void creation and diffusional creep at the grain boundary and grain boundary domain influences overall properties of the material, therefore, it is critical to understand the mechanical behavior of the grain boundary materials.

Chapter 5

Mechanical Properties of Grain Boundary Materials

5.1 Building the Model for Mechanical Test on Grain Boundary

In this chapter the grain boundary properties of ZrB_2 microstructure have been evaluated. First, we have developed sub-models by using grain boundary microstructures. This was done by taking a segment from the polycrystalline ZrB_2 model. The steps involved in developing the simulation box are illustrated in Fig.5-1. The simulation box contains 6,704 atoms in total and has the dimension of $8.52 \times 2.17 \times 4.5$ nm^3.

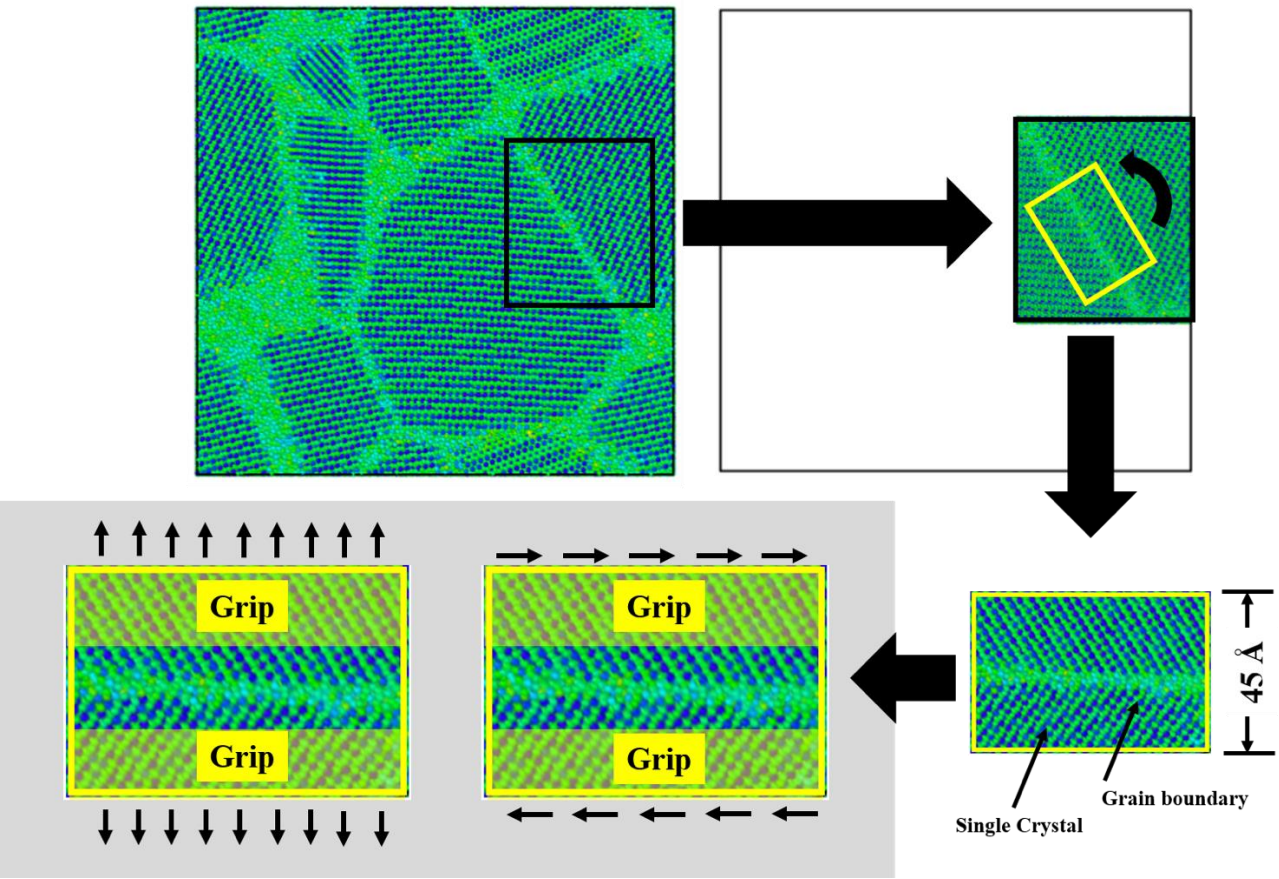

Figure 5-1 Steps needed to create simulation models for evaluating tensile and shear properties of the grain-boundary of polycrystalline ZrB2. First, a sub-model containing the grain boundary is isolated from the ZrB2 polycrystalline model. The sub-model is then rotated to align the grain boundary plan normal to the tensile loading and parallel to shear loading directions. The grain-boundary material in the sub-model is sandwiched between twinned crystals. A selected group of atoms in the twinned zone is set as "fixed." The "fixed" zone is equivalent to a "gripped" zone in conventional test frames. Tensile and shear displacements are applied to the gripped zone and the corresponding deformation in the remaining zones are recorded.

To perform mechanical tests, we fixed the top and bottom portion of the material (i.e., grip zone) and applied the tensile/shear load to that portion. It is apparent from Fig. 5-1 that the "deformable" zone in our model contains both grain boundary materials and crystalline structure. As such, total deformation in the material comes from the grain boundary deformation and deformation of the remaining crystalline structure. To obtain a better understanding of the evaluated properties, we conducted three independent simulations where the height of the "gripped zone" was chosen as 2.5, 5 and 7.5 Å, as shown in Fig. 5-2. We then applied the tensile and shear loading at the "gripped zone."

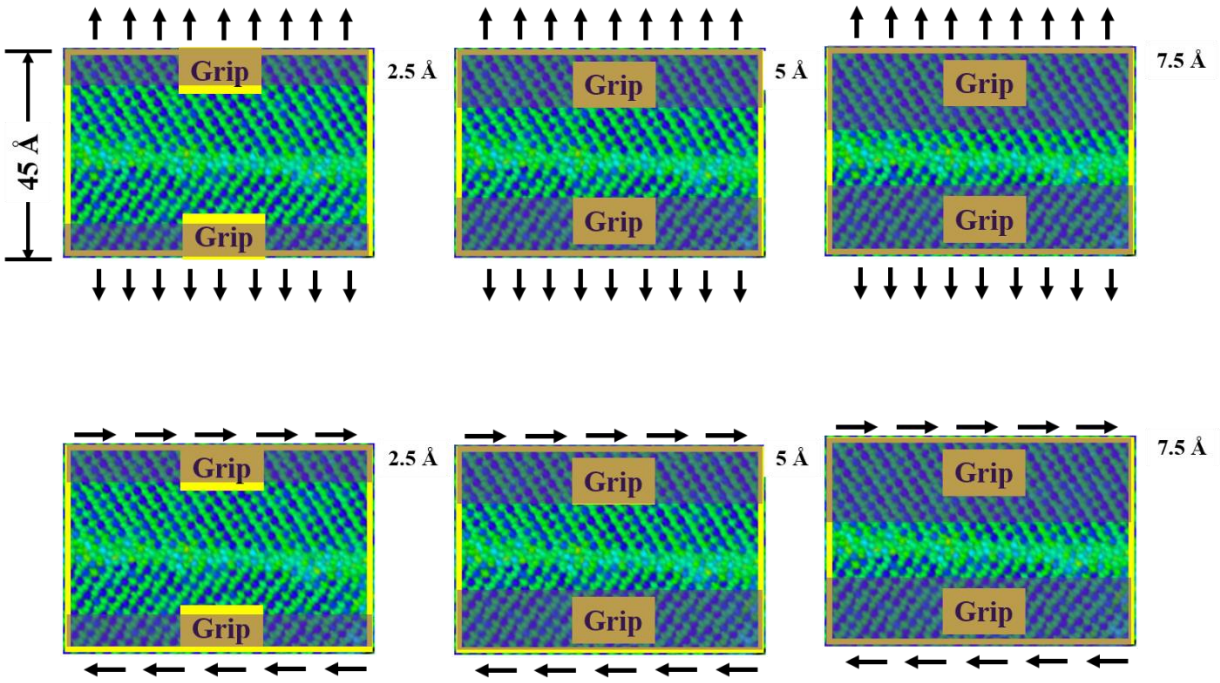

Figure 5-2:MD models for tensile and shear tests for evaluating grain boundary properties of polycrystalline ZrB2. 3 sets of models are created. Total height of the simulation box is 45 Å. In simulation set 1 (left figures), atoms located within 2.5 Å from the top and bottom boundary are defined as "rigid"/"gripped" atoms. Tensile and shear loads are applied to the "gripped" atoms as shown. In simulation set 2 (center figures) and 3 (right figures), atoms located within 5 Å and 7.5 Å from the top and bottom boundary are defined as "rigid"/"gripped" atoms.

5.2 Tensile and Shear Test on Grain Boundary

We then applied the tensile and shear loading at the "gripped zone." The corresponding tensile and shear stress-strain diagram are shown in Figures 5-3 and 5-4, respectively. The local stress plots at different strain states are shown in Figures 5-5 and 5-6. We also ran independent tensile and shear simulations on a model

containing only the twin crystal. Figure 5-7 shows the tensile and shear response of the twin crystal. The stiffness and strength of the sub-model and the twin-crystal are reported in Table 5-1 and 5-2, respectively. These values are utilized in the theory of laminated composites[78] to estimate the grain boundary stiffness properties. Figure 5-8 outlines the schematic of the analytical model.

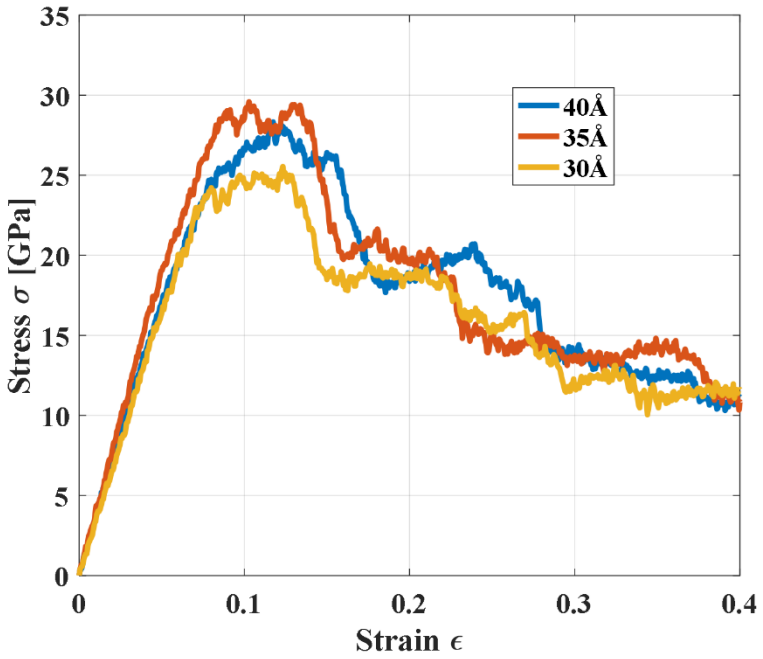

Figure 5-3 Tensile response of sub-model (containing grain boundary layer and twin crystal) of polycrystalline ZrB_2

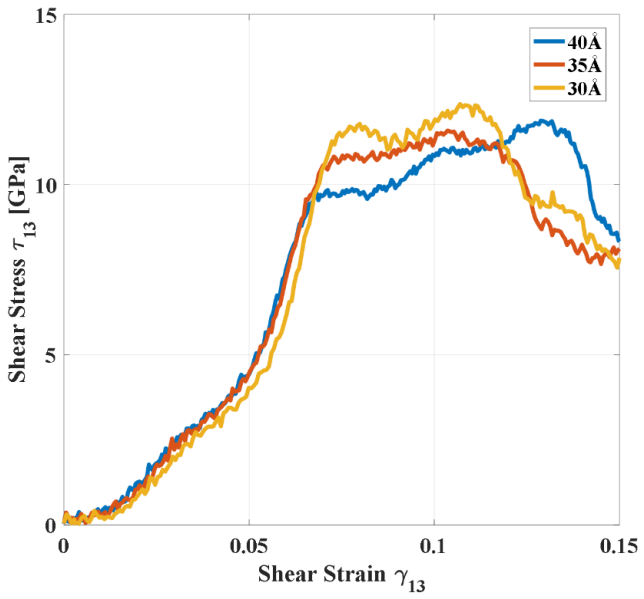

Figure 5-4 Shear response of sub-model (containing grain boundary layer and twin crystal) of polycrystalline ZrB_2

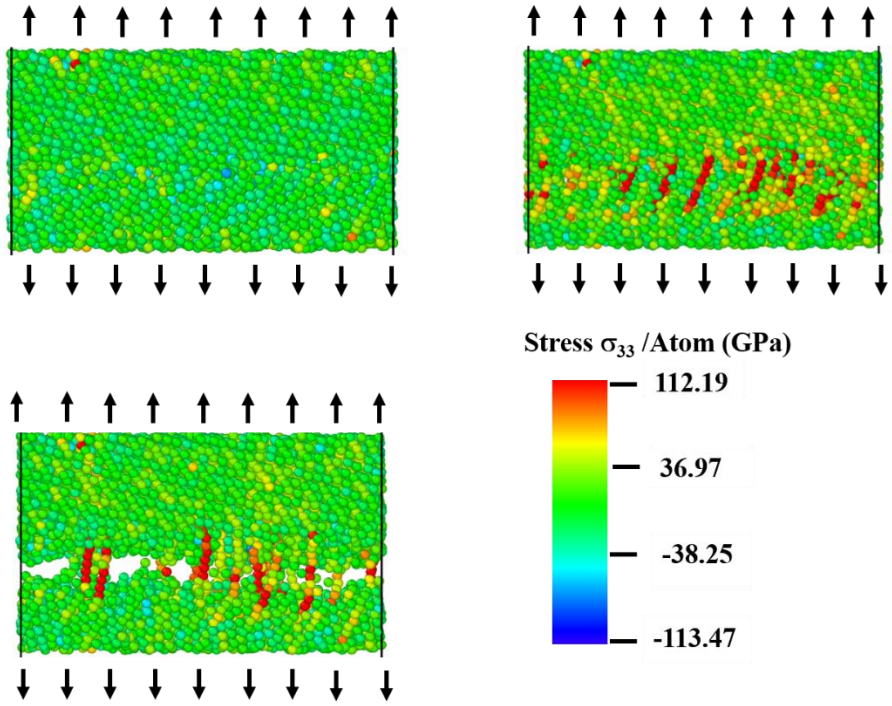

Figure 5-3 Local stress (Stress/Atom) plot of the model (taken from set 1) during tensile loading with strain level = 0, 13.4 and 16.7%. Local stress is much higher at the grain boundary compared to other

atoms. The atoms are colored according to the stress tensor (σ33). Note that the local direction "3" is different from the global direction "z"

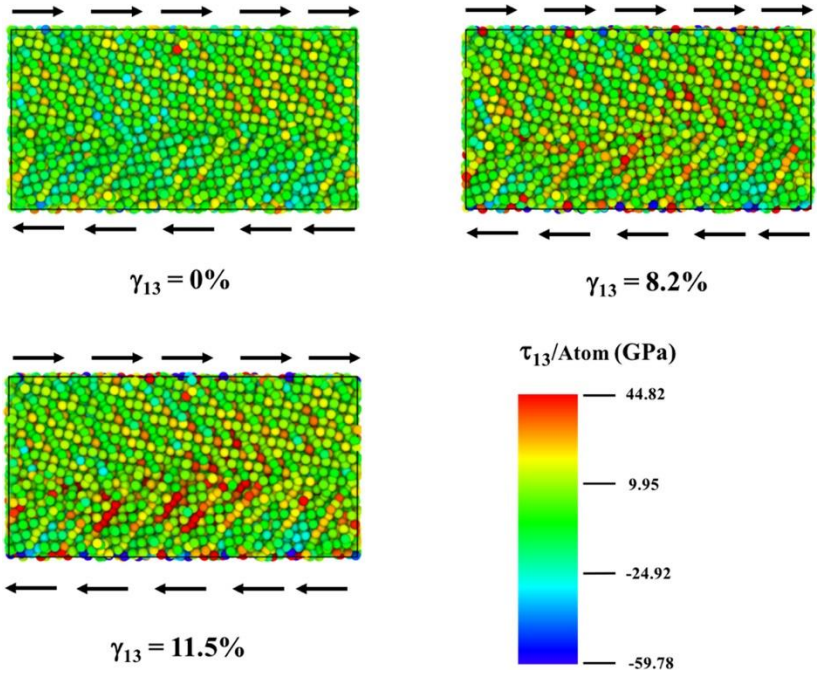

Figure 5-4 Local stress (Stress/Atom) plot of the model (taken from set 1) during shear loading with strain level = 0, 8.2 and 11.5%, respectively. The atoms are colored according to the stress tensor (τ_{13}). Note that the local direction "3" is different from the global direction "z".

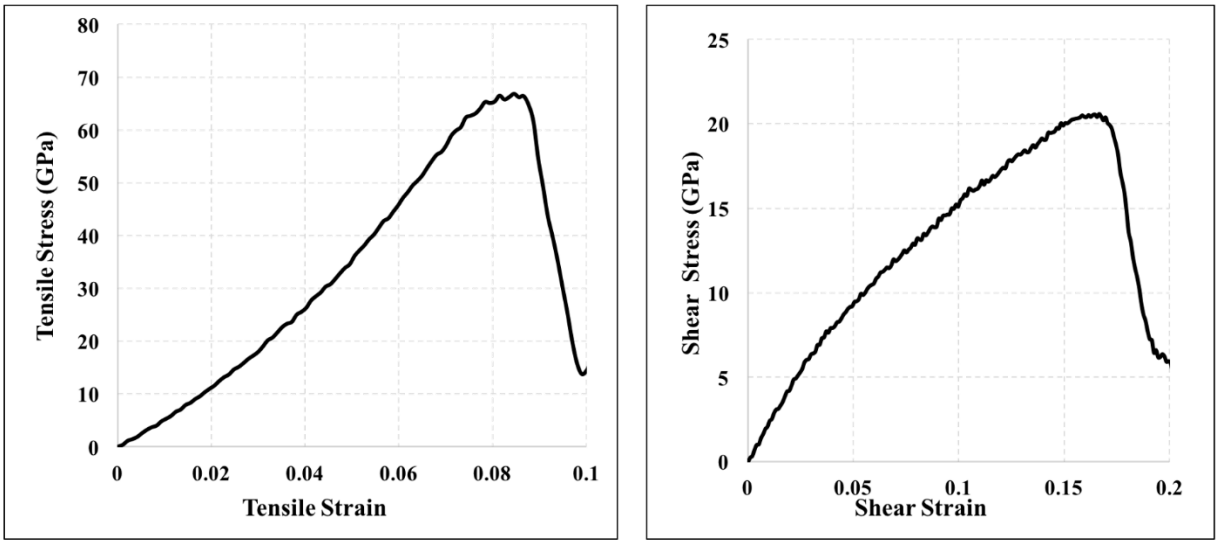

Figure 5-5 (a) Tensile and (b) shear response for the crystal structures adjacent to the grain boundary materials. Elastic properties extracted from these stress-strain relations are used in Eqs. 10 and 11

We also ran independent tensile and shear simulations on a model containing only the twin crystal. Figure 5-7 shows the tensile and shear response of the twin crystal. The stiffness and strength of the sub-model and the twin-crystal are reported in Table 5-1 and 5-2, respectively.

Table 5-1 Mechanical properties of Sub-Model

Sub-model type Ltotal (Å)	Elastic Constant, C11 (GPa)	Elastic Constant, C13 (GPa)	Young's modulus E (GPa)	Shear Modulus G = C44 (GPa)	Poisson's Ratio v	Tensile strength (GPa)	Shear strength (GPa)
40	366.89	201.1	224.49	114.25	0.35	28.32	12.25
35	386.69	212.84	235.57	116.13	0.35	29.58	11.82
30	328.67	180.36	200.86	112.59	0.35	25.54	13.40

Table 5-2 Mechanical properties of twin crystal of ZrB2 adjacent to grain boundary.

	Elastic Constant C11 (GPa)	Elastic Constant C13 (GPa)	Elastic Constant C44 (GPa)	Young's modulus E (GPa)	Poisson's Ratio v	Shear Modulus G (GPa)	Tensile strength (GPa)	Shear strength (GPa)
Twin crystal of ZrB2	521.08	214.04	218	396.43	0.29	218	66.91	20.51

These values are utilized in the theory of laminated composites [50] to estimate the grain boundary stiffness properties. Figure 5-8 outlines the schematic of the analytical model.

5.3 Stiffness of Grain Boundary with Analytical Model

Based on the illustration in Fig 5-8, it can be argued that the loaded sub-model is a laminated structure where grain-boundary material is sandwiched between twinned crystals. Since the orientation of the crystal above and below the grain boundary material is nearly mirrored with respect to the horizontal plane, it is

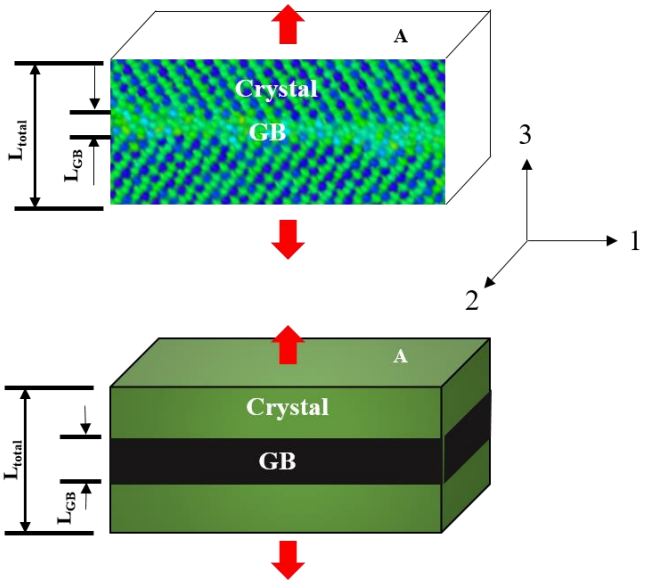

Figure 5-6 Schematic diagram showing how representative volume element for the analytical model is defined in relation to the sub-model.

reasonable to assume that the stiffness and strength of the crystal along the loading direction (i.e '3') can be assumed as the same. It can be observed that

$$L_{total} = L_{GB} + L_{crystal} \tag{1}$$

where L is the height of the sub-model = 40 Å, 35 Å and 30 Å in simulation Sets 1, 2 and 3 respectively. LGB is the height of the grain-boundary material, Lcrystal is the height of the crystal. From the MD snapshot of the sub-model, the average height of the grain boundary has been estimated as 5 Å, and it remains constant for all different sub-models.

Under uniform tensile displacement δ_{total}, the following relation is valid

$$\delta_{total} = \delta_{GB} + \delta_{crystal} \tag{5.1}$$

where δ_{GB} and $\delta_{crystal}$ are displacements in the grain boundary and in the crystal, respectively.

Assuming the cross-section area A is same for the crystal and the grain boundary layer, the force equilibrium along the "3" direction gives

$$F_{total} = F_{GB} = F_{crystal} = F = \sigma_{33}A \tag{5.2}$$

where F_{total}, F_{GB} and $F_{crystal}$ represents a corresponding internal result force in the sub-model, in the grain boundary and in the crystal layer, respectively. Thus, internal forces are the same in each layer. Since the area A is the same in each layer, the internal stress σ33will be the same in each layer as well.

Applying axial force-displacement relation $\delta = \frac{FL}{EA} = \frac{\sigma L}{E}$ for each layer, gives

$$\delta_{GB} = \frac{FL_{GB}}{E_{GB}A} = \frac{\sigma L_{GB}}{E_{GB}} \tag{5.3}$$

$$\delta_{Crystal} = \frac{\sigma L_{Crystal}}{E_{Crystal}} \tag{5.4}$$

where E_{GB} and $E_{crystal}$ are the stiffness of the grain boundary and the crystal, respectively.

Now, dividing Eqn. (2) with L and rearranging gives

$$\frac{\delta_{total}}{L} = \frac{\delta_{GB}}{L_{GB}}\frac{L_{GB}}{L} + \frac{\delta_{crystal}}{L_{Crystal}}\frac{L_{Crystal}}{L} \tag{5.5}$$

or,

$$\varepsilon_{total} = \varepsilon_{GB}\frac{L_{GB}}{L} + \varepsilon_{crystal}\frac{L_{Crystal}}{L} \tag{5.6}$$

where ε_{total}, ε_{GB} and $\varepsilon_{crystal}$ represent the state of strains in the sub-model, in the grain boundary and in the crystal, respectively. Also,

$$\varepsilon_{GB} = \frac{\sigma}{E_{GB}} \tag{5.7}$$

$$\varepsilon_{Crystal} = \frac{\sigma}{E_{Crystal}} \tag{5.8}$$

and combining Eqns. 6 and 7 can be expressed as

$$\varepsilon_{total} = \sigma\left(\frac{1}{E_{GB}}\frac{L_{GB}}{L} + \frac{1}{E_{Crystal}}\frac{L_{Crystal}}{L}\right) \tag{5.9}$$

Or

$$\frac{1}{E_{total}} = \left(\frac{1}{E_{GB}}\frac{L_{GB}}{L} + \frac{1}{E_{Crystal}}\frac{L_{Crystal}}{L}\right) \tag{5.10}$$

Rearranging results in

$$E_{GB} = \frac{L_{GB}}{\frac{L}{E_{total}} - \frac{L_{Crystal}}{E_{Crystal}}} \tag{5.11}$$

Using similar analysis, the shear modulus for the grain boundary can also be derived as

$$G_{GB} = \frac{L_{GB}}{\frac{L}{G_{total}} - \frac{L_{Crystal}}{G_{Crystal}}} \tag{5.12}$$

Table 5-3 lists the estimated grain boundary properties using the adjacent twin and the sub-model properties shown in Tables 5-1 and 5-2.

Table 5-3 Estimated mechanical properties of GB.

Sub-model type L_{total} (Å)	**Young's modulus (GPa)**	**Shear Modulus (GPa)**
40	97.26	26.27
35	116.54	30.46
30	100.50	32.64

Comparing the strength and stiffness of the twin crystal and the stiffness of the sub-model, the strength of the grain boundary material can be assumed the same as the strength of the sub-model. Based on this assumption, we can estimate that the tensile and shear strengths of the grain boundary are about 26–28 GPa and 12 GPa, respectively. Comparing these strength values with Fig. 4-3, it can be argued that the overall material strength is influenced by the shear failure of the grain boundary materials. The grain boundary material property reported here is specific to the grain boundary material selected from the specific location of ZrB_2. Additional studies are underway to obtain statistical distribution of grain boundary properties where grain boundary segments are chosen from multiple locations and averaged. The effect of temperature on the grain boundary properties are also studied. The results from this study will be reported in the future.

5.4 Conclusions

In this study, we have investigated the deformation and failure behavior of polycrystalline ZrB_2 and ZrC-ZrB_2 nanocomposites. The size of NP varied between 6, 7 and 8 nm. The location of NP within ZrB_2 varied when the ZrC NP was placed at the grain boundary junctions (Model I), on the grain boundary (Model II) and in the grain interior (Model III). Another model is built where ZrC NP is replaced by 6 nm in diameter void. Nevertheless, it has been observed that the failure of all materials occurs at the grain boundary via grain boundary sliding and void creation. Because the grain boundary has a significant effect on the failure behavior, the properties of the grain boundary were also evaluated. Simulation results indicate that the tensile strengths of ZrB_2 and ZrC-ZrB_2 nanocomposites are ~22.85 GPa, whereas the strength of the grain boundary is about 26–28 GPa. The shear strength of the grain boundary is 12 GPa. As such, the grain boundary is much weaker in shear which drives the overall failure via grain boundary sliding.

Chapter 6

Nanofilms of HfO_2

6.1 Introduction

Hafnium oxide is the inorganic compound with the formula HfO_2, also known as hafnia, this colorless solid is one of the most common and stable compounds of hafnium. It is an electrical insulator with a band gap of 5.3~5.7 eV. Hafnium dioxide is also called UHTC material because the meting point of this material is above 2700° C.

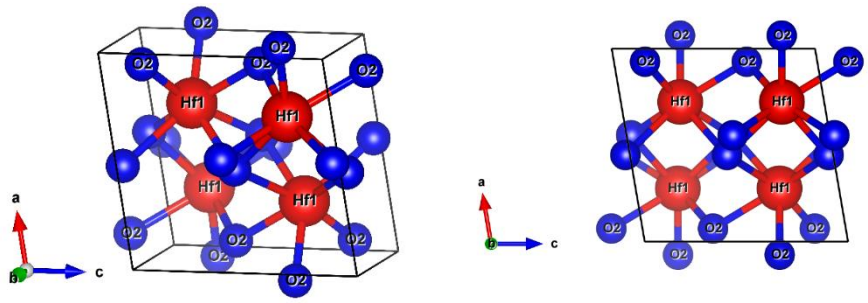

Figure 6-1 Crystal structure of monoclinic HfO_2

Hafnia crystallizes into three crystalline polymorphs at ambient pressure: a monoclinic P21/c phase, a tetragonal P42nmc phase, and a cubic fluorite $Fm^{-}3m$ phase. The monoclinic-to-tetragonal transition takes place at 2000 K while the tetragonal-to-cubic transition occurs at 2900 K. The melting point of the cubic phase is at 3085 K. There are also two high-pressure phases: the orthorhombic I phase Pbca, Brookite-type structure above 10 GPa and the orthorhombic II phase Pnma, PbCl2-type, or cotunnite structure above 30 GPa.13 Monoclinic hafnia has a band gap of 5.68 eV.

6.2 Motivation and Potential Application

Bio-inspired neuromorphic platforms have been attracting considerable attention as new type of computing systems, because of their high efficiency, low power consumption, adaptive learning algorithm and parallel

signal processing [1–4] Standard computation systems today are based on Von Neumann architecture where the processor and memory are separate, and data moves between them [99]. This separation produces a temporal and energetic bottleneck because information has to be shuttled repeatedly between the different parts of the system[6–8]. The neuromorphic computation completely changes that model by having memory and processor at one chip where information can be stored and computed from the same place. In neuromorphic architecture the device that mimics the synapses (a junction between two nerve cells) is called memristor, which is a two terminal device able to change their conductance from a high conductance state (HCS) to a low conductance state (LCS), under proper electrical stimuli [2, 9-10]. Memristor is a fourth passive circuit element originally postulated by Leon Chua in 1971[14], and the physical model was presented by Williams et al. at 2008[105].

A typical memristor device is a sandwich-like a nanostructure [2, 12-14] where the memristor material, mostly the oxides of Hf, Zr, Ti etc, is trapped between the electrode layers. Of these systems, HfO2-based memristor devices appear to become most popular. Nevertheless, the operation of such device requires substantial variation electric field intensity. For a resistive memristor device, the process also involves defect formation, collapse and migration inside the oxide layer. In addition, heat flux generated by power semiconductor devices is increasing every day. In some motor drive applications, the heat flux can be higher than 100 W/cm2 in the steady state, and the peak heat flux can be as high as 300 W/cm^2 under transient conditions[14–16]. Likewise, during the operation process of memristor, for the formation state where conduction filament is created, requires temperatures over 350°C [109]. In addition, study regarding the local thermal effects during switching in memristor provides strong evidence for local heating [110]. As the thermal expansion coefficient is different for different materials, with the application of heat flux this material experiences mechanical stress. Moreover, HfO_2 is a ferroelectric material, and all ferroelectric materials are generally pyroelectric and piezoelectric, but not vice versa [111]. Therefore, this material produces stress/strain when an electric field is applied. In other words, the cyclic nature of thermal and

electrical loading along with the defect dynamics and residual stress generation, the structural reliability, in terms of static and fatigue failures, of such devices needs to be clearly understood.

Garbin, et al. [112] and Covi et al [113] separately investigated the fatigue life of HfO_2 under various electrical loads. It has been observed that for a rectangular pulse with 1 V amplitude and 100 ns duration, the endurance limit of HfO2 is over 105 cycles [12]. It is also observed that the resistance of the device locks at high-resistance state when failure becomes imminent. If longer pulse duration (e.g. 1 μs) is used, then the failure does not occur even after 100 million cycles. Covi et al [113] have observed that for a given pulse amplitude, when longer time widths is applied, the conductance decreases rapidly and settles at a lower saturation value, with respect to shorter amplitude–width cases. Matveyev et al.[14] studied the fatigue life of a 3-nm-thick HfO2 film grown on a 40 × 40 nm2 surface and determined that the device endures over 105 switching cycles. Electric field-induced oxygen vacancy reservoir depletion [2] and damage of the electrode material [14] are suspected to be the two contemplating factors on the device failure. However, a fundamental understanding on the effect of electric field on the failure of memristor material is not clearly known primarily because it is difficult to capture the dynamic behavior of the material at the atomistic/nano level during experimentation.

At present, we have a limited understanding of how operating frequency and operating temperature affect the processes that govern the switching of nanoscale cells in nanosecond timescales. Microscopy and detailed electrochemical studies lack the spatial and temporal resolution needed to explore this regime. As such, atomistic simulations [25–31] can help fill this knowledge gap to understand the structural deformation and possible reasons for the memristor failure for various electric loading conditions. It is critical to gain fundamental understanding on the effect of electric field and temperature on the failure of memristor material. In this paper, the effects of electric field and temperature on the mechanical properties of HfO2 memristor material have been reported. We have chosen HfO_2 because it is one of the promising memristor materials recently manufactured and studied extensively [1–6]. We have studied how the electric field affects the crystal structure and structural damage of the memristor material.

6.3 Simulation Model

Molecular Dynamics simulations were carried out to investigate the mechanical behavior of HfO_2 thin films under different electrical loadings. All simulations were done in openly available MD simulation package LAMMPS[91]. The atomistic structures were visualized using OVITO software (a scientific visualization and analysis software for atomistic and particle simulation data)[64].

As shown in Fig. 6-2(a), the crystal structure of HfO_2 is built on a monoclinic lattice with nominal lattice constants a =5.12 Å , b = 5.17 Å, c =5.29 Å and angles $\alpha = \gamma = 90°$, $\beta = 99°$ [99]. An atomistic model (Fig. 1b) with a simulation box size of $16 \times 16 \times 5$ nm^3 containing a total of 108,000 atoms is developed in this study. To represent the material as a bulk nanoscale film, periodic boundary conditions are applied in x and y direction (normal to the thickness direction) and the thickness direction are kept as non-periodic. The thickness is kept as 5 nm because the typical thickness of memristor material is about 5 nm [121]. The interactions between Hf-Hf, O-O and Hf-O have been described by the charge optimized many body potential developed by Shan et al[38].

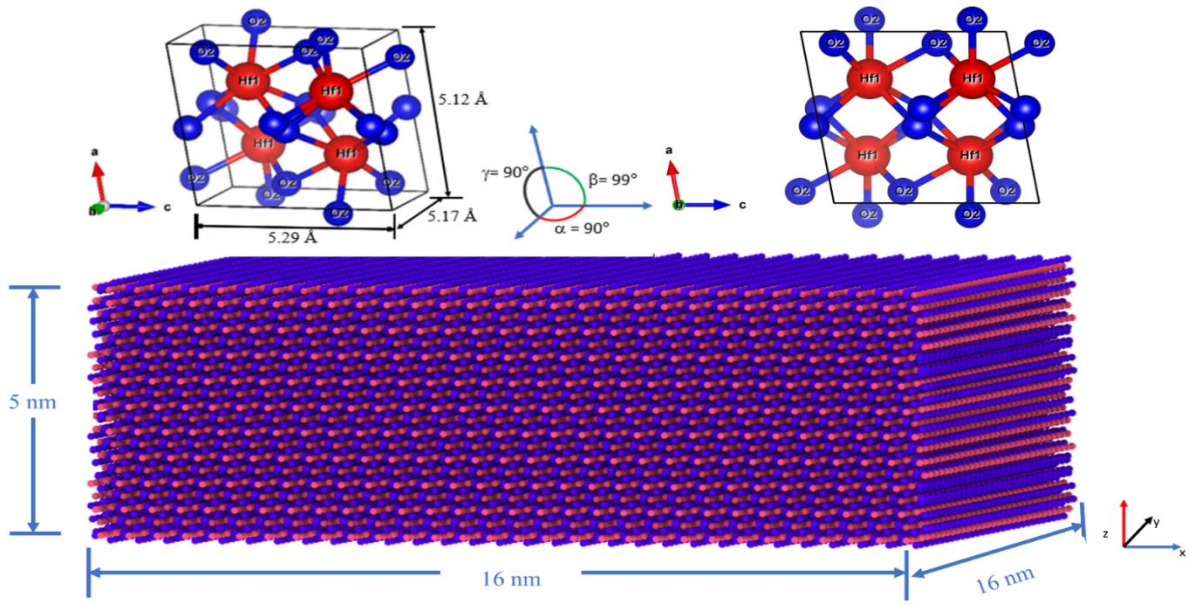

Figure 6-2 (a) Crystal structure of HfO_2. Here, the blue atoms represent Hf, and red atoms represent O (b) atomistic model of HfO_2.

The environmental temperature is maintained at 300 K using the Nosé-Hoover thermostat. To develop stress strain curves, initial atomistic models were equilibrated first to attain a stress-free state. During equilibration, each simulation was run up to 150,000 timesteps in a constant temperature/constant pressure (NPT) ensemble. After attaining the stress-free state, a displacement rate of 2.5 Å/ps is applied at the top and bottom fixed regions to obtain the tensile stress strain curve. The constant temperature/constant volume (NVT) ensemble was used during this step. In the remainder of this paper, this model is referred as "Without Efield Model". In parallel, the equilibrated model was separately subjected to different electric fields of intensities equal to 0.2 v/Å, 0.25 v/Å and .3 v/Å and was reequilibrated. Two types of simulations were conducted on each of this model. In the type 1 case, the electric field was kept "on" and tensile loading was applied in a similar manner described earlier. This is model is referred as the "With Efield model". In the type 2 case, tensile loading was applied with the electric field turned "off". This model is referred as the "Deformed model". For clarity, a flowchart is shown in Fig. 6-2 (b) outlining the steps involved during the

simulation. To capture the effect of temperature on these models, subsequent simulations were conducted at different temperatures, namely, at 350 K, 400 K and 450 K. Because of the applied electric field, these models experienced crystal deformation. As Figure 6-13(b) shows the crystal deformation of the model after applying 0.3 v/Å for 30 Ps. To study the effect of electric fields on those deformed models, tensile and shear tests were carried out from 0 to 0.3 v/Å electric loading conditions. The "deformed model" of figure 5 and 6, signifies 0 v/Å electric loading condition while carrying out the tensile test.

It should be noted that the electrode attached to the top of the memristor made of metal like Pt, Ti, Cu [24–26] has symmetric crystal structure and does not show any piezoelectric behavior. Therefore, the mechanical behavior for both tensile and shear will be different for different electric field conditions. To evaluate the mechanical response of memristor material HfO_2, we started with tensile test of HfO_2 at room temperature. As the crystal structure of the material is non symmetric the tensile tests were carried out in all different directions.

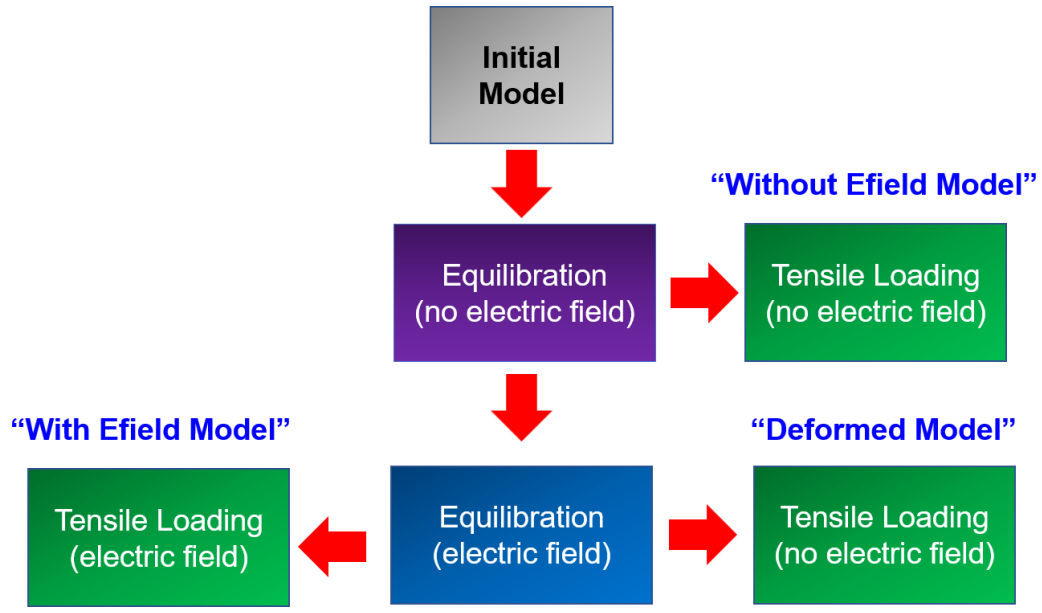

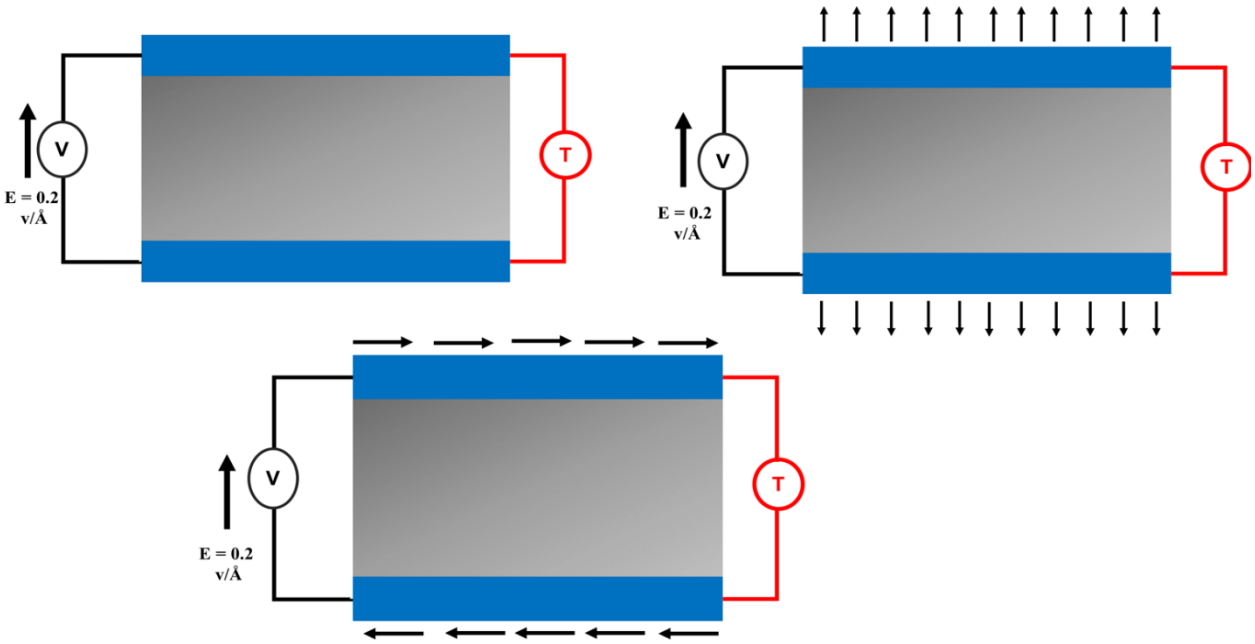

Figure 6-3 (a) Flowchart describing how different electric field conditions were imposed on a model during tensile test. The box in green indicates the final model simulated. The labels in blue refer to the model name that are used in this paper. (b) Schematics showing the mechanical loading scheme on the HfO2 thin film in presence of temperature and electric fields.

6.4 Results and Discussion

6.4.1 Mechanical properties of HfO_2

The tensile stress-strain response of HfO_2 due to displacement field applied along the z-direction is shown in Fig. 6-4. Due to displacement restriction, tensile stresses are developed along the x and y direction, as shown in Fig. 6-4. It can be observed from Fig. 6-4 that the stress strain curve is almost identical in the y and z direction whereas the material response is different in the x direction. The elastic constants of HfO_2 in x, y and z directions are 447.9 GPa, 543.76 GPa, 497.37 GPa, respectively. From the simulation, the tensile strength in the x direction is 33.77 GPa whereas the tensile strength of y and z directions are 43.64 and 42.16 GPa respectively. It is evident from Fig. 6-4 that the materials deform linearly up until about 0.02 strain (inset of the Fig. 3) and then they deform somewhat in a nonlinear manner until failure commences at about 0.12, 0.14 and 0.13 strain in the x , y and z direction, respectively. The MD snapshots during failure are captured and presented in Fig. 6-5. It can be observed that the failure occurred due to

crack formation along the inclined plane, which is the weakest crystal plane in the HfO_2 system. The mechanical behavior of HfO_2 depends on the crystal structure of the nanofilm which is further controlled by the nano film deposition method, deposition temperature and post annealing processes[125]. On the other hand, the mechanical properties of bulk HfO_2 depends on the microstructure of the specimen which is controlled by the fabrication process and sintering techniques[126]. Based on the specimen dimension and experimental procedures a wide range of elastic and shear modulus is reported in the literature. Furthermore, researcher also investigated the mechanical properties based on first principle calculation by using density functional theory. A comprehensive comparison of mechanical properties of HfO_2 by different analysis techniques is added in Table 6-1.

Table 6-1 Comparison of the mechanical properties of HfO2

	Crystal Structure	**C_{11} (GPa)**	**C_{22} (GPa)**	**C_{33} (GPa)**	**Young Modulus E (GPa)**	**Shear Modulus G_{13} (GPa)**	**Analysis Method**	**Ref**
1.	Monoclinic	297	396	340	316.79	130.73		[127]
2.	Tetragonal	495		397			DFT	[38]
3.	Cubic	578					DFT	[38]
4.	Polycrystal (Nano film)				380		AFM	[125]
5.	Monoclinic (Bulk material)				285	109.2	Sonic Resonance technique	[126]
6.	Monoclinic (Nano film)	447.9	543.76	497.37	345.62	179.67	MD	Current Work

From the data stated in the table 6-1, the value of the elastic constant C_{11} is varies from 297 GPa and 578 GPa based on the crystal structure. In this work, for the monoclinic HfO_2 the value for elastic constant is found as 447.9 GPa. The elastic modulus for the polycrystal HfO_2 nano film and monoclinic bulk specimen

are reported as 380 GPa and 285 GPa whereas from our simulations the elastic modulus is found as 345.62 GPa. Therefore, the mechanical properties we found from this work is quite comparable with the existing literature.

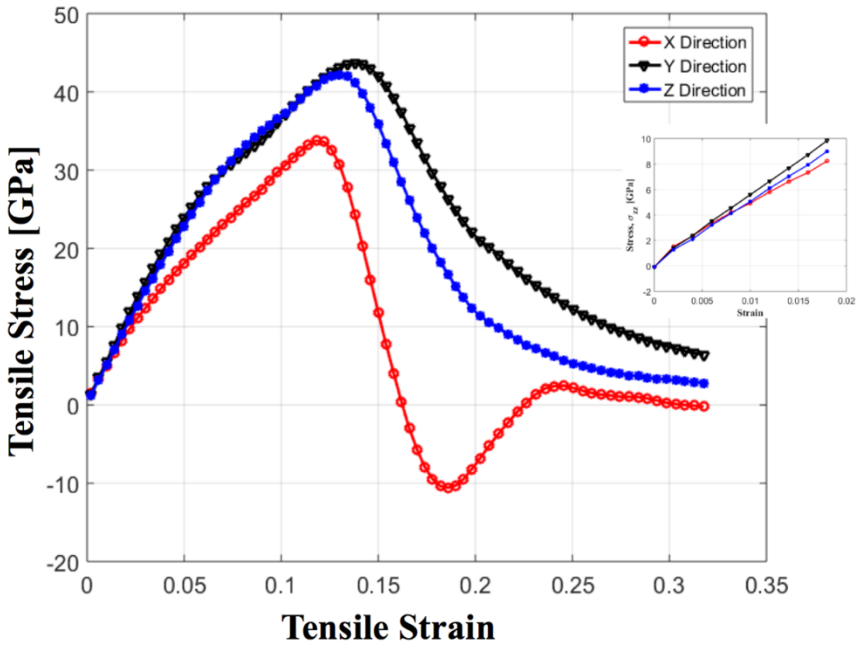

Figure 6-4 Stress-strain curves for tensile test of HfO2 at 300K. Inset plot shows initial part of stress-strain relation.

The MD snapshots during failure are captured and presented in Fig. 6-5. It can be observed that the failure occurred due to crack formation along the inclined plane, which is the weakest crystal plane in the HfO_2 system.

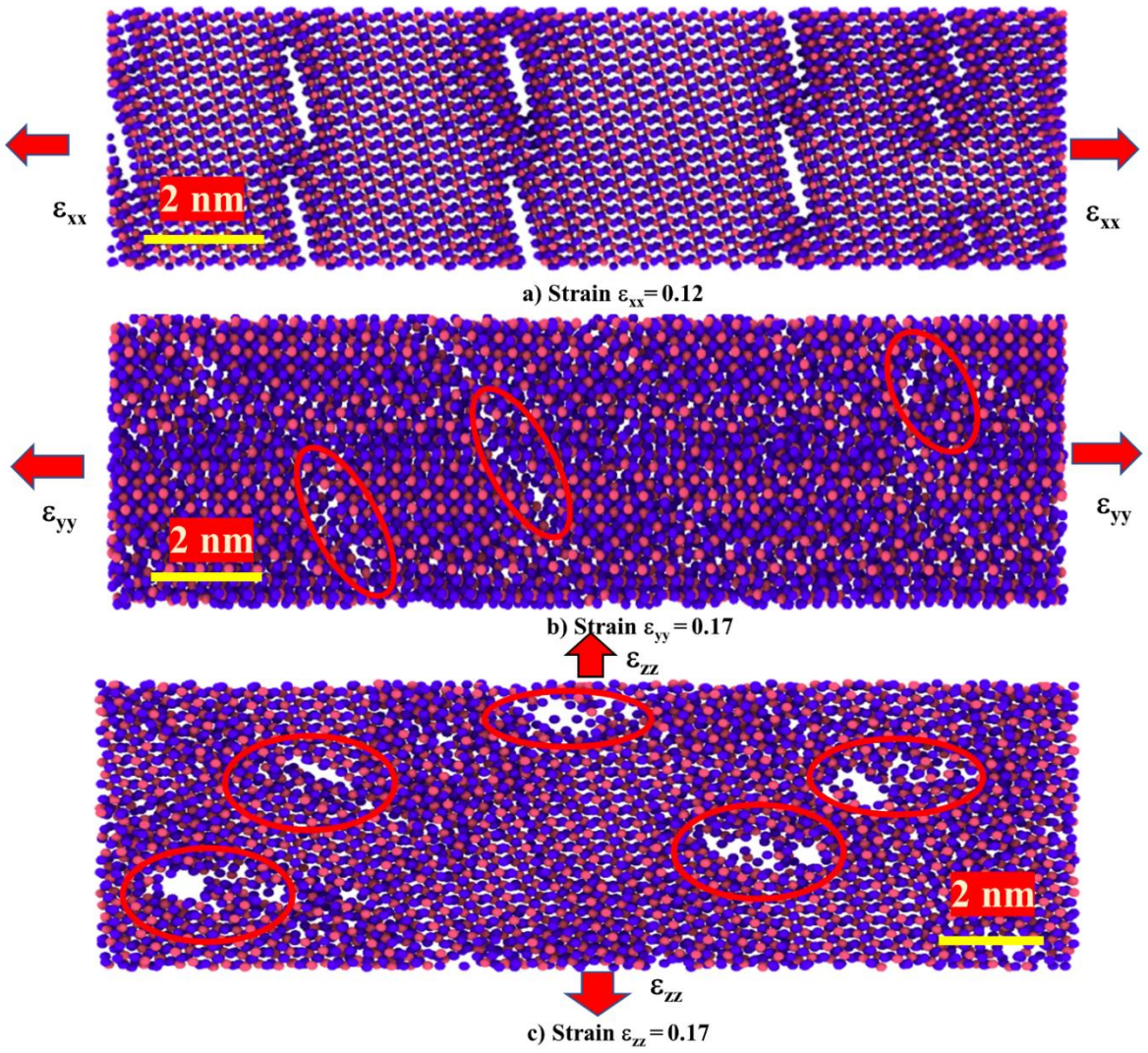

Figure 6-5 Atomic snapshots of deformed model of HfO2 at different strain states at different directions. Note that the material failed at strain states equal to 0.12, 0.14 and 0.13 in the x, y and z direction, respectively.

6.4.2 Effect of Electric Field on the Mechanical properties of HfO_2

To study the effect of electric load on the material properties, tensile tests were carried out under electric fields ranging from 0 to 0.3 v/Å. Before running the tensile tests, the models are equilibrated with different electric fields. The top and bottom regions are kept fixed during the simulation to mimic the confinement of the HfO_2 nanofilm. The stress strain curve is shown in Fig. 6-6. As the material is kept fixed, the applied electric field induces compressive residual stress on the material. It is estimated that for 0.2 v/Å and 0.3

v/Å electric fields, the developed residual stresses are 1.2 GPa and 2.2 GPa, respectively. This compressive residual stress[128] can negatively affect the diffusion property of memristor material.

It is evident from Fig. 5 that the tensile strength of HfO_2 without electric field is 42.27 GPa. The tensile strength of the HfO_2 along the thickness direction (i.e. σ_{zz}) reduces as the intensity of the electric field increases. The estimated tensile strengths of HfO_2 are 35.43 GPa and 29.40 GPa for 0.2 v/Å and 0.3 v/Å electric field, respectively. The elastic constant of HfO_2 without electric field is 492.04 GPa, while with the electric field of 0.2 v/Å and 0.3 v/Å, the elastic constants reduce to 444.13 GPa or 437.13 GPa respectively. Both elastic constant and tensile strength decrease with the applied electric field.

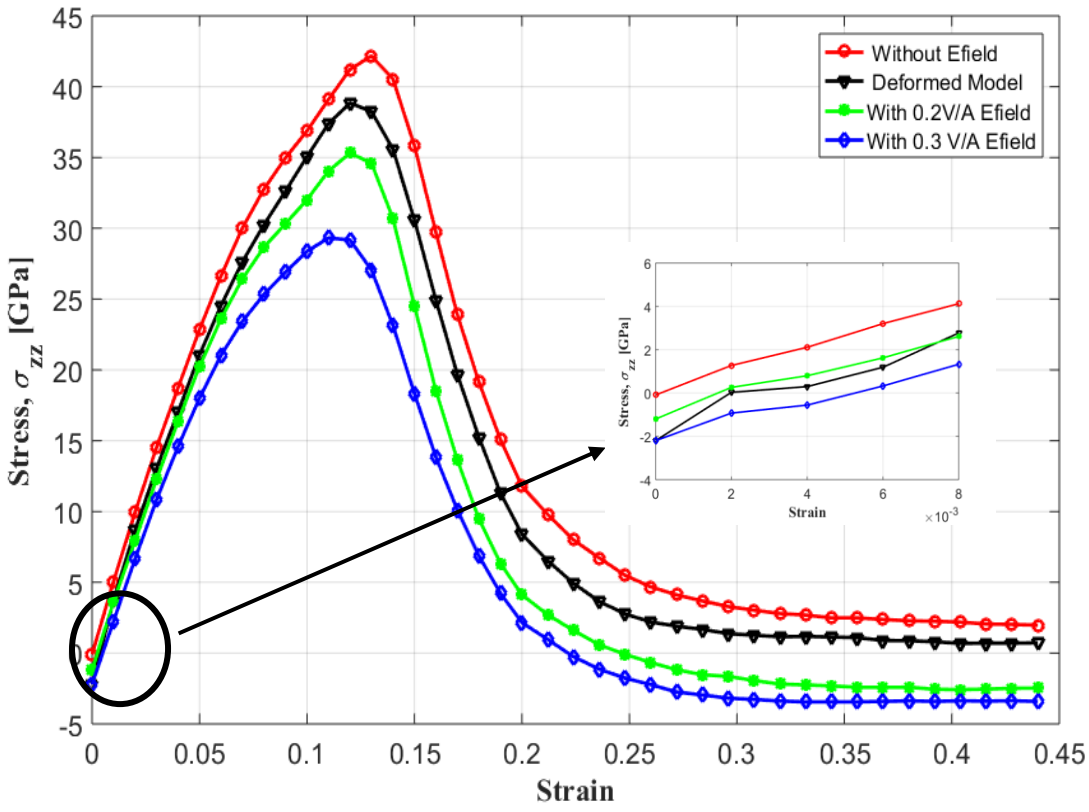

Figure 6-6 Stress-strain curves representing the effects of electric field on the tensile properties of HfO2. Inset plot shows the residual stress developed on HfO2 because of the applied electric field.

6.4.3 Effect of Temperature on the Tensile Properties of HfO_2

Because of the local heat produced during SET and RESET process of the memristor, the temperature may substantially increase in this material. The SET process refers to low resistance state which is considered as ON state in resistive switching device under negative voltages and RESET process refers to the high-resistance state (HRS) which is considered as OFF state of resistive switching device under positive voltages. These processes are reversible and can go through millions of cyclic loads based on their application. These processes create local heat which eventually produce thermal stress on the memristor device. According to the JEDEC standard the recommended value for thermal cyclic load varies from 248 K to 413K for electronic device components [129] .Therefore, the tensile properties are evaluated at different temperatures varying from 300 K to 450 K. From the Fig. 6-7, the materials response at 400 K is almost identical with the response of 300 K. Study by Fang et al [130] showed that HfO_2-based memristor materials exhibit temperature instability. They observed that with the increase of up to 100 ℃ high temperature the leakage current of high-resistance state increases, and the set/reset voltages decreases. The oxygen-vacancy-related trap formation and annihilation are thought to be responsible for all these phenomena. Since our simulation time is extremely short, it was not possible to capture any oxygen-vacancy-related trap formation and annihilation. As such, our tensile simulation at different temperatures did not exhibit any substantial difference in the structural properties of hafnia. In addition, the melting point of HfO_2 is 2973 K [131] which is much higher than the operating temperature of the device. Therefore, in the range of 300 K to 450 K almost identical tensile properties of HfO_2 are found.

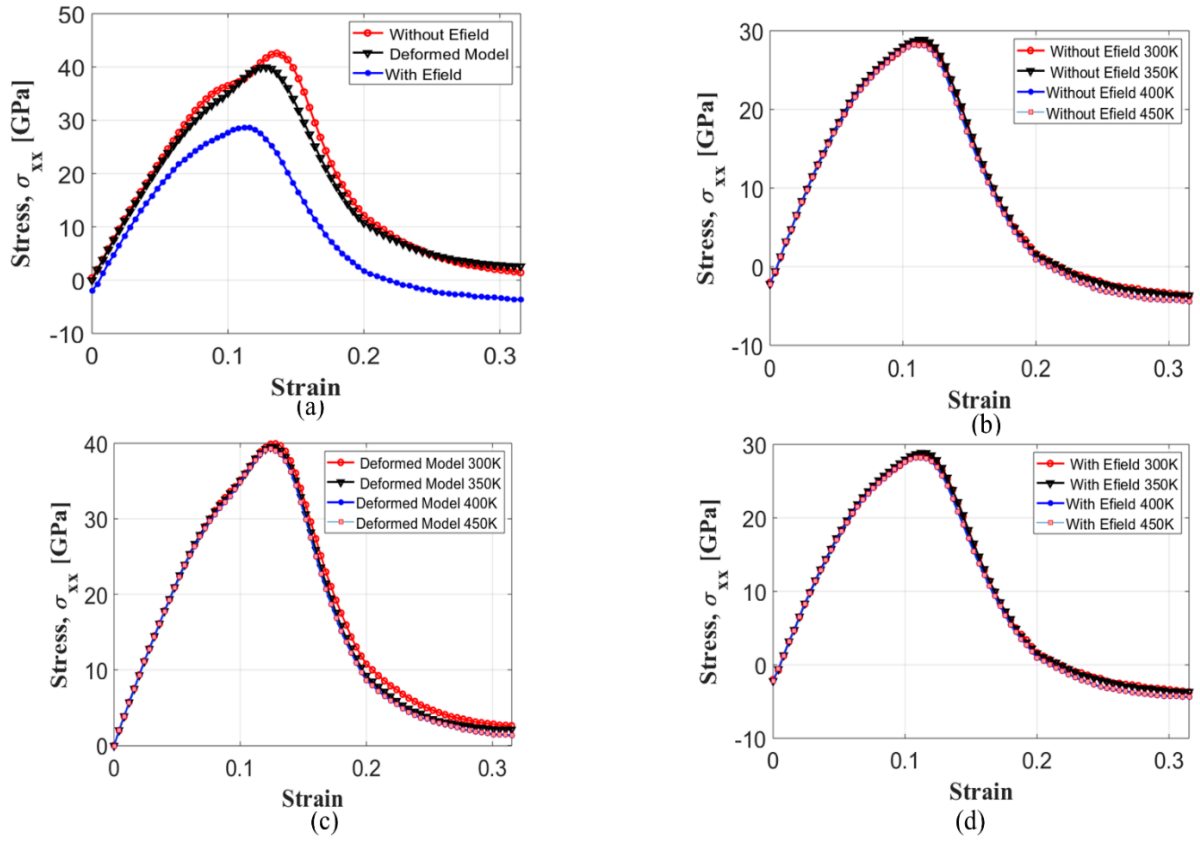

Figure 6-7 a) Stress strain curve for tensile test with different electric field condition at 400 K b) Stress strain curve without electric field at 300 K and 400 K c) Stress strain curve of deformed model electric field at 300 K and 400 K d) Stress strain curve with electric field at 300 K and 400 K.

6.4.4 Shear test of HfO_2 with different electric field

6.4.4.1 Shear test without electric field

The shear stress strain curve is obtained after shear load is applied at the top and bottom surface of the simulation model. As the crystal structure of hafnia is not symmetric, the shear loading is applied in two different manner. In the first set of simulation, the shear loading is applied such that the angle between the vertical axis and the inclined crystal plane increases due to loading. To achieve this, the top surface was moved from right to left and the bottom surface was moved from left to right, as shown in Fig. 6-8. The model deforms almost linearly until shear strain state of 0.09. Then, the curve becomes nonlinear until failure strain of 0.18. From Fig.6-9(a), it is observed that the material goes through some permanent deformation near the strain state of 0.09. The stress response becomes nonlinear after this point.

(c)

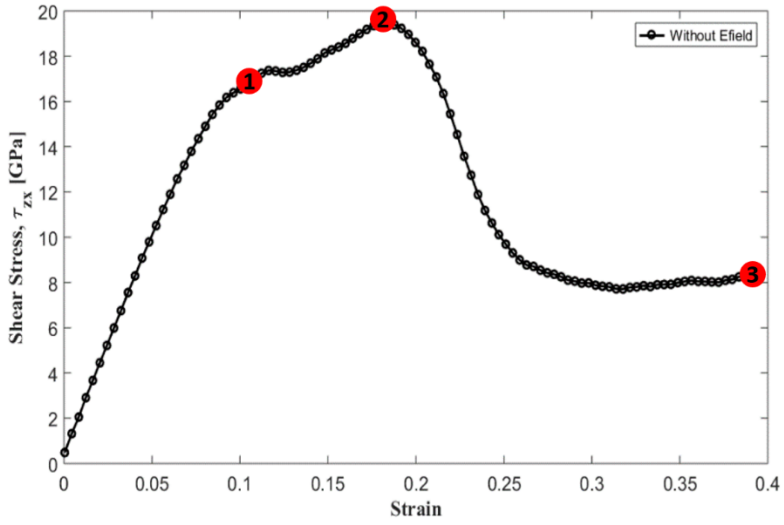

Figure 6-8 Shear stress strain curve of HfO_2 and deformed snapshot of HfO_2 at different strain states.

Between strain states of 0.09 and 0.18, damage accumulates, and voids start to form near the fixed layer. To identify the changes in the crystal structure during every loading step, local atomic densities are plotted. In the atomic density plot, the blue areas represent lowest atomic density region. As such, appearance of blue areas is an indication of void-formed area. The void area is indicated in Fig. 6-9(b). The Fig. 6-9(c) represents the material at the strain state of 0.38, where the material is completely failed. From the atomistic snapshots and density plot, it is evident that the damage accumulation and void growth are the key factors for the failure of hafnia.

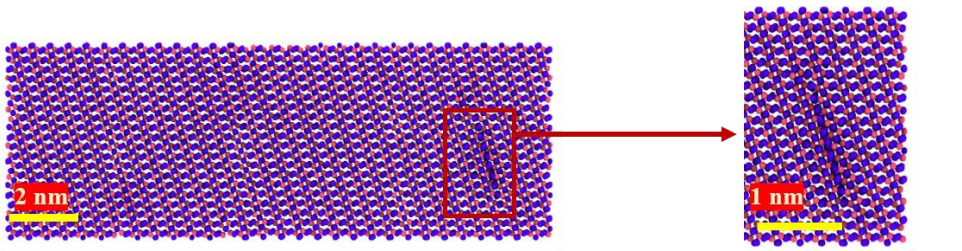

(a)

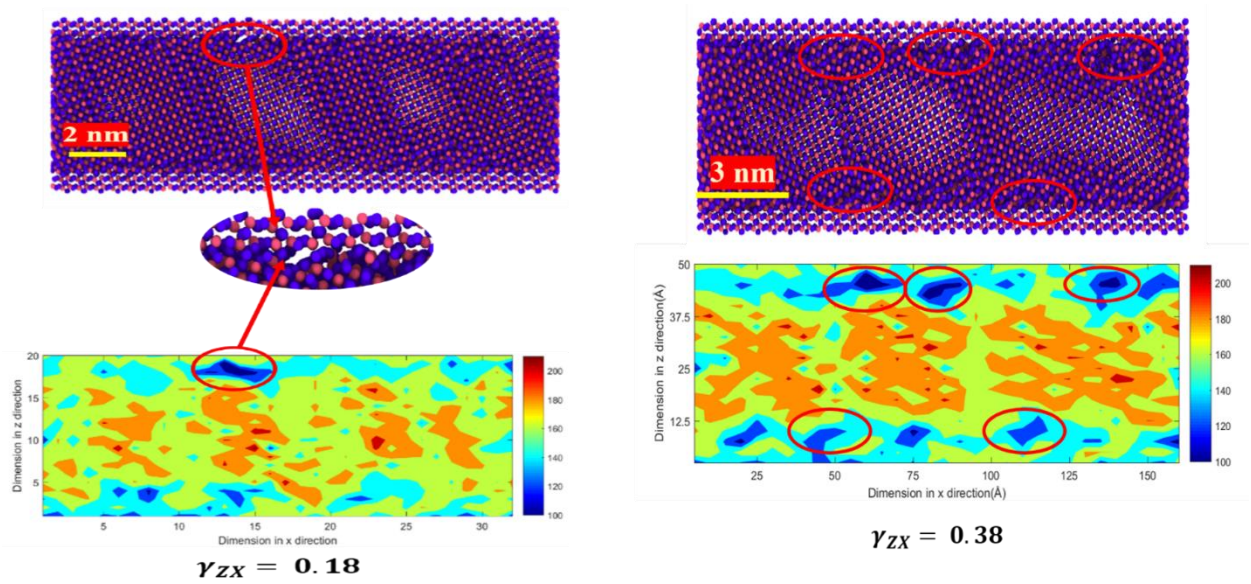

Figure 6-9 Deformed snapshots of HfO2 at different shear strain states. (a) at γ_(zx)=0.09,(b)at γ_(zx)=0.18 and (c) at γ_(zx)=0.38. These strain states correspond the red dots identified in Fig. 6-8. In (b) and (c), local distribution of atomic densities of HfO2 are shown. The color bar represents relative atomic density (ρ) of HfO_2, where ρ=1 means the atomic density at equilibrated state of the model. The blue zone represents region with lowest atomic density. Hence, these areas are potential void-formed areas.

In the next round of simulation, the direction of shear is reversed such that the angle between the vertical axis and the inclined crystal plane decreases due to loading. At the beginning of the test, the material was perfectly crystal and oxygen atoms make an angle 78.17° (measured clockwise from the horizontal axis), as indicated by point "a" in the Fig. 6-10. As the model is further deformed in shear, the angle changes from 78° to 90°. This is indicated by point "b" in the Fig. 6-10. Then the angle continues to increase with the increase in shear load, and at some point, it makes a mirror image of the initial structure. At this stage, the inclined planes make an angle of 79.65° (measured counterclockwise from the horizontal axis) at strain 0.18 (point "c" in Fig. 6-10). It can be noticed that the developed shear stress is minimum at this strain. At the shear deformation continues, the stress starts to increase again, as indicated in the stress strain curve. The tangent shear modulus beyond point "c" appears to be less than the initial modulus. This is because the reformation process did not transform the hafnia microstructure to a perfectly crystalline state but to a partially crystalline state. As such, the material became less stiff.

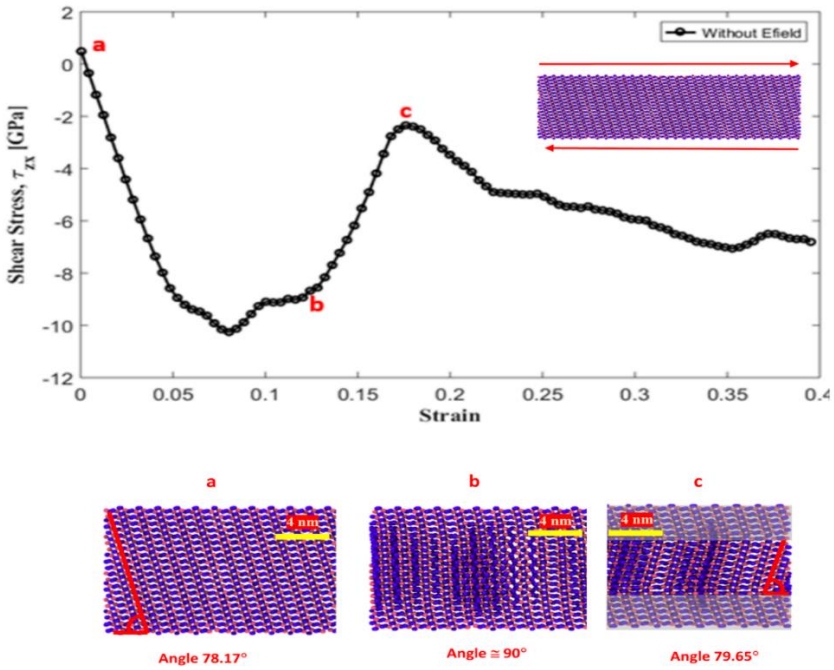

Figure 6-10 Shear stress strain curve of HfO_2. The loading direction is presented at the inset of the figure. Here, the atomistic models are corresponding to the front plane of the Fig. 6-2(b).

The combined stress strain curve that includes the shear stress-strain response due to positive (top surface displaced towards right) and negative (top surface displaced towards left) shear loading applied is shown in Fig. 6-11. The differences in shear response due to positive and negative shear on the hafnia crystal is apparent. It can be observed that the shear modulus due to negative shear loading is 179.67 GPa whereas the shear modulus due to positive shear is 248.16 GPa. The yield strength and the ultimate shear strength are higher when negative shear is applied. This is because the positive shear involves rotation of the inclined planes against compressive stress imposed by the confining top and bottom surfaces.

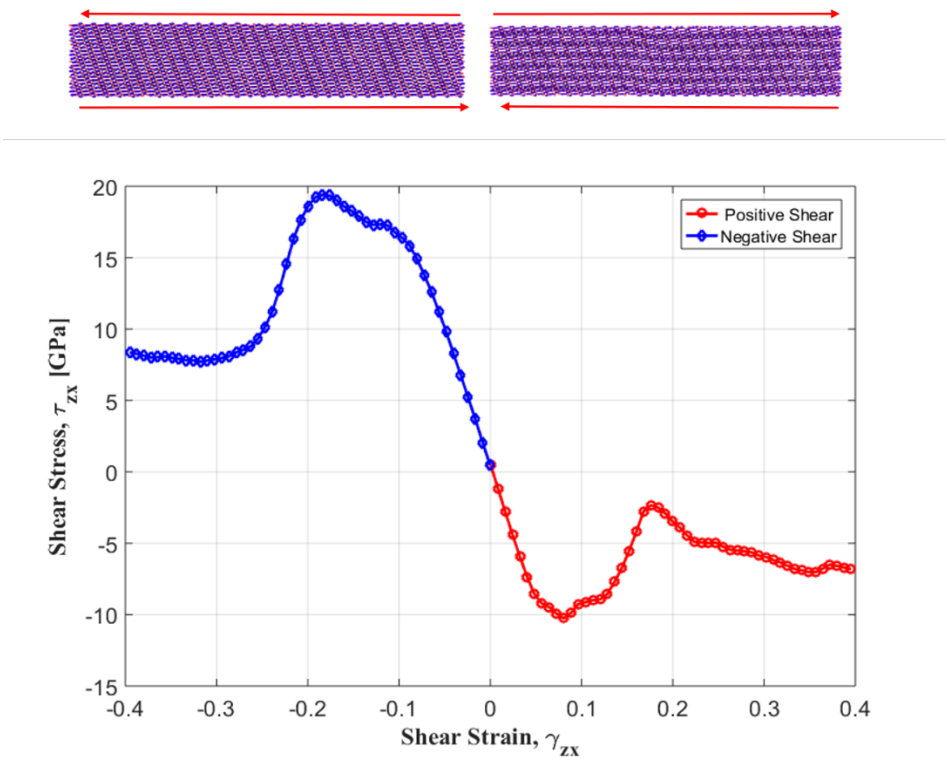

Figure 6-11 Shear stress strain curve of HfO_2 with two opposite loading directions.

For this, significant microstructural changes take place that reduces the yield strength and ultimate strength. The imposed compressive stress resists shear deformation during positive shear load. As such, the shear stiffness due to positive shear is higher. During negative shear, the inclination angle with respect to the horizontal axis reduces. The top and bottom surfaces favor does not act against the deformation. For this, the stiffness in negative shear is less than the stiffness in the positive shear. Moreover, the microstructural changes during negative shear are not as significant as the changes observed in positive shear. It means, less damage is accumulated during negative shear loading. For this, the strengths are higher.

6.4.4.2 Shear test with electric field

Shear tests were carried out under electric fields ranging from 0 to 0.3 v/Å. Before applying the shear deformation, simulation models were equilibrated with different electric fields, and their effects on the structure were observed. Figure 6-12 shows the change of total energy after applying 0.2 v/Å electric field. From the figure it is observed that after 40,000 timestep the change in the total energy is too small which

confirms the equilibration of the atomistic model. Figure 6-13 shows the MD snapshots after applying electric field. It can be observed that insignificant structural changes occurred on the material after equilibration with 0.2 v/Å. On the other hand, significant material damage is clearly noticed when 0.3 v/Å electric field is applied.

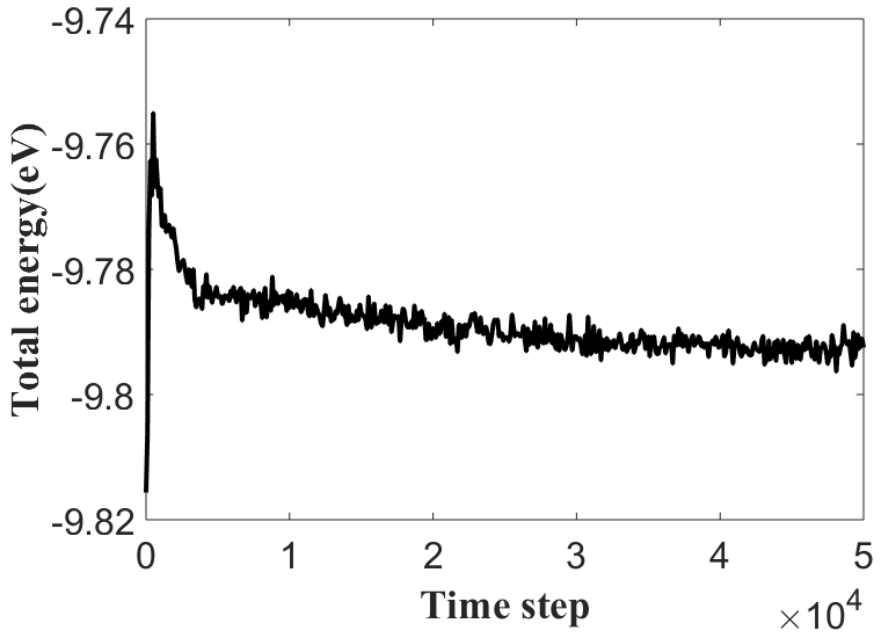

Figure 6-12 The total energy plot of HfO2 atomistic model after applying 0.2 v/Å electric field.

We believe the accumulated material damage due to applied electric field is reversible and only depends on the applied electric field. To support this hypothesis, we ran shear simulations without electric field on two different models. The first model was the one that was equilibrated with 0.3 v/Å electric field and accumulated visible damage after equilibration. The second model was equilibrated without any electric field. The stress stress-strain curves are shown in Fig. 6-14. It is evident that although electric field induces damage in a material, when shear load is applied without active electric field, the material immediately "self-heals" and there is no significant difference in the stress-strain response when this material is compared with the one that was never subjected to any electric field.

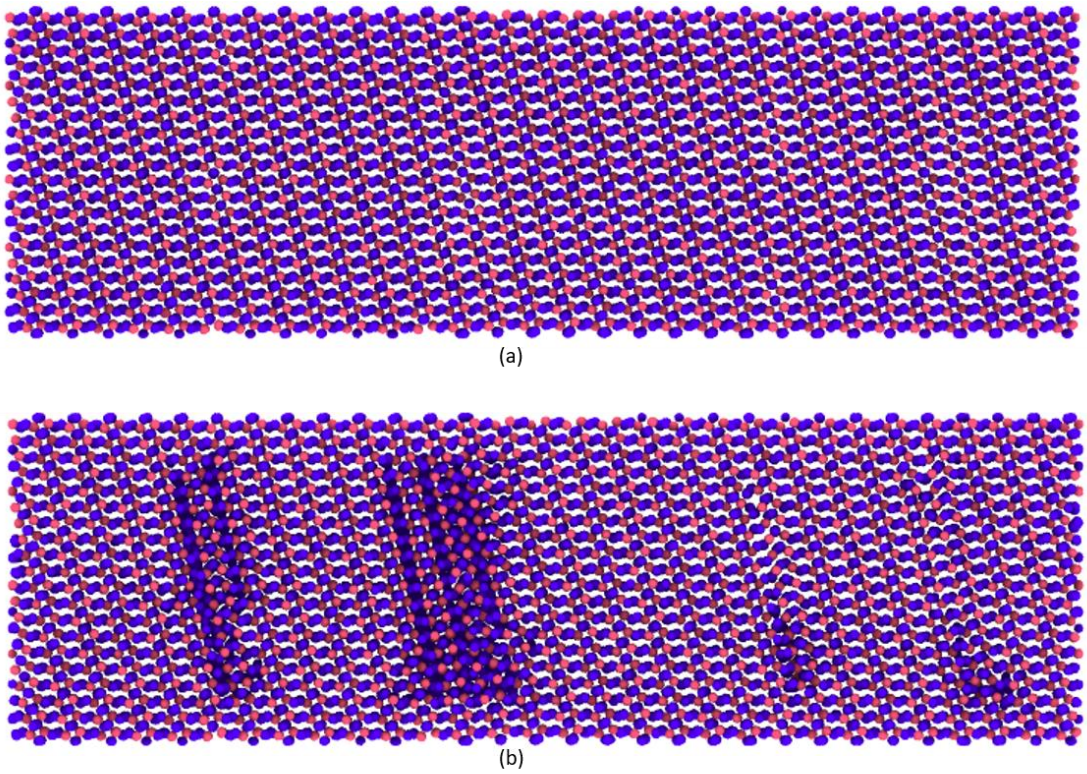

Figure 6-13 Structural changes of HfO_2 model after equilibration (a) with 0.2 v/Å Efield (b) with 0.3 v/Å Efield

The case is different when material is tested with the electric field is active. The shear responses of the material with 0.2 v/Å and 0.3 v/Å electric fields are included with the two curves just discussed. It is evident that with the shear properties of hafnia degrade with the presence of electric field. Moreover, the degradation is higher with the application of higher electric field. For instance, the shear strengths of hafnia (due to negative shear) tested with 0.2 v/Å and 0.3 v/Å active electric field are 16.87 GPa and 13.65 GPa, respectively. The shear strength of the model tested without electric field is 19.38 GPa. The trend is consistent when positive shear is applied. In particular, the shear strengths under 0.2 v/Å and 0.3 v/Å are 7.39 GPa and 7.1 GPa, respectively. The corresponding shear strength of the model tested without electric field is 10.19 GPa. It can be inferred that although the material goes through some deformation under

electric field, it has insignificant effect on the shear stress strain curve when the electric field is removed, and shear test is then carried out.

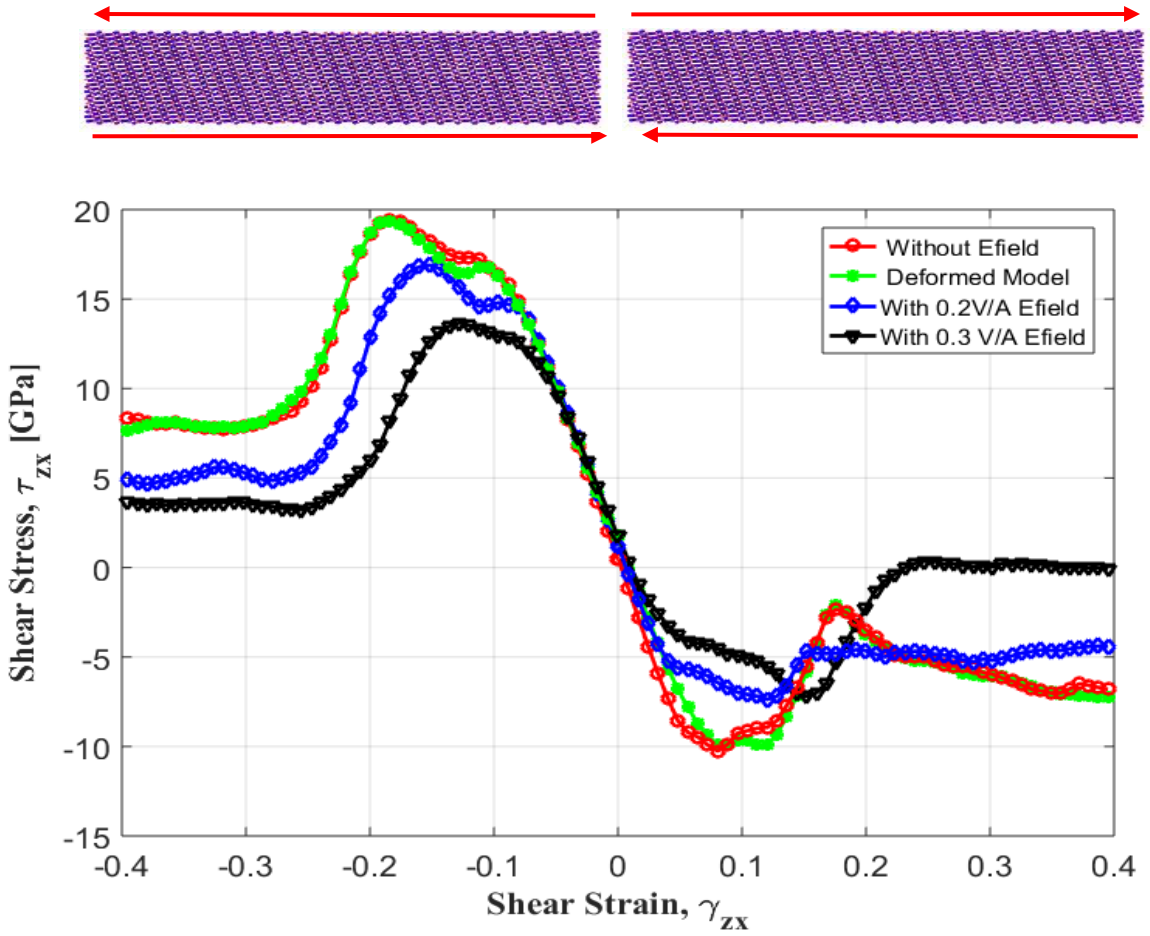

Figure 6-14 Stress-strain curves representing the effects of electric field on the shear properties of HfO_2. The electric field varies from 0 to 0.3 v/Å.

6.5 Conclusion

Here, we have studied the effect of electric field and thermal load on the mechanical properties of HfO_2. The following conclusions can be drawn from this study. First, we have found that applied electric fields can significantly alter the elastic constant and the tensile strength of HfO_2. With the electric field of 0.2 and 0.3 v/Å, the elastic constant and tensile strength of hafnia are 437.13 GPa and 29.40 GPa respectively,

whereas without electric field the values are 492.04 GPa and 42.27 GPa. The effect of temperature on the mechanical properties of HfO_2 is not significant. Nearly identical stress strain curves re found as the tensile tests were carried out at 300K and 400 K. Since the material possesses a non-symmetric structure, we have found different shear stress strain responses when shear loads are applied in the positive and negative x directions. For the positive and negative x directions, the shear strengths are 10.19 GPa and 19.38 GPa respectively. Presence of residual stress is noticed on the material when electric field is applied. This compressive residual stress can negatively affect the diffusion property of memristor material. In the near future, the effect of residual stress on the diffusion property of HfO_2 will be studied.

Chapter 7

Conclusion and Future Work

7.1 Summary

From hypersonic vehicles to electronics, ceramic materials are considered as the next generation material for their many desirable properties. By using the nanotechnology and nano particle reinforcement, tailored mechanical properties can be achieved for a certain mechanical system.

Chapter 1 we reviewed the advancement of nanotechnology as the motivation for why this dissertation focuses on the nanoscale ceramics composites and the reinforcement effect on overall mechanical properties of nanostructures. In Chapter 2, we reviewed the fabrication process of bulk ceramics and the synthesis process of nanofilms. Since molecular dynamics was used to study the failure behavior of polycrystalline ceramics and ceramic nanofilms, the theoretic foundation of MD simulation, was briefly introduced in Chapter 3.

In Chapter 4, we report the mechanical behavior of 2 polycrystalline ultra-high-temperature ceramics (UHTC s), zirconium diboride (ZrB_2) and zirconium carbide (ZrC) with zirconium diboride (ZrC-ZrB_2). These nanocomposites were investigated using large-scale molecular dynamics simulations. First, the atomistic models of the polycrystalline ZrB_2 and ZrC-ZrB_2 nanocomposites were subjected to tensile loading to determine their elastic constants and tensile strengths. What we observed is that the strength of grain-boundary materials at the nanoscale are weaker than any other part of the material. As such, the presence of nanoparticles doesn't improve their strength. It has also been observed that the failure mechanisms of both the ZrB_2 and ZrC-ZrB_2 nanocomposite are driven by grain boundary deformation. At any instant during the applied load transfer, local tensile stress distribution data indicate that atomic stress becomes much higher near the grain boundaries compared to other locations. We performed additional sets of simulations to obtain tensile and shear properties of grain boundary material.

In Chapter 5, we focused on the failure deformation of grain boundary material. By using the molecular dynamics simulation, we evaluated the mechanical properties of grain boundary by creating a sub model consisting of one grain boundary and a twin crystal from whole ZrB_2 simulation model. The new sub model was then subjected to tensile and shear loading. The atomics stress of grain boundary material are also evaluated. Comparing the strength values of grain boundary with the overall mechanical properties of ZrB_2, it can be argued that the overall material strength is influenced by the shear failure of the grain boundary materials. In addition, an analytical model was developed to estimate the grain boundary properties by using the mechanical properties of adjacent crystals and whole model properties.

In Chapter 6, the mechanical behavior of HfO_2 based nanofilms have been studied with the presence of electric field and thermal load. HfO_2 is a potential candidate for using as memristor materials for neuromorphic applications. Because of the nonsymmetric crystal structure of HfO_2, the tensile behavior of HfO_2 is different in different directions. Then, we have found that applied electric fields can significantly alter the elastic constant and the tensile strength of HfO_2. With the electric field, damage accumulation was observed in the crystal structure of HfO_2, therefore we found reduced the elastic modulus and failure strength of the materials compared to without electric field condition. In addition, we evaluated the effect of temperature on the mechanical properties of HfO_2. Nearly identical stress strain curves were found as the tensile tests were carried out at 300K and 400 K. Since the material possesses a non-symmetric structure, we have found different shear stress strain responses when shear loads are applied in the positive and negative x directions. Presence of residual stress is noticed on the material when electric field is applied which can negatively affect the diffusion properties of HfO_2.

7.2 Recommendation for Future Study

1. For the ZrB_2 based nanocomposites, the failure is driven by the grain boundary deformation which is weaker in shear loads. Therefore, core shell model of multiphase ceramics can be explored to replace the grain boundary with a stronger second phase material.

2. Simulations at the continuum scale are performed using plasticity laws within finite element framework. On the other hand, simulations at the atomic scale would require proper input from the crystallographic level. At the smallest length scale, the material building blocks are essentially discrete in nature where the governing laws of atoms are drastically different than that employed for the bulk. By using multiscale modeling one can optimize the mesoscopic properties (atomic structure, composition, microstructure, defects and interfaces etc) for which the best macroscopic material can be obtained for a given application. Therfore, Simulations can be done in different scales to find and optimize design parameters for desired macroscopic properties of ceramics.

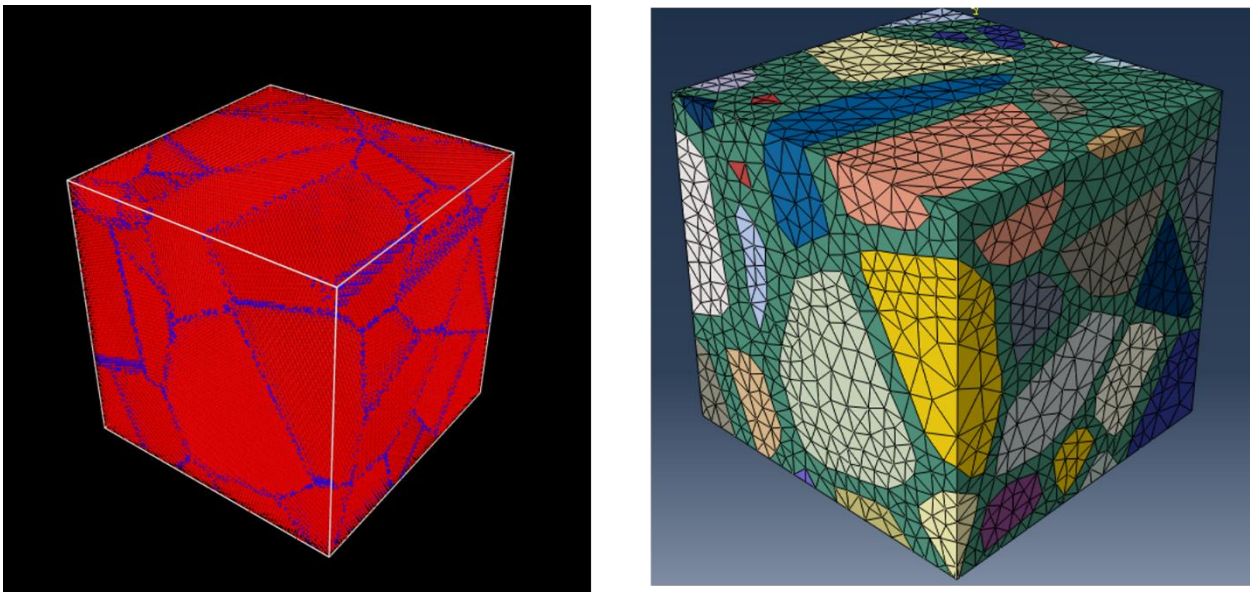

Figure 7-1 Multi scale modeling of polycrystalline ZrB_2

3. For HfO_2 nano film, presence of residual stress is noticed on the material when electric field is applied. This compressive residual stress can negatively affect the diffusion property of memristor material. In the future, the effect of residual stress on the diffusion property of HfO_2 can be studied.

References

[1] E. D. Ekpa, U. R. Asuquo, A. A. Elijah, S. N.-A. Ime, and U. A. Ini, "The oral film delivery-Application of nanotechnology and potential in medication adherence," *GSC Biol. Pharm. Sci.*, vol. 11, no. 3, pp. 34–51, 2020.

[2] P. Salunkhe, P. Bhoyar, A. Gode, and S. P. Shewale, "Application of Nanotechnology to the Extraction of Herbal Components for Medicinal Uses," *Curr. Nanomater.*, vol. 5, no. 1, pp. 4–11, 2020.

[3] K. P. Chong, "Nanotechnology and information technology in civil engineering," in *towards a vision for information technology in civil engineering*, 2004, pp. 1–9.

[4] M. C. Roco and W. S. Bainbridge, *Converging technologies for improving human performance: Nanotechnology, biotechnology, information technology and cognitive science*. Springer Science & Business Media, 2013.

[5] W. J. V. der M. Steyn, "Research and application of nanotechnology in transportation," *SATC 2008*, 2008.

[6] Z. Nurfatihah and S. Siddiquee, "Nanotechnology: recent trends in food safety, quality and market analysis," in *Nanotechnology: Applications in Energy, Drug and Food*, Springer, 2019, pp. 283–293.

[7] S. A. O. Adeyeye and O. E. Fayemi, "Nanotechnology and food processing: between innovations and consumer safety," *J. Culin. Sci. Technol.*, vol. 17, no. 5, pp. 435–452, 2019.

[8] D. Kalita and S. Baruah, "The impact of nanotechnology on food," in *Nanomaterials Applications for Environmental Matrices*, Elsevier, 2019, pp. 369–379.

[9] V. Sanna, N. Pala, and M. Sechi, "Targeted therapy using nanotechnology: focus on cancer," *Int. J. Nanomedicine*, vol. 9, p. 467, 2014.

[10] P. V Baptista, "Cancer nanotechnology-prospects for cancer diagnostics and therapy," *Curr.*

Cancer Ther. Rev., vol. 5, no. 2, pp. 80–88, 2009.

[11] M. Rai, A. P. Ingle, S. Birla, A. Yadav, and C. A. Dos Santos, "Strategic role of selected noble metal nanoparticles in medicine," *Crit. Rev. Microbiol.*, vol. 42, no. 5, pp. 696–719, 2016.

[12] B. Y. S. Kim, J. T. Rutka, and W. C. W. Chan, "Nanomedicine," *N. Engl. J. Med.*, vol. 363, no. 25, pp. 2434–2443, 2010.

[13] T. Yamashita *et al.*, "Carbon nanomaterials: efficacy and safety for nanomedicine," *Materials (Basel).*, vol. 5, no. 2, pp. 350–363, 2012.

[14] Y. Matveyev, R. Kirtaev, A. Fetisova, S. Zakharchenko, D. Negrov, and A. Zenkevich, "Crossbar Nanoscale HfO 2-Based Electronic Synapses," *Nanoscale Res. Lett.*, vol. 11, no. 1, p. 147, 2016.

[15] D. Sciti, L. Silvestroni, G. Celotti, C. Melandri, and S. Guicciardi, "Sintering and mechanical properties of ZrB2–TaSi2 and HfB2–TaSi2 ceramic composites," *J. Am. Ceram. Soc.*, vol. 91, no. 10, pp. 3285–3291, 2008.

[16] R. Nayak *et al.*, "Body armor for stab and spike protection, Part 1: Scientific literature review," *Text. Res. J.*, vol. 88, no. 7, pp. 812–832, 2018.

[17] Z. Benzait and L. Trabzon, "A review of recent research on materials used in polymer–matrix composites for body armor application," *J. Compos. Mater.*, vol. 52, no. 23, pp. 3241–3263, 2018.

[18] P. S. Gallardo, "Nanotechnology-Aided Armor," *Nanotechnol. Def. Ind. Adv. Innov. Pract. Appl.*, pp. 109–132, 2019.

[19] M. Jian *et al.*, "Advanced carbon materials for flexible and wearable sensors," *Sci. China Mater.*, vol. 60, no. 11, pp. 1026–1062, 2017.

[20] L. Hu and Y. Cui, "Energy and environmental nanotechnology in conductive paper and textiles," *Energy Environ. Sci.*, vol. 5, no. 4, pp. 6423–6435, 2012.

[21] H. B. Yildiz, E. Cevik, and B. B. Carbas, "Nanotechnology for biological photovoltaics; industrial applications of nanomaterials," in *Industrial Applications of Nanomaterials*, Elsevier, 2019, pp. 65–89.

[22] W. G. Fahrenholtz and G. E. Hilmas, "Ultra-high temperature ceramics: materials for extreme

environments," *Scr. Mater.*, vol. 129, pp. 94–99, 2017.

[23] J. Xu *et al.*, "Quinic Acid-Conjugated Nanoparticles Enhance Drug Delivery to Solid Tumors via Interactions with Endothelial Selectins," *Small*, vol. 14, no. 50, p. 1803601, 2018.

[24] H. Liu *et al.*, "Phosphorene: an unexplored 2D semiconductor with a high hole mobility," *ACS Nano*, vol. 8, no. 4, pp. 4033–4041, 2014.

[25] "ICAMS » Research." http://www.icams.de/content/research/ (accessed Jul. 17, 2020).

[26] W. Brostow and H. E. H. Lobland, *Materials: introduction and applications*. John Wiley & Sons, 2016.

[27] S. F. Ferdous, "Improving Fracture Toughness Of Silicon Carbide Based Ceramics By Microstructure Tailoring," 2015.

[28] R. O. Ritchie, "The conflicts between strength and toughness," *Nat. Mater.*, vol. 10, no. 11, pp. 817–822, 2011.

[29] B. Basu and K. Balani, *Advanced structural ceramics*. John Wiley & Sons, 2011.

[30] E. W. Neuman, "Elevated temperature mechanical properties of zirconium diboride based ceramics," 2014.

[31] Q. Fang *et al.*, "Investigation of TiO2-doped HfO2 thin films deposited by photo-CVD," *Thin Solid Films*, vol. 428, no. 1–2, pp. 263–268, 2003.

[32] S. Nonobe, N. Takahashi, and T. Nakamura, "Preparation of HfO2 nano-films by atomic layer deposition using HfCl4 and O2 under atmospheric pressure," *Solid state Sci.*, vol. 6, no. 11, pp. 1217–1219, 2004.

[33] W.-E. Fu, B.-C. He, and Y.-Q. Chang, "Surface mechanical property assessment of ultra-thin HfO2 films," *Thin Solid Films*, vol. 544, pp. 212–217, 2013.

[34] T. S. Yang *et al.*, "Chemical vapor deposition of HfO2 thin films using the novel single precursor hafnium 3-Methyl-3-pentoxide, Hf (mp) 4," *Chem. Mater.*, vol. 17, no. 26, pp. 6713–6718, 2005.

[35] F.-Z. Dai, Y. Zhou, and W. Sun, "Segregation of solute atoms (Y, Nb, Ta, Mo and W) in ZrB2 grain boundaries and their effects on grain boundary strengths: A first-principles investigation,"

Acta Mater., vol. 127, pp. 312–318, 2017.

[36] J. G. Lee, *Computational materials science: an introduction*. CRC press, 2016.

[37] J. Tersoff, "New empirical approach for the structure and energy of covalent systems," *Phys. Rev. B*, vol. 37, no. 12, p. 6991, 1988.

[38] T.-R. Shan, B. D. Devine, T. W. Kemper, S. B. Sinnott, and S. R. Phillpot, "Charge-optimized many-body potential for the hafnium/hafnium oxide system," *Phys. Rev. B*, vol. 81, no. 12, p. 125328, 2010.

[39] S. R. Phillpot *et al.*, "Charge Optimized Many Body (COMB) potentials for simulation of nuclear fuel and clad," *Comput. Mater. Sci.*, vol. 148, pp. 231–241, 2018, doi: https://doi.org/10.1016/j.commatsci.2018.02.041.

[40] A. Adnan, "Molecular simulations of deformation, failure and fracture of nanostructured materials." Purdue University, 2008.

[41] A. K. Subramaniyan and C. T. Sun, "Continuum interpretation of virial stress in molecular simulations," *Int. J. Solids Struct.*, vol. 45, no. 14, pp. 4340–4346, 2008, doi: https://doi.org/10.1016/j.ijsolstr.2008.03.016.

[42] R. J. Hardy, "Formulas for determining local properties in molecular-dynamics simulations: Shock waves," *J. Chem. Phys.*, vol. 76, no. 1, pp. 622–628, 1982.

[43] J. H. Irving and J. G. Kirkwood, "The statistical mechanical theory of transport processes. IV. The equations of hydrodynamics," *J. Chem. Phys.*, vol. 18, no. 6, pp. 817–829, 1950.

[44] F. Monteverde, A. Bellosi, and L. Scatteia, "Processing and properties of ultra-high temperature ceramics for space applications," *Mater. Sci. Eng. A*, vol. 485, no. 1–2, pp. 415–421, 2008.

[45] R. Savino, M. D. S. Fumo, D. Paterna, and M. Serpico, "Aerothermodynamic study of UHTC-based thermal protection systems," *Aerosp. Sci. Technol.*, vol. 9, no. 2, pp. 151–160, 2005.

[46] T. H. Squire and J. Marschall, "Material property requirements for analysis and design of UHTC components in hypersonic applications," *J. Eur. Ceram. Soc.*, vol. 30, no. 11, pp. 2239–2251, 2010.

[47] M. Belmonte, “Advanced ceramic materials for high temperature applications,” *Adv. Eng. Mater.*, vol. 8, no. 8, pp. 693–703, 2006.

[48] F. Monteverde and A. Bellosi, “Microstructure and properties of an HfB2-SiC composite for ultra high temperature applications,” *Adv. Eng. Mater.*, vol. 6, no. 5, pp. 331–336, 2004.

[49] W. G. Fahrenholtz, G. E. Hilmas, I. G. Talmy, and J. A. Zaykoski, “Refractory diborides of zirconium and hafnium,” *J. Am. Ceram. Soc.*, vol. 90, no. 5, pp. 1347–1364, 2007.

[50] Q. Hu, P. Luo, M. Zhang, M. Song, and J. Li, “Combustion and formation behavior of hybrid ZrB2 and ZrC particles in Al–Zr–B4C system during self-propagation high temperature synthesis,” *Int. J. Refract. Met. Hard Mater.*, vol. 31, pp. 89–95, 2012.

[51] W. Guo and G. Zhang, “Microstructures and mechanical properties of hot-pressed ZrB2-based ceramics from synthesized ZrB2 and ZrB2-ZrC Powders,” *Adv. Eng. Mater.*, vol. 11, no. 3, pp. 206–210, 2009.

[52] H.-L. Liu, G.-J. Zhang, J.-X. Liu, and H. Wu, “Synergetic roles of ZrC and SiC in ternary ZrB2–SiC–ZrC ceramics,” *J. Eur. Ceram. Soc.*, vol. 35, no. 16, pp. 4389–4397, 2015.

[53] D. Ağaoğulları, H. Gökçe, İ. Duman, and M. L. Öveçoğlu, “Characterization investigations of ZrB2/ZrC ceramic powders synthesized by mechanical alloying of elemental Zr, B and C blends,” *J. Eur. Ceram. Soc.*, vol. 32, no. 7, pp. 1447–1455, 2012.

[54] R. E. Tressler, “Recent developments in fibers and interphases for high temperature ceramic matrix composites,” *Compos. Part A Appl. Sci. Manuf.*, vol. 30, no. 4, pp. 429–437, 1999.

[55] I. Farahbakhsh, Z. Ahmadi, and M. S. Asl, “Densification, microstructure and mechanical properties of hot pressed ZrB2–SiC ceramic doped with nano-sized carbon black,” *Ceram. Int.*, vol. 43, no. 11, pp. 8411–8417, 2017.

[56] S. C. Zhang, G. E. Hilmas, and W. G. Fahrenholtz, “Pressureless sintering of ZrB2–SiC ceramics,” *J. Am. Ceram. Soc.*, vol. 91, no. 1, pp. 26–32, 2008.

[57] A. L. Chamberlain, W. G. Fahrenholtz, and G. E. Hilmas, “Low-temperature densification of zirconium diboride ceramics by reactive hot pressing,” *J. Am. Ceram. Soc.*, vol. 89, no. 12, pp.

3638–3645, 2006.

[58] M. Thompson, W. G. Fahrenholtz, and G. Hilmas, “Effect of starting particle size and oxygen content on densification of ZrB2,” *J. Am. Ceram. Soc.*, vol. 94, no. 2, pp. 429–435, 2011.

[59] S. C. Zhang, G. E. Hilmas, and W. G. Fahrenholtz, “Pressureless densification of zirconium diboride with boron carbide additions,” *J. Am. Ceram. Soc.*, vol. 89, no. 5, pp. 1544–1550, 2006.

[60] H.-L. Liu, J.-X. Liu, H.-T. Liu, and G.-J. Zhang, “Contour maps of mechanical properties in ternary ZrB2SiCZrC ceramic system,” *Scr. Mater.*, vol. 107, pp. 140–144, 2015.

[61] Q. Qiang, Z. Xinghong, M. Songhe, H. Wenbo, H. Changqing, and H. Jiecai, “Reactive hot pressing and sintering characterization of ZrB2–SiC–ZrC composites,” *Mater. Sci. Eng. A*, vol. 491, no. 1–2, pp. 117–123, 2008.

[62] T. Cheng and W. Li, “The temperature-dependent ideal tensile strength of ZrB2, HfB2, and TiB2,” *J. Am. Ceram. Soc.*, vol. 98, no. 1, pp. 190–196, 2015.

[63] X. Zhang, X. Luo, J. Li, P. Hu, and J. Han, “The ideal strength of transition metal diborides TMB2 (TM= Ti, Zr, Hf): Plastic anisotropy and the role of prismatic slip,” *Scr. Mater.*, vol. 62, no. 8, pp. 625–628, 2010.

[64] A. Stukowski, “Visualization and analysis of atomistic simulation data with OVITO–the Open Visualization Tool,” *Model. Simul. Mater. Sci. Eng.*, vol. 18, no. 1, p. 15012, 2009.

[65] N. L. Okamoto, M. Kusakari, K. Tanaka, H. Inui, and S. Otani, “Anisotropic elastic constants and thermal expansivities in monocrystal CrB2, TiB2, and ZrB2,” *Acta Mater.*, vol. 58, no. 1, pp. 76–84, 2010.

[66] X. Zhang, X. Luo, J. Han, J. Li, and W. Han, “Electronic structure, elasticity and hardness of diborides of zirconium and hafnium: First principles calculations,” *Comput. Mater. Sci.*, vol. 44, no. 2, pp. 411–421, 2008.

[67] S. Zhu, “Densification, microstructure, and mechanical properties of zirconium diboride based ultra-high temperature ceramics,” 2008.

[68] S. Zhu, W. G. Fahrenholtz, G. E. Hilmas, and S. C. Zhang, “Pressureless sintering of zirconium

diboride using boron carbide and carbon additions," *J. Am. Ceram. Soc.*, vol. 90, no. 11, pp. 3660–3663, 2007.

[69] F. Monteverde, S. Guicciardi, and A. Bellosi, "Advances in microstructure and mechanical properties of zirconium diboride based ceramics," *Mater. Sci. Eng. A*, vol. 346, no. 1–2, pp. 310–319, 2003.

[70] F. Monteverde and A. Bellosi, "Beneficial effects of AlN as sintering aid on microstructure and mechanical properties of hot-pressed ZrB2," *Adv. Eng. Mater.*, vol. 5, no. 7, pp. 508–512, 2003.

[71] A. L. Chamberlain, W. G. Fahrenholtz, G. E. Hilmas, and D. T. Ellerby, "High-strength zirconium diboride-based ceramics," *J. Am. Ceram. Soc.*, vol. 87, no. 6, pp. 1170–1172, 2004.

[72] A. L. Chamberlain, W. G. Fahrenholtz, and G. E. Hilmas, "Pressureless sintering of zirconium diboride," *J. Am. Ceram. Soc.*, vol. 89, no. 2, pp. 450–456, 2006.

[73] E. V Clougherty, K. E. Wilkes, and R. P. Tye, "Research and Development of Refractory Oxidation-Resistant Diborides. Part 2, Volume 5: Thermal, Physical, Electrical and Optical Properties," MANLABS INC CAMBRIDGE MA, 1969.

[74] J. J. Meléndez-Martınez, A. Domınguez-Rodrıguez, F. Monteverde, C. Melandri, and G. De Portu, "Characterisation and high temperature mechanical properties of zirconium boride-based materials," *J. Eur. Ceram. Soc.*, vol. 22, no. 14–15, pp. 2543–2549, 2002.

[75] F. Monteverde, "Beneficial effects of an ultra-fine α-SiC incorporation on the sinterability and mechanical properties of ZrB 2," *Appl. Phys. A*, vol. 82, no. 2, pp. 329–337, 2006.

[76] F. Monteverde, "The addition of SiC particles into a MoSi2-doped ZrB2 matrix: effects on densification, microstructure and thermo-physical properties," *Mater. Chem. Phys.*, vol. 113, no. 2–3, pp. 626–633, 2009.

[77] Q. Liu, W. Han, and J. Han, "Influence of SiCnp content on the microstructure and mechanical properties of ZrB2–SiC nanocomposite," *Scr. Mater.*, vol. 63, no. 6, pp. 581–584, 2010.

[78] R. M. Jones, *Mechanics of composite materials*. CRC press, 1998.

[79] W. D. Callister and D. G. Rethwisch, *Materials science and engineering*, vol. 5. John wiley &

sons NY, 2011.

[80] V. Samvedi and V. Tomar, “An ab initio study of ZrB2–SiC interface strength as a function of temperature: Correlating phononic and electronic thermal contributions,” *J. Eur. Ceram. Soc.*, vol. 33, no. 3, pp. 615–625, 2013.

[81] E. W. Neuman, G. E. Hilmas, and W. G. Fahrenholtz, “Ultra-high temperature mechanical properties of a zirconium diboride–zirconium carbide ceramic,” *J. Am. Ceram. Soc.*, vol. 99, no. 2, pp. 597–603, 2016.

[82] W. G. Fahrenholtz, E. J. Wuchina, W. E. Lee, and Y. Zhou, *Ultra-high temperature ceramics: materials for extreme environment applications*. John Wiley & Sons, 2014.

[83] D. KALISH, E. V CLOUGHERTY, and K. KREDER, “Strength, fracture mode, and thermal stress resistance of HfB2 and ZrB2,” *J. Am. Ceram. Soc.*, vol. 52, no. 1, pp. 30–36, 1969.

[84] W.-W. Wu, Y. Sakka, M. Estili, T. S. Suzuki, T. Nishimura, and G.-J. Zhang, “Microstructure and high-temperature strength of textured and non-textured ZrB2 ceramics,” *Sci. Technol. Adv. Mater.*, vol. 15, no. 1, p. 14202, 2013.

[85] L. Silvestroni, H.-J. Kleebe, S. Lauterbach, M. Müller, and D. Sciti, “Transmission electron microscopy on Zr-and Hf-borides with MoSi 2 addition: densification mechanisms,” *J. Mater. Res.*, vol. 25, no. 5, pp. 828–834, 2010.

[86] L. Silvestroni and D. Sciti, “Densification of ZrB2–TaSi2 and HfB2–TaSi2 ultra-high-temperature ceramic composites,” *J. Am. Ceram. Soc.*, vol. 94, no. 6, pp. 1920–1930, 2011.

[87] S. Kumar and S. K. Kurtz, “Simulation of material microstructure using a 3D Voronoi tesselation: Calculation of effective thermal expansion coefficient of polycrystalline materials,” *Acta Metall. Mater.*, vol. 42, no. 12, pp. 3917–3927, 1994.

[88] A. Kınacı *et al.*, “Interatomic potentials for zirconium diboride and hafnium diboride,” *Phys. Rev. B*, vol. 50, no. 11, pp. 2828–2835, 2011.

[89] A. Kınacı, J. B. Haskins, C. Sevik, and T. Çağın, “Thermal conductivity of BN-C nanostructures,” *Phys. Rev. B*, vol. 86, no. 11, p. 115410, 2012.

[90] S.-Q. Guo, “Densification of ZrB2-based composites and their mechanical and physical properties: a review,” *J. Eur. Ceram. Soc.*, vol. 29, no. 6, pp. 995–1011, 2009.

[91] S. Plimpton, “Fast parallel algorithms for short-range molecular dynamics,” *J. Comput. Phys.*, vol. 117, no. 1, pp. 1–19, 1995.

[92] W. G. Fahrenholtz, G. E. Hilmas, S. C. Zhang, and S. Zhu, “Pressureless sintering of zirconium diboride: particle size and additive effects,” *J. Am. Ceram. Soc.*, vol. 91, no. 5, pp. 1398–1404, 2008.

[93] X. Zhang, L. Xu, W. Han, L. Weng, J. Han, and S. Du, “Microstructure and properties of silicon carbide whisker reinforced zirconium diboride ultra-high temperature ceramics,” *Solid State Sci.*, vol. 11, no. 1, pp. 156–161, 2009.

[94] E. Neuman, W. Fahrenholtz, and G. Hilmas, “Factorial design to minimize residual oxygen in reaction hot-pressed zirconium diboride,” *Int. J. Appl. Ceram. Technol.*, vol. 14, no. 4, pp. 636–643, 2017.

[95] E. W. Neuman, G. E. Hilmas, and W. G. Fahrenholtz, “Processing, microstructure, and mechanical properties of zirconium diboride-boron carbide ceramics,” *Ceram. Int.*, vol. 43, no. 9, pp. 6942–6948, 2017.

[96] R. Jiang, P. Ma, Z. Han, and X. Du, “Habituation/Fatigue behavior of a synapse memristor based on IGZO–HfO 2 thin film,” *Sci. Rep.*, vol. 7, no. 1, p. 9354, 2017.

[97] E. Covi, S. Brivio, A. Serb, T. Prodromakis, M. Fanciulli, and S. Spiga, “HfO2-based memristors for neuromorphic applications,” in *Circuits and Systems (ISCAS), 2016 IEEE International Symposium on*, 2016, pp. 393–396.

[98] M. Bendova, Z. Pytlicek, J. Prasek, and A. Mozalev, “The growth and unique electronic properties of the porous-alumina-assisted hafnium-oxide nanostructured films,” *Electrochim. Acta*, vol. 327, p. 135029, Dec. 2019, doi: 10.1016/J.ELECTACTA.2019.135029.

[99] X. Zhao and D. Vanderbilt, “First-principles study of structural, vibrational, and lattice dielectric properties of hafnium oxide,” *Phys. Rev. B*, vol. 65, no. 23, p. 233106, 2002.

[100] L. Zhang, J. Fan, and M. Qu, “MD Simulations on the Transport Behaviors of Mixed Na+ and Li+ in a Transmembrane Cyclic Peptide Nanotube un[1] L. Zhang, J. Fan, and M. Qu, “MD Simulations on the Transport Behaviors of Mixed Na+ and Li+ in a Transmembrane Cyclic Peptide Nanotube under a,” *J. Chem. Inf. Model.*, vol. 59, no. 1, pp. 170–180, Jan. 2019, doi: 10.1021/acs.jcim.8b00593.

[101] I. K. Schuller and R. Stevens, “Neuromorphic computing: from materials to systems architecture,” *Round Table Rep.*, 2015.

[102] S. H. Jo, T. Chang, I. Ebong, B. B. Bhadviya, P. Mazumder, and W. Lu, “Nanoscale memristor device as synapse in neuromorphic systems,” *Nano Lett.*, vol. 10, no. 4, pp. 1297–1301, 2010.

[103] S. Ambrogio *et al.*, “Modeling resistive switching materials and devices across scales,” *J. Electroceramics*, vol. 39, no. 1–4, pp. 39–60, 2017.

[104] L. Qiu *et al.*, “Electro curing of oriented bismaleimide between aligned carbon nanotubes for high mechanical and thermal performances,” *Carbon N. Y.*, vol. 145, pp. 650–657, Apr. 2019, doi: 10.1016/J.CARBON.2019.01.074.

[105] D. B. Strukov, G. S. Snider, D. R. Stewart, and R. S. Williams, “The missing memristor found,” *Nature*, vol. 453, no. 7191, p. 80, 2008.

[106] M. C. Shaw *et al.*, “Enhanced thermal management by direct water spray of high-voltage, high power devices in a three-phase, 18-hp ac motor drive demonstration,” in *ITherm 2002. Eighth Intersociety Conference on Thermal and Thermomechanical Phenomena in Electronic Systems (Cat. No. 02CH37258)*, 2002, pp. 1007–1014.

[107] L. Meysenc, M. Jylhakallio, and P. Barbosa, “Power electronics cooling effectiveness versus thermal inertia,” *IEEE Trans. Power Electron.*, vol. 20, no. 3, pp. 687–693, 2005.

[108] G.-Q. Lu, J. N. Calata, Z. Zhang, and J. G. Bai, “A lead-free, low-temperature sintering die-attach technique for high-performance and high-temperature packaging,” in *Proceedings of the Sixth IEEE CPMT Conference on High Density Microsystem Design and Packaging and Component Failure Analysis (Hdp’04)*, 2004, pp. 42–46.

[109] J. P. Strachan *et al.*, “Direct identification of the conducting channels in a functioning memristive device,” *Adv. Mater.*, vol. 22, no. 32, pp. 3573–3577, 2010.

[110] S. E. Savel’Ev, A. S. Alexandrov, A. M. Bratkovsky, and R. S. Williams, “Molecular dynamics simulations of oxide memory resistors (memristors),” *Nanotechnology*, vol. 22, no. 25, p. 254011, 2011.

[111] L. Liang, X. Kang, Y. Sang, and H. Liu, “One-Dimensional Ferroelectric Nanostructures: Synthesis, Properties, and Applications,” *Adv. Sci.*, vol. 3, no. 7, p. 1500358, 2016.

[112] D. Garbin *et al.*, “HfO 2-based OxRAM devices as synapses for convolutional neural networks,” *IEEE Trans. Electron Devices*, vol. 62, no. 8, pp. 2494–2501, 2015.

[113] E. Covi, S. Brivio, M. Fanciulli, and S. Spiga, “Synaptic potentiation and depression in Al: HfO2-based memristor,” *Microelectron. Eng.*, vol. 147, pp. 41–44, 2015.

[114] Y. Gao and F. Müller-Plathe, “Molecular Dynamics Study on the Thermal Conductivity of the End-grafted Carbon Nanotubes Filled Polyamide-6.6 Nanocomposites,” *J. Phys. Chem. C*, vol. 122, no. 2, pp. 1412–1421, Jan. 2018, doi: 10.1021/acs.jpcc.7b11310.

[115] M. Foroutan, V. F. Naeini, and M. Ebrahimi, “Carbon nanotubes encapsulating fullerene as water nano-channels with distinctive selectivity: Molecular dynamics simulation,” *Appl. Surf. Sci.*, vol. 489, pp. 198–209, Sep. 2019, doi: 10.1016/J.APSUSC.2019.05.229.

[116] Y. Feng, H. Zou, L. Qiu, and X. Zhang, “Size effect on the thermal conductivity of octadecanoic acid: A molecular dynamics study,” *Comput. Mater. Sci.*, vol. 158, pp. 14–19, Feb. 2019, doi: 10.1016/J.COMMATSCI.2018.11.012.

[117] H. Park *et al.*, “Exploring new approaches towards the formability of mixed-ion perovskites by DFT and machine learning,” *Phys. Chem. Chem. Phys.*, vol. 21, no. 3, pp. 1078–1088, 2019, doi: 10.1039/C8CP06528D.

[118] L. Qiu *et al.*, “Enhancing the interfacial interaction of carbon nanotubes fibers by Au nanoparticles with improved performance of the electrical and thermal conductivity,” *Carbon N. Y.*, vol. 141, pp. 497–505, Jan. 2019, doi: 10.1016/J.CARBON.2018.09.073.

[119] M. L. Martin, M. Dadfarnia, A. Nagao, S. Wang, and P. Sofronis, “Enumeration of the hydrogen-enhanced localized plasticity mechanism for hydrogen embrittlement in structural materials,” *Acta Mater.*, vol. 165, pp. 734–750, Feb. 2019, doi: 10.1016/J.ACTAMAT.2018.12.014.

[120] M. A. Z. Mamun, M. Hasan, N. Mustakim, and S. Subrina, “A Molecular Dynamics Study of Thermal conductivity in Monolayer GaN Nanoribbon,” in *TENCON 2019 - 2019 IEEE Region 10 Conference (TENCON)*, 2019, pp. 52–56, doi: 10.1109/TENCON.2019.8929484.

[121] C.-K. Lee, E. Cho, H.-S. Lee, C. S. Hwang, and S. Han, “First-principles study on doping and phase stability of HfO 2,” *Phys. Rev. B*, vol. 78, no. 1, p. 12102, 2008.

[122] S. Brivio, E. Covi, A. Serb, T. Prodromakis, M. Fanciulli, and S. Spiga, “Gradual set dynamics in HfO 2-based memristor driven by sub-threshold voltage pulses,” in *2015 International Conference on Memristive Systems (MEMRISYS)*, 2015, pp. 1–2.

[123] X. Yang *et al.*, “Investigation on the RESET switching mechanism of bipolar Cu/HfO2/Pt RRAM devices with a statistical methodology,” *J. Phys. D. Appl. Phys.*, vol. 46, no. 24, p. 245107, 2013.

[124] L. Wei Zhou *et al.*, “Interface engineering for improving reliability of resistance switching in Cu/HfO2/TiO2/Pt structure,” *Appl. Phys. Lett.*, vol. 107, no. 7, p. 72901, 2015.

[125] M. Berdova *et al.*, “Hardness, elastic modulus, and wear resistance of hafnium oxide-based films grown by atomic layer deposition,” *J. Vac. Sci. Technol. A Vacuum, Surfaces, Film.*, vol. 34, no. 5, p. 51510, 2016.

[126] S. L. Dole, O. Hunter Jr, and C. J. Wooge, “Elastic properties of monoclinic hafnium oxide at room temperature,” *J. Am. Ceram. Soc.*, vol. 60, no. 11-12, pp. 488–490, 1977.

[127] M. de Jong *et al.*, “Charting the complete elastic properties of inorganic crystalline compounds,” *Sci. Data*, vol. 2, no. 1, p. 150009, 2015, doi: 10.1038/sdata.2015.9.

[128] Y. Shi, A. H. Bork, S. Schweiger, and J. L. M. Rupp, “The effect of mechanical twisting on oxygen ionic transport in solid-state energy conversion membranes,” *Nat. Mater.*, vol. 14, no. 7, p. 721, 2015.

[129] X. Cao, T. Wang, K. D. T. Ngo, and G.-Q. Lu, “Characterization of lead-free solder and sintered

nano-silver die-attach layers using thermal impedance," *IEEE Trans. Components, Packag. Manuf. Technol.*, vol. 1, no. 4, pp. 495–501, 2011.

[130] Z. Fang *et al.*, "Temperature Instability of Resistive Switching on $\hbox {HfO} _ {x} $-Based RRAM Devices," *IEEE Electron Device Lett.*, vol. 31, no. 5, pp. 476–478, 2010.

[131] J. C. Garcia *et al.*, "Band structure derived properties of HfO2 from first principles calculations," in *AIP Conference Proceedings*, 2005, vol. 772, no. 1, pp. 189–191.